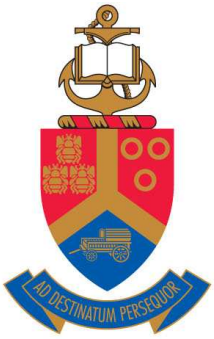

UNIVERSITEIT VAN PRETORIA
UNIVERSITY OF PRETORIA
YUNIBESITHI YA PRETORIA

ON THE PERFORMANCE GAIN OF STFC-LDPC CONCATENATED CODING SCHEME FOR MIMO-WiMAX

K.P MARÉ

2009

UNIVERSITEIT VAN PRETORIA
UNIVERSITY OF PRETORIA
YUNIBESITHI YA PRETORIA

ON THE PERFORMANCE GAIN OF STFC-LDPC CONCATENATED CODING SCHEME FOR MIMO-WiMAX

By

Karel Petrus Maré

Study leader: Dr. B.T. Maharaj

Submitted in partial fulfilment of the requirements for the degree

Master of Engineering (Electronic)

in the

Department of Electrical, Electronic & Computer Engineering

in the

School of Engineering

in the

Faculty of Engineering, Built Environment & Information Technology

UNIVERSITY OF PRETORIA

Feb 2009

SUMMARY

ON THE PERFORMANCE GAIN OF STFC-LDPC CONCATENATED CODING SCHEME FOR MIMO-WiMAX

by

Karel Petrus Maré

Studyleader: Dr. B.T. Maharaj

Department of Electrical, Electronic & Computer Engineering

Master of Engineering (Electronic)

In mobile communications, using multiple transmit and receive antennas has shown considerable improvement over single antenna systems. The performance increase can be characterized by more reliable throughput obtained through diversity and the higher achievable data rate through spatial multiplexing. The combination of multiple-input multiple-output (MIMO) wireless technology with the IEEE 802.16e-2005 (WiMAX) standard has been recognized as one of the most promising technologies with the advent of next generation broadband wireless communications. The dissertation introduces a performance evaluation of modern multi-antenna coding techniques on a MIMO-WiMAX platform developed to be capable of simulating space-selective, time-selective and frequency-selective fading conditions, which are known as triply-selective fading conditions. A new concatenated space-time-frequency low-density parity check (LDPC) code is proposed for high performance MIMO systems, where it is shown that the newly defined coding technique outperforms a more conventional approach by concatenating space-time blocks with LDPC codes. The analysis of the coding techniques in realistic mobile environments, as well as the proposed STFC-LDPC code, can form a set of newly defined codes, complementing the current coding schemes defined in the WiMAX standard.

Keywords:

MIMO, space-time codes, space-frequency codes, space-time-frequency codes, capacity, correlation and LDPC .

OPSOMMING

ON THE PERFORMANCE GAIN OF STFC-LDPC CONCATENATED CODING SCHEME FOR MIMO-WiMAX

deur

Karel Petrus Maré

Studieleier: Dr. B.T. Maharaj

Departement Elektriese, Elektroniese & Rekenaar Ingenieurswese

Meester in Ingenieurswese (Elektronies)

In mobiele kommunikasie het die gebruik van veelvoudige versend- en ontvangsantennas 'n aansienlike verbetering teenoor enkel-antennastelsels getoon. Die verbetering in werkverrigting kan toegeskryf word aan 'n meer betroubare deurset verkry deur diversiteit en die hoër data oordragtempo wat verkry kan word deur ruimtelike multipleksering. Die kombinasie van veelvoudige-inset veelvoudige-uitset (VIVO) koordlose tegnologie met die IEEE 802.16e-2005 WiMAX standaard word erken as een van die mees belowende tegnologieë in die volgende generasie breëband koordlose kommunikasies. Hierdie verhandeling stel bekend 'n werkverrigtingsevaluasie van moderne multi-antenna-koderingstegnieke op 'n VIVO-WiMAX platform wat ontwikkel is met die vermoë om ruimte-selektiewe, tyd-selektiewe en frekwensie-selektiewe deiningkondisies te simuleer, wat bekend staan as drievoudig-selektiewe deiningkondisies. 'n Nuwe samekoppeling van ruimte-tyd-frekwensie lae digtheid pariteitstoetskode word voorgestel vir hoë-verrigting VIVO stelsels waar aangetoon word dat die nuwe gedefinieerde koderingstegniek beter presteer as die meer konvensionele benadering om die ruimte-tydblokke met lae digtheid pariteitstoetskodes te koppel. Die analise van die koderingstegnieke in realistiese mobiele omgewings, sowel as die voorgestelde ruimte-tyd-frekwensie lae digtheidpariteitstoets kode, kan 'n stel nuwe gedefinieerde kodes daarstel, wat die bestaande koderingskemas soos gedefinieer in die WiMAX standaard komplementeer.

Sleutelwoorde:

VIVU, ruimte-tydkodes, ruimte-frekwensiekodes, ruimte-tyd-frekwensie, kapasiteit, korrelasie.

This dissertation is dedicated to:

God Almighty, for all the countless opportunities He has given me;

My loving family and friends, for their support, encouragement and good advice

ACKNOWLEDGEMENTS

The author would like to thank the following people and institutions without whose help this dissertation would not have been possible:

- My study leader, Dr. B.T Maharaj, for all the advice and guidance he has given me.

- The Sentech Chair in Broadband Wireless Multimedia Communications (BWMC) at the University of Pretoria and the National Research Foundation (NRF) for their financial support.

- My fellow students at BWMC for their useful suggestions and advice.

- The University of Pretoria's computer clusters, maintained by Hans Grobler, which greatly aided in my simulations.

CONTENTS

CONTENTS

LIST OF ABBREVIATIONS

ACI	Adjacent Carrier Interference
AWGN	Additive White Gaussian Noise
BER	Bit Error Rate
BW	Bandwidth
b/s/Hz	Bits per second per Hertz
CDMA	Code Division Multiple Access
CP	Cyclic Prefix
CSI	Channel State Information
DAST	Diagonal Algebraic Space-Time Codes
FDMA	Frequency Division Multiple Access
FFT	Fast Fourier Transform
FUSC	Full Usage of the Sub-Channel
IFFT	Inverse Fast Fourier Transform
ISI	Inter-Symbol Interference
LDPC	Low-Density Parity Check
LLR	Log-Likelihood Ratio
LOS	Line-Of-Sight
MAN	Metropolitan Arena Network
MAP	Maximum A Posteriori Probability
MMSE	Minimum Mean Square Error
MRC	Maximum-Ratio-Combining
MIMO	Multiple-Input-Multiple-Output
MISO	Multiple-Input-Single-Output

ML	Maximum Likelihood
MSE	Mean Square Error
NC	Nulling Cancelling
NLOS	Non-Line-of-Sight
OFDM	Orthogonal Frequency Division Multiplexing
OFDMA	Orthogonal Frequency Division Multiple Access
PAPR	Peak to Average Power Ratio
PDF	Probability Distribution Function
PDP	Power Delay Profile
PSD	Power Spectral Density
PSK	Phase Shift Keying
QAM	Quadrature Amplitude Modulation
SDA	Sphere Decoding Algorithm
SIMO	Single-Input-Multiple-Output
SISO	Single-Input-Single-Output
SNR	Signal-to-Noise-Ratio
SF	Space-Frequency
SFC	Space-Frequency Code
ST	Space-Time
STBC	Space-Time Block Code
STC	Space-Time-Code
STF	Space-Time-Frequency
STFC	Space-Time-Frequency code
TAST	Threaded Algebraic Space-Time Codes
TDMA	Time Division Multiple Access
UMTS	Universal Mobile Telecommunication System
UP	University of Pretoria
VIVU	Veelvuldige-Inset-Veelvuldige-Uitset
WB	Wideband
WiMAX	Worldwide Interoperability for Microwave Access
ZF	Zero Forcing

LIST OF SYMBOLS

$\rho(\alpha(t))$	Probability distribution function of the Rayleigh distribution
$\sigma^2_{\alpha(t)}$	Variance of the Rayleigh distribution
M_t	Number of transmit antennas
M_r	Number of receive antennas
$\mathbf{y}(k)$	Output vector at time instant k
$\mathbf{H}_l(k)$	Channel matrix at sampling time delay l and time instant k
$H^n_{i,j}(p)$	Channel frequency response from the j^{th} transmit antenna to the i^{th} receive antenna on the p^{th} subcarrier
$\mathbf{z}(k)$	AWGN vector at time instant k
L	Total number of independent fading paths
$\mathbf{\Psi}_{Tx}$	Correlation coefficient matrix at the transmitter
$\mathbf{\Psi}_{Rx}$	Correlation coefficient matrix at the receiver
$\mathbf{C}_{ISI}$	Covariance matrix of the inter-symbol interference filter tap coefficients
$\rho(n(t))$	Probability distribution function of the Gaussian distribution
E_s	Energy per symbol
E_b	Energy per bit
N_0	Single-sided power spectral density of AWGN
Θ_{M_t}	Linear complex precoder matrix based on algebraic rotation
M_b	Number of consecutive OFDM blocks used in the multi-antenna code
$\Lambda(x)$	Variable node degree distribution
$P(x)$	Check node degree distribution
$\lambda(x)$	Variable edge degree distribution

$\rho(x)$	Check edge degree distribution
x_k	Received binary representation for received vector at position k
$\lambda_L(x_k)$	Received log-likelihood value at the input of the decoder for x_k
$\mathcal{A}$	Constellation representation
$\lambda_A(x_k)$	A priori information for x_k
$\lambda_E(x_k)$	Extrinsic information for x_k
r	Exponential correlation parameter, varying from 0.0 - 1.0

LIST OF FIGURES

LIST OF TABLES

CHAPTER ONE
INTRODUCTION

1.1 HISTORY OF WIRELESS COMMUNICATION SYSTEMS

Wireless communication was introduced in 1901, when the first telegraph was sent across the Atlantic Ocean. Wireless communications have evolved over the last 40 years; the first generation cellular systems were introduced in the 1970s. First generation systems were analog systems designed for voice communications using frequency division multiple access (FDMA) as the underlying technology.

In the 1990s, second-generation cellular systems emerged, which are digital systems using time division multiple access or code division multiple access (CDMA) as the underlying technology. Second generation systems offer quality of service with increased spectral efficiency and enhanced capacity. Second generation systems are still in service in most countries today.

With the high demand on broadband wireless services, third generation cellular systems emerged, supporting very high data rates in the megabits per second region, as well as user mobility. Technologies used to employ the third generation systems include multi-carrier CDMA, direct-sequence CDMA and universal mobile telecommunication system (UMTS). Fourth generation systems are on the horizon with the aim of providing even higher data rates and user mobility. Technologies that follow the methodology for fourth generation systems include the Worldwide Interoperability for Microwave Access (WiMAX) standard [1], multiple-input multiple-output (MIMO) antenna system configurations and multi-antenna

codes, which include space-time codes, space-frequency codes and space-time-frequency codes.

1.2 WiMAX

The WiMAX standard consists of three physical layers based on the 802.16 MAN standard [1] and was developed by the WiMAX forum [2]. The physical layer used in this dissertation is the 802.16e2005 standard, which is also referred to as mobile WiMAX. The standard is defined for full mobility, operating in the frequency range up to 6 GHz. The 802.16e2004 standard supports very little mobility and operates in the frequency range up to 10 GHz. No line-of-sight (LOS) component is required in both standards for communication, but only the 802.16e2005 standard has handover capability.

The WiMAX standard uses scalable orthogonal frequency division multiplexing (OFDM), with various scalable factors, which include system bandwidth, Fast Fourier transform (FFT) size and number of subchannels, while still maintaining the same subcarrier frequency spacing. The standard also supports various modulation schemes, which can consist of QPSK, 16QAM and 64-QAM. Using OFDM as the underlying technology can be characterized by reduced complexity through the use of FFT processing, with higher throughput using orthogonal multi-carrier system compared to the traditional single carrier system and eliminating inter-symbol interference (ISI) by the use of a cyclic prefix.

1.3 MIMO

Capacity is defined as the maximum possible transmission rate to still maintain a negligible error probability. The single-input single-output (SISO) channel capacity for additive white Gaussian noise (AWGN) channels was first derived by Shannon in 1948 [3]. With the demand for larger capacity in cellular systems, it was shown that using MIMO antenna setups increases the channel capacity of the system [4]. The capacity increase when increasing the number of transmit and receive antennas is illustrated in this dissertation, as well as the effects of correlated conditions on the capacity of the system. Apart from increasing the capacity, MIMO systems have shown considerable improvements over single-antenna systems. The performance increase

can be characterized by more reliable throughput obtained through diversity. Diversity is the method of receiving multiple copies of the transmitted signal at the receiver, where each signal experiences its own channel fading conditions, reducing the probability that all signal replicas fade simultaneously. Evaluating the performance of the MIMO system in terms of bit error rate (BER) versus signal-to-noise ratio (SNR), the behaviour can be characterized as [5], [6]

$$\text{Probability of error} \quad \sim \quad G_c \cdot \text{SNR}^{-G_d} \tag{1.1}$$

where G_c is referred to as the coding gain, G_d is called the diversity gain and SNR is the signal-to-noise ratio of the system, usually normalized with respect to the noise equivalent bandwidth (see chapter 2). Plotting the error performance curve in a log-log scale of BER versus SNR, the diversity gain determines the slope of the curve obtained and the coding gain determines the parallel shift of the curve relative to the uncoded curve. The differences are illustrated in figure 1.1, where it is shown that the diversity gain plays a more important role than the coding gain in terms of showing an improvement in BER performance.

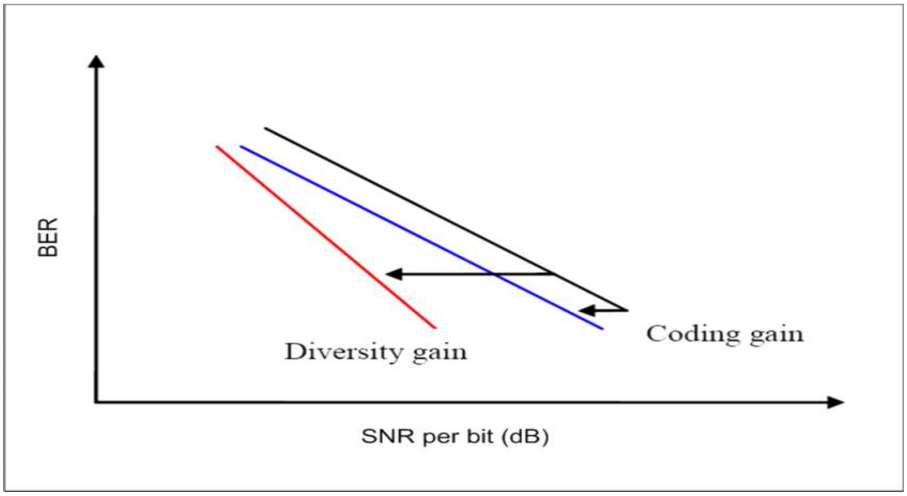

FIGURE 1.1: The difference between coding gain and diversity gain on a BER vs E_b/N_0 graph

In order to exploit the diversity, while still maintaining a suitable throughput rate, various multi-antenna coding schemes have been developed. Multi-antenna coding techniques to exploit space, time and frequency diversity are handled in this dissertation, combining the effects of realistic mobile channels with OFDM for high diversity systems. The multi-antenna codes can achieve high diversity gain, but only limited coding gain. For coding gain improvements, error correcting codes can be concatenated with the multi-antenna coding techniques.

1.4 OBJECTIVE OF THIS DISSERTATION

Most modern multi-antenna coding techniques are only evaluated in ideal mobile channel environments, assuming for each transmit and receive antenna pair either flat fading or frequency-selective fading with a low number of channel taps in the power delay profile (PDP). Additional assumptions include that the antennas at the transmitter, as well as at the receiver, are spaced far apart from one another, so that no correlation will occur at the transmitter or receiver. These assumptions simplify simulation implementation and produce very good results for these codes, but do not resemble results representing "real-world" scenarios, as the assumptions made are highly unlikely.

The first objective of the dissertation was to evaluate these coding techniques in a realistic mobile environment, which includes antenna correlation at the transmitter and receiver, as well as evaluating these coding strategies in PDPs consisting of a large number of channel taps. Recent coding technologies of space-time-frequency and high-rate space-frequency codes [7], to the author's knowledge, have not yet been evaluated under these channel conditions.

In order to evaluate these coding strategies in realistic mobile environments, a suitable MIMO channel model was created, which was computationally efficient as well as capable of simulating the following channel impairments:

- Frequency-selective fading conditions, using any defined PDP without increasing the sampling frequency in simulations
- Time-selective fading
- Space-selective fading, introduced by either an exponential correlation matrix or by actual placement of antennas at the transmitter and receiver, defining the angular spread as well as angle of arrival
- Quasi-static fading for the evaluation of the Alamouti space-time code, as well as the more realistic approach in block-fading conditions.

With mobile WiMAX in combination with MIMO technologies being a candidate for fourth generation technologies, the MIMO channel created was combined with WiMAX to create a MIMO-WiMAX simulation platform according to the WiMAX standard [1]. The

implementation is based on the 802.16e-2005 standard using scalable orthogonal frequency division multiple access (OFDMA) PHY air interface with full usage of the subchannel mode. Evaluating these coding strategies on a MIMO-WiMAX platform can form a set of newly defined codes, which can be incorporated into the standard complementing current single-symbol maximum likelihood (ML) codes as a guideline in designing real world MIMO-WiMAX systems.

The last objective was to evaluate the proposed coding scheme, which is a concatenation of a space-time-frequency code (STFC) with low-density parity check (LDPC) codes for a high performance MIMO system analysis. Proper soft outputs were derived for the STFC and used with a soft-output sphere decoder. To the author's knowledge, no soft-output values have been derived or used for the STFC defined in [7]. LDPC codes were designed using methods of density evolution, where the performance gain of the proposed STFC-LDPC outperformed the more conventional approach of combining space-time codes based on Alamouti's scheme with LDPC codes.

1.5 OUTLINE OF THE DISSERTATION

The dissertation starts by describing the mobile factors that have to be considered when simulating realistic mobile environments and how these factors were implemented in the MIMO channel model. Chapter 2 also describes the WiMAX platform, with a detailed description of the MIMO-WiMAX platform used for simulations.

Chapter 3 starts by giving an overview of multi-antenna coding strategies for flat fading channels and how these technologies were adapted and implemented for the MIMO-WiMAX standard in frequency-selective fading conditions. The chapter also illustrates how the soft output values were derived and concludes with a discussion of the LDPC codes and how they were designed for the STFC-LDPC concatenated coding scheme.

Chapter 4 begins with illustrating the operation of the sphere decoding algorithm, which was used to decode the multi-antenna codes based on algebraic rotations, concluding with a description of how soft-output values were calculated using a soft-output sphere decoding algorithm.

Chapter 5 presents the results obtained using the MIMO-WiMAX simulator with various realistic mobile environments. The dissertation is concluded in chapter 6 with concluding remarks and suggestions for future research.

1.6 CONTRIBUTIONS

The following international peer reviewed conference paper at IEEE WiMOB 2008 has been published with the work being directly based on the results from this research:

- K.P. Mare and B.T. Maharaj, *"Performance Analysis of modern Space-Time codes on a MIMO-WiMAX Platform"*, in Proc. IEEE WiMOB, Avignon, 12-14 Oct 2008, CDROM

The following conference paper was written and accepted to the IEEE ICC 2009 conference with work based on the results obtained from this research:

- K.P. Mare, B.P. Salmon and B.T. Maharaj, *Performance Gain of Space-Time-Frequency Concatenated LDPC Codes*, in Proc. IEEE ICC 2009, Dresden, Germany, 14-18 Jun 2009, accepted for publication

The following conference paper was co-authored and accepted to the IEEE WCNC 2009 conference with work based on the results obtained from this research:

- D.J. Basilio, K.P. Mare and B.T. Maharaj, *Performance of Space-Time-Frequency block-coded MC-DS-CDMA in Correlated conditions*, in Proc. IEEE WCNC 2009, Budapest, Hungary, 5-8 Apr 2009, accepted for publication

The following journal paper was written for submission to the IEEE Transactions in Wireless Communications with work based on the results obtained from this research:

- K.P. Mare, B.P. Salmon and B.T. Maharaj, *Performance Gain of Space-Time-Frequency Concatenated LDPC Codes*, in review IEEE Transactions in Wireless Communications

CHAPTER TWO

MIMO-WiMAX SIMULATION PLATFORM

2.1 INTRODUCTION

Creating suitable models to represent a realistic mobile environment for MIMO systems usually results in either statistically accurate and computationally inefficient ones or ones that are efficient but lacking in statistical properties. The aim of this chapter is to introduce the MIMO-WiMAX platform that was created, which used methods proposed in [8] to create a suitable MIMO channel for small-scale fading parameters, which includes various type of channels consisting of AWGN, frequency-selective fading, space-selective fading and time-selective fading. These selectivities are known as triply-selective fading conditions. The chapter will illustrate how these selectivities are introduced to conform to a suitable model representing realistic mobile environments for MIMO systems.

The simulator was implemented to conform to the IEEE 802.16e2005 (WiMAX) standard [1] which has been recognized as one of the most promising technologies with the advent of next generation broadband wireless communications. Using OFDM/OFDMA as the underlying technology enables the use of suitable multi-antenna coding techniques in conjunction with the WiMAX standard.

The chapter begins with a discussion on realistic mobile channels, with emphasis on characteristics suitable for small-scale fading channels used in this dissertation. A brief discussion on the various forms of diversity illustrates which selectivities are exploited to gain performance using OFDM, MIMO and multi-antenna coding techniques.

A detailed design and analysis is given on the implementation of the channel model to conform to these realistic mobile channel conditions mentioned, while still being computationally efficient compared to conventional channel model implementations.

The mobile WiMAX platform is discussed, as well as the way in which it is incorporated into the MIMO channel model that was created. OFDM is discussed in detail, as it is being used as the underlying technology. A description of the system block diagram, which is a concatenation of all the technologies described in this section, concludes the chapter. All the simulations and analyses in this dissertation were implemented using this model.

2.2 WIRELESS PROPAGATION EFFECTS

For the creation of a realistic mobile wireless environment, one has to consider challenges posed by wireless propagation to present simulation results which are statistically accurate. This section describes the factors influencing propagation in wireless channels and illustrates which effects are incorporated into the channel model created to form a realistic environment suitable for the performance analysis of next generation wireless technologies. It can be summarized as follows:

1. **Path loss :** As electromagnetic waves propagate through free space, their magnitude decays with distance and this is known as path loss. The power decay depends not only on distance, but also on the wavelength, transmit antenna gain, receive antenna gain and the propagation medium. The harshness of the wireless propagation medium constitutes the difference between wireless and fixed-line communications and gives rise to the implication that designers have to pay more attention to power efficiency.

2. **Shadowing, reflecting, diffracting and scattering :** A wireless environment can contribute to these effects as LOS operations are not always realistically possible. Obstacles that might block wireless transmission are known as shadowing, where some of the signal might be reflected if the size of the object is greater than the wavelength of the signal. With differently sized objects, the signal can also undergo scattering and diffraction, causing fading effects in the signal.

3. **Multipath propagation :** A signal which undergoes reflecting, diffracting and scattering reaches the receiver through various indirect paths, which add constructively and/or destructively to amplify or attenuate the signal. Each signal arriving may differ in amplitude, phase and carrier offset. The multiple versions of the signal cause a delay spread in the signal, which spreads the original signal in time, causing a smearing effect. The smearing effect causes ISI in a received signal.

4. **Fading effects :** Relative motion between the transmitter and receiver, as well as propagation medium changes, can contribute fading conditions along with multipath propagation. These effects cause time-varying paths as the signal changes over time. With varying amplitudes the signal can approach vanishing levels, which is known as fading. Fading effects can be divided into three categories:

   - Large-scale path loss effects modelled through an envelope which decays with distance.
   - Large- to medium-scale slowly varying shadowing effects modelled by a random amplitude following a log-normal distribution.
   - Small-scale fast varying effects modelled as a random channel amplitude using a Rice distribution for LOS components and a Rayleigh distribution for non-line-of-sight (NLOS) components.

The aim of the channel model was to create a realistic mobile environment, considering only small-scale fading propagation effects. The model opted for a worst case scenario with no LOS component present, where the channel amplitude only follows a Rayleigh distribution. The probability distribution function (PDF) of the Rayleigh distribution is given as follows [9]:

$$\rho(\alpha(t)) = \begin{cases} \frac{\alpha(t)}{\sigma^2_{b(t)}} \exp\left(-\frac{\alpha^2(t)}{2\sigma^2_{b(t)}} \right) & \text{if } 0 \leq \alpha(t) \leq \infty \\ 0 & \text{if } \alpha(t) \leq 0 \end{cases} \tag{2.1}$$

In the above equation, $\alpha(t)$ is the fading amplitude, $\sigma_{b(t)}$ is the root mean square value of the received signal before envelope detection and $\sigma^2_{b(t)}$ is the average power of the received signal. The statistical mean of the Rayleigh distribution is given as

$$\mathrm{E}[\alpha(t)] = \sqrt{\frac{\pi}{2}}\sigma_{b(t)}. \tag{2.2}$$

The variance of the Rayleigh distribution is given as

$$\sigma^2_{\alpha(t)} = \left(2 - \frac{\pi}{2}\right)\sigma^2_{b(t)}. \tag{2.3}$$

The next sub-section will highlight key parameters that define wireless channels which will be used for simulation purposes. These parameters will classify the channel and give a definition of the wireless propagation effects the MIMO-WiMAX platform is capable of simulating.

2.2.1 Wireless channel parameters and classification

The classification of wireless fading channels is presented in the following sub-sections.

2.2.1.1 Delay spread and coherence bandwidth

A symbol having a time duration of T_p, transmitted at a period of T_s, through a channel $h(\tau)$ having a delay spread of τ_d, will experience no ISI if $T_p + \tau_d \leq T_s$. The time dispersive channel can be analyzed in the time domain by comparing the delay spread τ_d with the signal period and transmission time. The comparisons between these parameters will decide the severity of the ISI. In the frequency domain the coherence bandwidth B_{coh} is defined as the interval over which frequencies will experience the same degree of fading and relates to the delay spread as follows:

$$B_{coh} \approx \frac{1}{\tau_d}\,. \tag{2.4}$$

The amount of ISI corresponds to the degree of frequency-selectivity, where the signal will experience either flat fading or frequency-selective fading depending on how the signal bandwidth (BW) compares with the coherence BW. The fading classifications based on the delay spread and coherence BW is summarized in figure 2.1.

2.2.1.2 Doppler spread and coherence time

A time-varying channel $h(t)$ will disperse the BW of a signal by an amount B_d, when a relative motion between the transmitter and receiver exists. This is due to the Doppler effect, where the

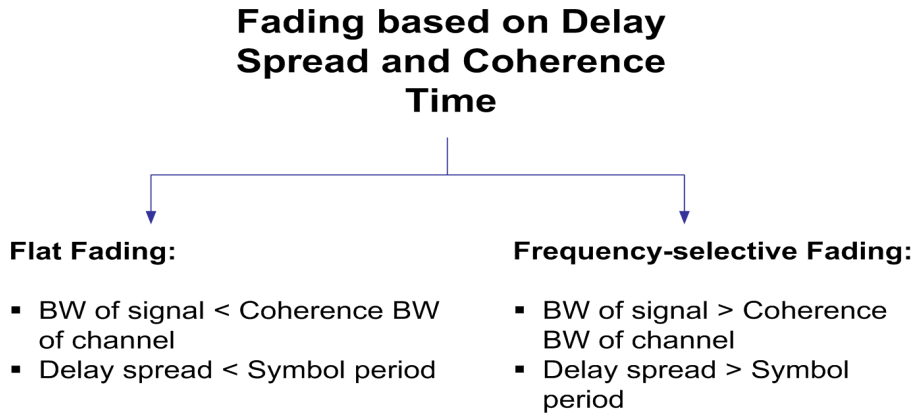

FIGURE 2.1: Summary of fading classification for delay spread and coherence bandwidth

amount B_d is known as the Doppler spread. For a symbol having a BW B_p and transmitted in successive bands spaced B_s Hz apart, it will have no overlapping frequencies if $B_s \geq B_p + B_d$. In the time domain, the coherence time T_{coh} is defined as a measure of the time duration over which the channel impulse response is essentially invariant and relates to the Doppler spread as follows:

$$T_{coh} \approx \frac{1}{B_d} . \tag{2.5}$$

The amount of overlapping frequencies corresponds to the degree of time-selectivity, where the signal will experience either fast fading or slow fading depending on how the signal duration compares with the coherence time. The fading classifications based on the Doppler spread and coherence time are summarized in figure 2.2.

2.2.1.3 Angular spread and coherence distance

Coherence distance is defined as the maximum distance for antennas to be separated in wavelengths so the channel impulse response can be assumed to be constant. For MIMO system analysis, this parameter is often neglected, where previous analysis on multi-antenna codes (see chapter 3) assumes that the antennas are spaced far apart from each other so that there is no correlation between transmit antennas and receive antennas. The coherence distance can be related to the behaviour of arrival directions of the reflected signals and is characterized by the angular spread [10].

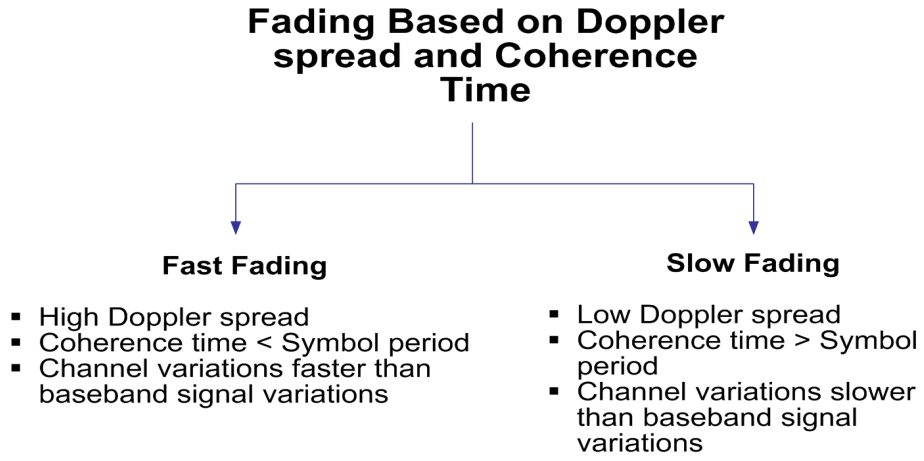

FIGURE 2.2: Summary of fading classification for Doppler spread and coherence time

When a channel is experiencing frequency-selective, time-selective and space-selective fading, the channel is known as a triply-selective channel. These selectivities introduced in this section categorize the wireless channel, where the platform created in this dissertation is capable of simulating these conditions, to present a realistic wireless environment for multi-antenna coding analysis. With the combination with WiMAX, the MIMO-WiMAX channel investigated consists of only frequency-selective fading and space-selective fading channels, since the performance evaluation of modern coding techniques in time-selective channels falls outside the scope of this dissertation. The WiMAX estimation techniques defined in [1] assumed that the channel remains constant over the whole OFDM/OFDMA codeword, which is defined as time-non-selective fading. The coding techniques defined in chapter 3 assume time-non-selective fading; techniques used for fast varying time-selective channels are presented in [11], [12], [13], [14], [15].

2.2.1.4 Quasi-static and block-fading channels

The implementation of the specific space-time codes (see chapter 3) requires the channel implementation to be quasi-static. Quasi-static fading conditions assume that the duration of the coherence time of the channel is constant for the whole codeword, which can consist of two or more OFDM/OFDMA symbols.

Assuming quasi-static fading conditions for system analysis and simulation is impractical, since realistic channel conditions will experience block-fading conditions. Block-fading conditions assume that the duration of the coherence time is constant for only one OFDM/OFDMA

symbol, but differs from one symbol to another. Coding over these blocks introduces another dimension of diversity, which is exploited in space-time-frequency codes (chapter 3).

The various channel conditions introduced and the way in which they are implemented in a computationally efficient way are discussed in subsequent sections, where codes are implemented and analyzed on a MIMO-WiMAX platform using frequency-selective, space-selective, quasi-static and block-fading conditions.

2.3 PROVIDING DIVERSITY GAIN THROUGH WIRELESS CHANNELS

This section describes the various methods of obtaining diversity, which are used in the multi-antenna coding techniques described in chapter 3. Diversity is referred to as the number of multiple copies received due to channel characteristics and MIMO implementations, which can be used in a suitable matter to increase system reliability and throughput. The following sub-sections illustrate the origin of the various forms of diversity and how they are collected for improved system performance.

2.3.1 Diversity through frequency-selective fading channels

Frequency-selective fading is due to delay spread and multipath channels as described in the previous section. These replicas that are received add degrees of freedom to the PDF, which contribute to less fading. Frequency diversity can be obtained if the same symbol is transmitted on multiple carriers that are separated pairwise in the frequency domain by at least as much as the coherence BW of the channel. Each symbol on each carrier will experience different fading characteristics, where the combined signal will improve the average error performance of the system. Various coding techniques, such as linear precoding (section 3.4), can be used to spread the symbol over various carriers without sacrificing throughput.

The MIMO-WiMAX platform makes use of frequency diversity by combining multi-antenna coding techniques with OFDM. Using OFDM in a frequency-selective fading channel enables each carrier to experience flat fading conditions, but fading characteristics will differ for each carrier in the system. Another method of enabling frequency diversity is through the use of

spread-spectrum transmission. Using spreading codes with good autocorrelation properties, a Rake receiver can effectively combine the multipath signals [16], [17].

2.3.2 Diversity through time-selective fading channels

Time-selective channels have the potential benefit that it is unlikely that the symbol will be lost due to a deep fade, when the channel varies over a symbol duration. Diversity can be obtained by using the techniques defined for frequency diversity in the time domain by using a symbol period that is equal to the coherence time of the channel and repeating the signal over various time instants. As stated previously, various techniques exist to enable diversity through coding and can be applied to time-selective fading conditions [14], [18]. Time-selective fading channels and coding thereof fall outside the scope of this dissertation.

2.3.3 Diversity through multiple transmit and receive antennas

Using multiple transmit and/or receive antennas gives rise to another degree of freedom called space diversity. Space diversity improves the error performance of the system without increasing the transmission bandwidth power or expanding the signal in the time domain. Various forms of multi-antenna diversity can be used and are described in the following sub-sections.

2.3.3.1 Single-input multiple-output channel

A system using M_r receive antennas and a single transmit antenna, gives rise to a single-input multiple-output (SIMO) channel. Each receive antenna receives a copy of the transmitted symbol, where the M_r receive antennas collect M_r times more power than a single antenna system, increasing the instantaneous SNR for the combined signal. These signals are usually extracted by combining techniques consisting of a maximum ratio combining (MRC) or equal-gain combiner. The output of these combiners consists of the sum of the degrees of freedom of all the paths in the system, which gives increased performance in fading channel, as the probability that two or more paths will experience the same degree of fading decreases with the increase in the number of receive antennas [19].

SIMO-based systems may not be viable in the downlink for wireless communications, as they may be ineffective as the handset size decreases, causing the antennas to be situated closer to

each other, as well as in view of the undesirable cost increase of packing multiple antennas at the mobile station.

2.3.3.2 Multiple-input single-output channel

A system using M_t transmit antennas and a single receive antenna gives rise to a multiple-input single-output (MISO) channel. Unlike SIMO systems, the transmit power has to be divided by $1/\sqrt{M_t}$ to ensure the power in the system stays the same, which causes the received power to be the same as for SISO channels. Obtaining diversity in MISO channels is different from SIMO channels, as the received signals are superimposed at the receive antenna and require multi-antenna coding techniques to enable diversity.

2.3.3.3 Multiple-input multiple-output channel

MIMO channels are the combination of the effects represented by SIMO and MISO channels. MIMO channels will be the focus in this dissertation; it was shown in [4], that the capacity for MIMO systems increases linearly with an increase in the number of transmit and/or receive antennas. For SISO channels, the capacity can only be increased logarithmically with an increase in SNR. A significant capacity increase can thus be achieved by MIMO systems without adding additional power or increasing the bandwidth of the system. A typical MIMO system is illustrated in [20] and presented in figure 2.3.

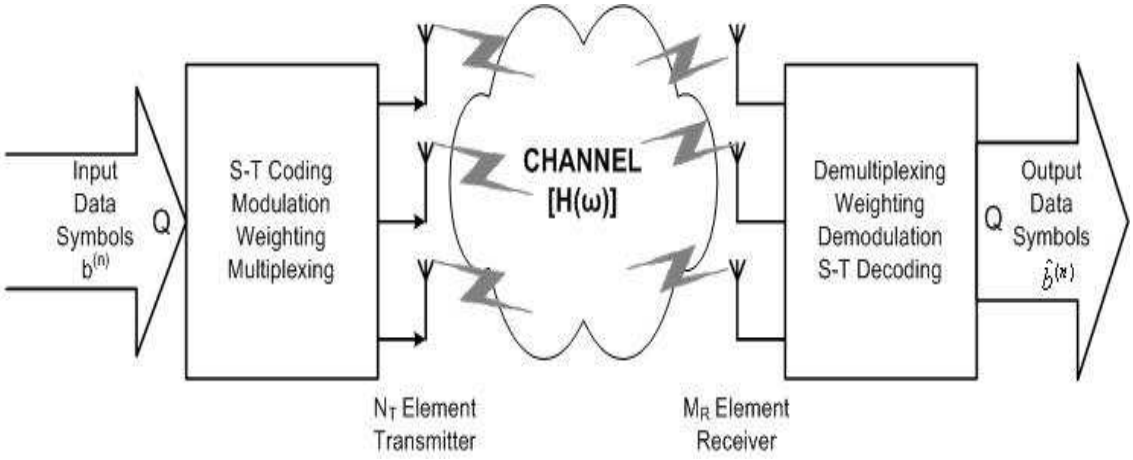

FIGURE 2.3: Space diversity provided by MIMO systems

After the data symbols have been created, they are encoded by a specific multi-antenna encoding technique to exploit the extra dimensions offered by the MIMO channel. The degrees of

freedom available in MIMO channels can further enhance the capacity and data rate well beyond those available in SISO channels [4]. The multi-antenna coding techniques presented in chapter 3 were used and designed for maximum diversity for MIMO channels, taking wireless channel impairments into consideration, which include frequency-selective fading, quasi-static fading, block-fading and space-selective fading. Besides error rate performance, the design of the multi-antenna codes must take into account a number of practical issues, which include receiver complexity, data rate and mobility.

2.4 SIMULATING WIRELESS PROPAGATION EFFECTS

This section describes how the wireless propagation effects discussed in the previous section are implemented in a simulation model so that it is statistically accurate and computationally efficient. It presents a detailed description of how the selectivities introduced in the previous section are incorporated into the channel's stochastic coefficients.

Small-scale frequency-selective fading channels are implemented by using a channel tap delay line model [16] to introduce delay spread and multipath propagation for wireless channel propagation. The tap delays are associated with the PDP simulated, where the multipath channel representing a PDP between any distinct pair of transmit and receive antenna is illustrated in figure 2.4.

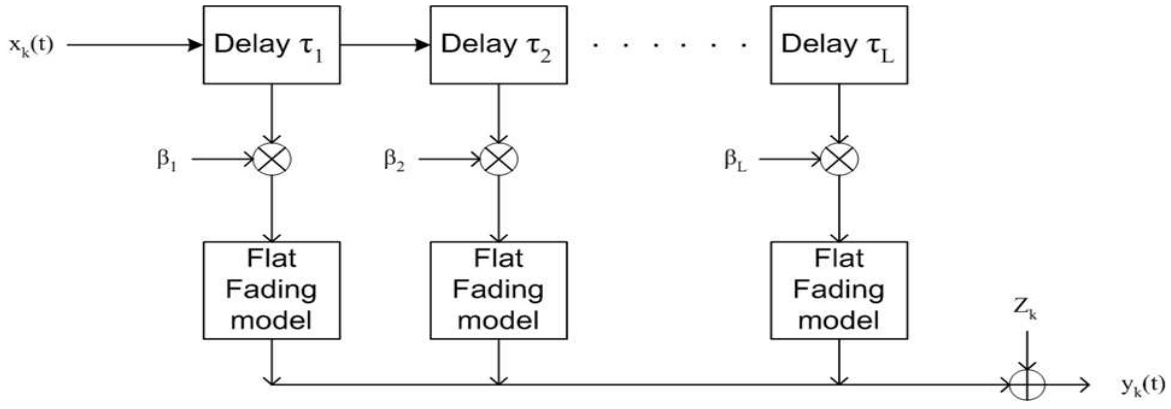

FIGURE 2.4: Conventional tapped delay line implementation of a multipath propagation channel

In figure 2.4 L is the total resolvable paths of the PDP with β_i and τ_i representing the power

and delay of the i^{th} tap respectively. The input signal x_k is delayed and scaled for each of the L propagation paths according to the predefined PDP used in the simulation. After the L propagation paths are combined at the receiver, they are corrupted by the AWGN term Z_k, which is generated as illustrated in section 2.4.1. The flat fading modules are generated by using improved models based on Jake's fading model (see section 2.4.2) or by using Clarke's model [21].

The problem with conventional models as presented in figure 2.4 is that if the number of propagation paths L is large or if the relative path delays are small between adjacent paths, the computational requirement to represent the channel accurately can be unfeasible or inefficient. This is due to the oversampling requirement needed to approximate channels with multiple fractionally delayed fading paths.

For example, say the input signal uses one sample per symbol at $T_s = 0.1\mu s$. If the values for $\tau_1 = 0.3\mu s$ and $\tau_2 = 1.0\mu s$, the relative delays can be incorporated as a simple 3-sample delay for τ_1 and a 10-sample delay for τ_2. When using a different PDP, with $\tau_1 = 0.12\mu s$ and $\tau_2 = 1.45\mu s$, the input signal has to be oversampled by a factor of 10 to simulate the new PDP presented accurately. This can become unfeasible for an extremely high value for L, as the simulation time can increase dramatically when high oversampling is required. In addition, the sampling rate can possibly change for every implementation of a different PDP, which makes the simulation of any PDP for a simulation model a tedious task.

A platform suitable to present any PDP accurately without increasing the sampling frequency was presented in [8]. Techniques presented here were used to form the channel model for the MIMO-WiMAX platform, where the channel coefficients used in the tap delay line translate the effects of the channel model into the receiver's sampling spaced stochastic channel coefficients. Not only frequency-selective fading conditions are translated into the coefficients, but also space-selective fading, as well as having the capability of incorporating time-selective fading. In addition to these selectivities that were introduced, the model also translates the effects of the transmit and receive filter into the sample spaced tap delay model, so that no oversampling or additional overhead is needed for the filterting operations. The sampling spaced channel tap delay line model used with the MIMO-WiMAX platform is illustrated in figure 2.5.

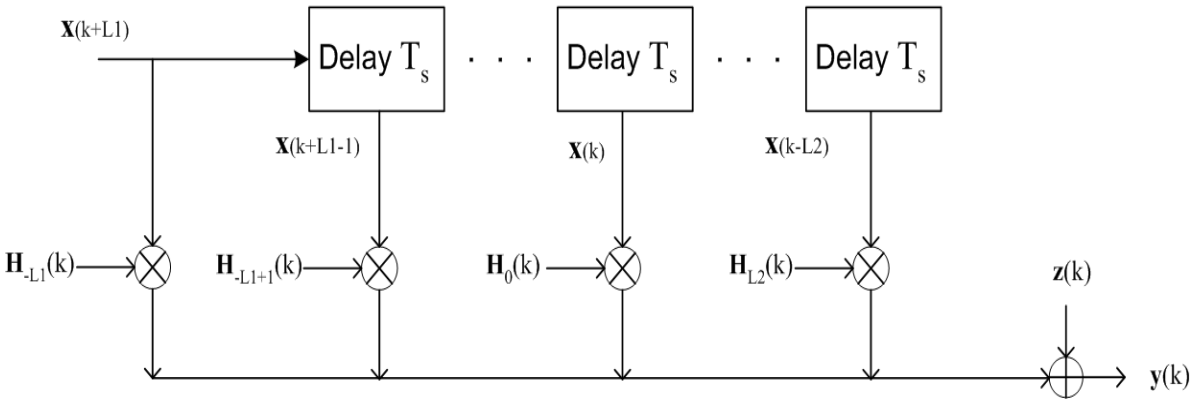

FIGURE 2.5: Discrete-time MIMO sample spaced tap delay line channel model

The following equation defines the output of the channel illustrated in figure 2.5 as

$$\mathbf{y}(k) = \sum_{l=-L1}^{L2} \frac{1}{\sqrt{M_t}} \mathbf{H}_l(k).\mathbf{x}(l-k) + \mathbf{z}(k) \tag{2.6}$$

where k represents the time instant, $L1$ and $L2$ are positive numbers so that $L_1 + L_2 + 1 = L$, where L represents the total number of coefficients used for the combined channel impulse response, which includes the number of propagation paths in the PDP as well as the transmit and receive filter effects. The length of L is chosen to include approximately $97\% - 99.9\%$ of the total system power in a truncated tapped delay line sample spaced model. The values of $L1$ and $L2$ in equation 2.6 are determined by the maximum delay spread of the physical channel as well as the time durations of the transmit and receive filters. The non-casuality of the tapped delay line model is introduced by combining the effects of the transmit and receive filters into the channel response.

The input vector $\mathbf{x}(k)$ represents the $M_t \times 1$ time domain representation of the OFDM/OFDMA baseband signal which is received from the WiMAX transmitters, where M_t represents the total number of transmit antennas and $\mathbf{z}(k)$ represents the AWGN vector with zero mean and variance $N_0/2$, generated as illustrated in section 2.4.1. The input of the channel at each transmit antenna is scaled by a normalization factor $1/\sqrt{M_t}$ to ensure that the power received for each receive antenna is independent of M_t. The output vector $\mathbf{y}(k)$ represents the combined output for all the sample spaced tap delays, corrupted by AWGN at time instant k.

For every l in the tapped delay line model, the channel matrix can be represented as

$$\mathbf{H}_l(k) = \begin{bmatrix} h_{1,1}(k,l) & \dots & h_{1,M_t}(k,l) \\ \vdots & \ddots & \vdots \\ h_{M_r,1}(k,l) & \dots & h_{M_r,M_t}(k,l) \end{bmatrix} \tag{2.7}$$

where M_r represents the total number of receive antennas. The generation of the values for the channel coefficients is represented in [8], where the values for $h_{m,n}(k,l)$ are indexed from the following equation:

$$\mathbf{h}_v(k) = \left[\mathbf{h}_{1,1}(k), ..., \mathbf{h}_{1,M_t}(k) | \dots | \mathbf{h}_{M_r,1}(k), ..., \mathbf{h}_{M_r,M_t}(k)\right]^{\mathcal{T}}. \tag{2.8}$$

In the above equation $\mathcal{T}$ represents the transpose operation and $\mathbf{h}_{m,n}$ is the m^{th} receive antenna and n^{th} transmit antenna pair's stochastic channel coefficients at time instant k and is given as

$$\mathbf{h}_{m,n}(k) = \left[h_{m,n}(k, L1) \dots h_{m,n}(k, L2)\right]. \tag{2.9}$$

The channel model consists of a total of $M_t M_r L$ channel coefficients. The generation of $\mathbf{h}_v(k)$ from which the channel coefficients are indexed is given as [8]

$$\mathbf{h}_v(k) = \left(\mathbf{\Psi}_{Rx}^{1/2} \otimes \mathbf{\Psi}_{Tx}^{1/2} \otimes \mathbf{C}_{ISI}^{1/2}\right).\mathbf{\Phi}(k) \tag{2.10}$$

where $\otimes$ denotes the Kronecker product [22]. In equation 2.10, $\mathbf{\Psi}_{Rx}$ and $\mathbf{\Psi}_{Tx}$ denote the correlation coefficient matrices at the receiver and transmitter respectively and are given as

$$\mathbf{\Psi}_{Rx} = \begin{bmatrix} \rho_{R_x}^{(1,1)} & \dots & \rho_{R_x}^{(1,M_r)} \\ \vdots & \ddots & \vdots \\ \rho_{R_x}^{(M_r,1)} & \dots & \rho_{R_x}^{(M_r,M_r)} \end{bmatrix} \tag{2.11}$$

and

$$\mathbf{\Psi}_{Tx} = \begin{bmatrix} \rho_{T_x}^{(1,1)} & \dots & \rho_{T_x}^{(1,M_t)} \\ \vdots & \ddots & \vdots \\ \rho_{T_x}^{(M_t,1)} & \dots & \rho_{T_x}^{(M_t,M_t)} \end{bmatrix}. \tag{2.12}$$

Space-selective fading is introduced by proper design of $\mathbf{\Psi}_{Rx}$ and $\mathbf{\Psi}_{Tx}$. The space-selective fading can either be introduced according to antenna spacing and angular spread using techniques defined in [23] or by using an exponential correlation matrix [24] defined as

$$\rho_{R_x}^{(m,p)} = r^{|m-p|},\ \rho_{T_x}^{(n,q)} = r^{|n-q|},\ |r| \leq 1 \tag{2.13}$$

where parameter r can vary from 0 to 1, representing 0% to 100% correlation respectively.

In equation 2.10, $\mathbf{C}_{ISI}$ represents the covariance matrix of the inter-symbol interference filter tap coefficients of equation 2.9. The $\mathbf{C}_{ISI}$ parameter translates the effects of the transmit filter, the channel fading parameters and the receive filter into the receiver's sampling-period spaced stochastic channel coefficients. The design of $\mathbf{C}_{ISI}$ [8] ensures that no oversampling is needed to handle multiple fractionally delayed power delay profiles, which ensures a computational complexity reduction compared to conventional tap delay line implementations and is given as

$$\mathbf{C}_{ISI} = \begin{bmatrix} c(-L1,-L1) & \dots & c(-L1,L2) \\ \vdots & \ddots & \vdots \\ c(L2,-L1) & \dots & c(-L2,L2) \end{bmatrix} \tag{2.14}$$

with $c(l_1, l_2)$ calculated as

$$c(l_1,l_2) = \sum_{i=1}^{K} \beta_i \overline{R}_{P_T P_R}(l_1 T_s - \tau_i)\overline{R}^{*}_{P_T P_R}(l_2 T_s - \tau_i). \tag{2.15}$$

In equation 2.15, K represents the total number of resolvable paths from the PDP[1], β_i and τ_i represent the power and delay of the i^{th} tap from the PDP respectively and $\overline{R}_{P_T P_R}$ is the convolution function of the transmit filter P_T and receive filter P_R.

For example, for a system with a sampling frequency of $T_s = 0.87\mu s$, using square root raised cosine filters for P_T and P_R with a roll of factor of $\alpha = 0.3$ using a Vehicular A PDP (see Appendix A) defined in the UMTS standard [25], the $\mathbf{C}_{ISI}$ matrix can be represented as follows:

[1] The total number of paths from the PDP does not necessarily equal the number of taps in the tapped delay line model from figure 2.5.

TABLE 2.1: $\mathbf{C}_{ISI}$ for the Vehicular A profile

$c(l_1, l_2)$	$l_2 = -1$	$l_2 = 0$	$l_2 = 1$	$l_2 = 2$	$l_2 = 3$
$l_1 = -1$	0.0077	-0.0447	-0.0242	0.0055	-0.0007
$l_1 = 0$	-0.0447	0.7930	0.1387	-0.0317	0.0038
$l_1 = 1$	-0.0242	0.1387	0.1695	-0.0087	0.0000
$l_1 = 2$	0.0055	-0.0317	-0.0087	0.0246	-0.0009
$l_1 = 3$	-0.0007	0.0038	0.0000	-0.0009	0.0053

From the above table we can see that $L = 5$ for a sample spaced tapped delay line for the Vehicular A PDP. All taps are included to include 99% of the total system power, where paths for $L \geq 5$ have little impact on the output of the signal and are discarded. The diagonal of the values illustrated in table 2.1 represents the total power of the truncated system.

From equation 2.15, $\mathbf{\Phi}(k)$ represents an uncorrelated Rayleigh flat fading vector created using improved methods for Jake's model as described in section 2.4.2. Changes in the generation of $\mathbf{\Phi}(k)$ values at different time instants can determine if the channel is experiencing time-selective, quasi-static or block-fading conditions. Specifying the Doppler spread for the flat fades (see section 2.4.2) and creating new channel coefficients at certain time instants can introduce the time selectivity. By choosing an appropriate Doppler spread and only generating new flat fades for every codeword, one will introduce quasi-static fading conditions. These flat fades can be introduced per OFDM/OFDMA block and not every codeword, which will give rise to block-fading conditions.

The triply-selective fading conditions can be introduced by proper design of the above parameters. Space-selectivity is introduced by $\mathbf{\Psi}_{Rx}$ and $\mathbf{\Psi}_{Tx}$ and frequency-selectivity by $\mathbf{C}_{ISI}$ and $\mathbf{\Phi}(k)$, where changes in the generation of $\mathbf{\Phi}(k)$ values at different time instants and choosing an appropriate value for the Doppler spread can determine if the channel is experiencing time-selective fading. As mentioned, time-selective fading techniques are not part of the dissertation, where the channel model was used in a MIMO-WiMAX platform to evaluate modern coding techniques, as well as doing a performance evaluation on the proposed LDPC-STFC concatenated code (chapter 3) in frequency-selective, space-selective, quasi-static and block-fading conditions.

The channel coefficients generated by the channel model were used at the receiver to supply perfect channel state information (CSI) for the multi-antenna coding techniques. No estimation of channel parameters was done, as the process of estimating CSI for MIMO fading channels is a topic not handled in this dissertation.

2.4.1 Generating AWGN samples

The AWGN samples generated for the noise in the tap delay line model follow a Gaussian distribution given as

$$\rho(n(t)) = \frac{1}{\sqrt{2\pi}\sigma_n} \exp\left(\frac{-n^2(t)}{2\sigma^2_{n(t)}}\right) \tag{2.16}$$

where $\sigma^2_{x(t)}$ represents the noise variance. The noise samples were generated using the Bray-Marsagalia algorithm [26], which transforms uniformly distributed variables into a Gaussian distributed variable with zero mean and unit variance. Uniform distributed variables were generated using the Wichmann-Hill algorithm [27], which has a sufficient repetition length for suitable statistics to simulate a communication system using millions of samples.

The performance evaluation of the MIMO-WiMAX platform was measured in terms of BER versus E_b/N_0. and is defined as the normalization of the SNR with respect to the noise equivalent bandwidth. The reason for using an E_b/N_0 value for performance measurements is that it is an independent variable, where performance evaluation can be compared to other systems without the need of the noise equivalent bandwidth. The relationship between SNR and E_b/N_0 is presented in [28], assuming the output signal is received through a noise-limiting filter, and is given as follows:

$$\text{SNR} = \frac{\sigma^2_{s(t)}}{\sigma^2_{n(t)}} = \frac{E_b.f_{bit}}{N_0 \int_0^\infty |H_{Rx}(f)|^2 df} = \frac{E_c.(f_{bit}/R_c)}{N_0 \int_0^\infty |H_{Rx}(f)|^2 df}. \tag{2.17}$$

In the above equation, $\sigma^2_{s(t)}$ represents the power of the transmitted signal, $\sigma^2_{n(t)}$ the variance of the Gaussian noise sample, E_b the energy in the uncoded bit, N_0 the power spectral density (PSD) of the noise, E_c the energy in coded bit with R_c representing the code rate and f_{bit} the uncoded bit rate. The noise variance can be presented in terms of the specified E_b/N_0 in dB from the above equation as follows [28]:

$$\sigma^2_{n(t)} = \frac{\sigma^2_{s(t)} \int_0^\infty |H_{Rx}(f)|^2 df}{10^{(\frac{1}{10}E_b/N_0)}.f_{bit}}. \tag{2.18}$$

If the noise samples from the Bray-Marsagalia algorithm are generated at a rate of f_{samp} Hz with unit variance, the output of the receive filter can be presented as follows [28]:

$$\sigma^2_{r(t)} = \frac{2}{f_{samp}} \int_0^\infty |H_{Rx}|^2 df. \tag{2.19}$$

With the required noise scaling given in equation 2.18, a factor k_n is derived by which the generated noise samples have to be scaled in order to produce the correct variance for a specific E_b/N_0 and is given as follows [28]:

$$k_n = \frac{\sigma^2_{n(t)}}{\sigma^2_{r(t)}} = \frac{\sigma^2_{s(t)}.f_{samp}}{10^{(\frac{1}{10}E_b/N_0)}.2.f_{bit}}. \tag{2.20}$$

The k_n factor presented in equation 2.20 was extended to include OFDM transmission in [29] and was used in the implementation of the MIMO-WiMAX platform. For the MIMO-WiMAX platform using N_{FFT} tones and a cyclic prefix (CP) length consisting of N_{CP} time domain symbols, the total sample length of the OFDM symbol can be presented as [29]:

$$N_{Total} = N_{FFT} + N_{CP}. \tag{2.21}$$

In addition, another term N_{bit} is defined, which represents the uncoded bit rate for all sub-carriers and is defined as [29]

$$N_{bit} = \sum_{j=1}^{N} f_{bit,j} \tag{2.22}$$

where $f_{bit,j}$ represents the uncoded bit rate for the j^{th} carrier, summed over all carriers. The new k_n value for the MIMO-WiMAX platform can then be illustrated by the following equation [29]:

$$k_n = \frac{\sigma^2_{s(t)}.f_{samp}.N_{Total}}{10^{(\frac{1}{10}E_b/N_0)}.2.N_{FFT}.N_{bit}}. \tag{2.23}$$

The scaling factor of $1/\sqrt{M_t}$ in the tap delay line from equation 2.6 ensures that the signal power is independent of the number of transmit antennas M_t and has no impact on the generation of noise samples for a specific E_b/N_0 value.

2.4.2 Generating uncorrelated Rayleigh flat fades using Jake's model

The multiple uncorrelated fades in equation 2.10 were generated using improved models based on Jake's original model [30]. The original model has problems in generating more than three uncorrelated flat fades, as well as not being wide sense stationary. Improvements were made in [31] to remove non-stationary problems and all statistical deficiencies were removed in [32] and [33]. The model in the latter two references was used to form the uncorrelated flat fades in equation 2.10.

The l^{th} Rayleigh fade with $l = 1...M_tM_rL$ at time instant k for the $M_tM_rL \times 1$ matrix $\mathbf{\Phi}(k)$ from equation 2.10 is generated from the improved Jake's models as

$$Z^l(k) = Z_c^l(k) + jZ_s^l(k) \tag{2.24}$$

$$Z_c^l(k) = \sqrt{\frac{2}{M}} \sum_{n=1}^{M} \cos\left[2\pi f_d k \cos(\alpha_n) + \phi_n\right] \tag{2.25}$$

$$Z_s^l(k) = \sqrt{\frac{2}{M}} \sum_{n=1}^{M} \cos\left[2\pi f_d k \sin(\alpha_n) + \gamma_n\right] \tag{2.26}$$

$$\alpha_n = \frac{2\pi n - \pi + \theta}{4M}, \qquad \text{for} \quad n = 1, 2...M \tag{2.27}$$

where ϕ_n, γ_n and θ are statistically independent and uniformly distributed on $[-\pi, \pi)$ for all n. M in the above equations represents the number of sinusoids and it was found that $M \geq 8$ would be sufficient for the approximation of the Rayleigh fading process [33]. f_d represents the maximum Doppler spread introduced in the simulations.

2.5 MOBILE WiMAX PLATFORM

WiMAX represents an industry consortium to promote and support the adoption of the IEEE 802.16 family of standards. The standard was ratified in 2005 to include mobility with a targeted maximum speed of the mobile stations in the range of 125 km/h [1]. The mobile WiMAX physical layer specifications adopt OFDM and OFDMA modulation for improved performance in frequency-selective fading channels in NLOS environments and are discussed in section 2.5.1. A simulation platform for mobile WiMAX was developed in [29] and [34] for SISO systems. In this dissertation, the mobile WiMAX platform was extended for use with MIMO, to analyze modern multi-antenna coding techniques, as well as the proposed STFC-LDPC concatenated scheme in various channel conditions.

The simulation platform incorporates the Wireless MAN OFDMA air interface using Full Usage of the Subchannel (FUSC) mode with MIMO. FUSC was chosen for implementation as it is used for outer cell communications representing a worst case scenario compared to Partial Usage of the Subchannel (PUSC). PUSC has more control over the network, offering quality of service and is used for inner cell communication. For PUSC implementation, most of the parameters would remain unchanged, as the advantages PUSC offers compared to FUSC are not handled in this study. The OFDM symbol is constructed to conform to the standard [1] and is illustrated in figure 2.6.

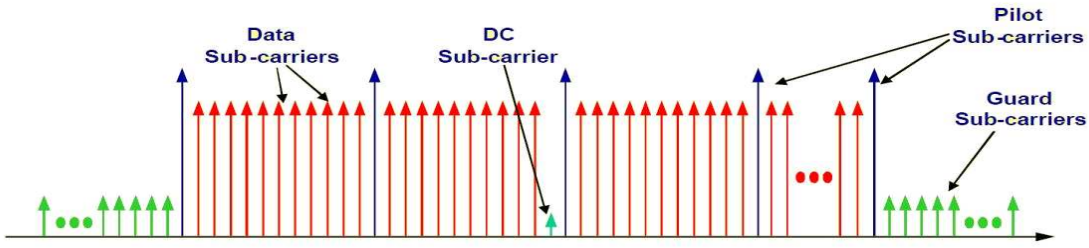

FIGURE 2.6: OFDMA WiMAX symbol structure

The WiMAX symbol structure consists of data carriers, which are divided into subchannels and carry the payload information. The guard bands are used to reduce adjacent carrier interference (ACI). The pilot tones are used with channel estimation and synchronization techniques. The

pilot tones consist of fixed as well as variable pilot tones, where the variable pilot tones are linearly displaced depending on the OFDM symbol number [1].

In the amendment to the IEEE 802.16, scalable OFDMA is introduced to support various channel bandwidths in the $1.25 - 20$ MHz range. The scalability is introduced by adjusting the FFT size, while keeping the sub-carrier frequency spacing constant at 10.94 kHz. Scalability parameters used in the simulation platform are defined in [1] and summarized as follows:

TABLE 2.2: OFDMA scalable parameters defined for the MIMO-WiMAX platform

System bandwidth (MHz)	1.25	2.5	10	20
FFT size	128	512	1024	2048
Number of subchannels	2	8	16	32
Subcarrier frequency spacing (kHz)	10.94	10.94	10.94	10.94

The simulations in chapter 5 were all simulated using the parameters of the first column in table 2.2. The parameters were chosen for computational efficiency and reduced simulation time. Accurate results in realistic frequency-selective fading conditions were maintained due to the high delay spread of the PDPs chosen for simulations. Along with the scalability, mobile WiMAX supports various modulation schemes, which include BPSK, QPSK, 16-QAM and 64-QAM. Although the pilot tones were placed according to the WiMAX standard [1], perfect CSI was assumed at the receiver and extracted directly from the channel model, as estimation techniques were not handled in this dissertation.

2.5.1 OFDM modulation

OFDM is the underlying technology used with the MIMO-WiMAX platform, where OFDM converts the multi-antenna transmission over frequency-selective fading channels to a set of flat fading channels. The advantage of multi-carrier systems over single-carrier alternatives is that the set of flat fading channels reduces the complexity in equalization and decoding. Using OFDM with MIMO over frequency-selective fading channels enables three dimensions to be exploited, namely space (multiple antennas), frequency (multi-carriers) and time (block fading).

As OFDM transmission is the same between any distinct pair for transmit antennas M_t and receive antennas M_r, OFDM is first presented for the single antenna case and then extended for

MIMO. For the n^{th} OFDM symbol, the frequency domain representation of the input signal for the N-carrier single antenna OFDM system is presented as

$$\mathbf{x}_n = [\ x_n(0)\ x_n(1)\ \ldots\ x_n(N-1)]^{\mathcal{T}}. \tag{2.28}$$

The OFDM transmitter uses the $N \times 1$ input signal and obtains the time domain representation of the OFDM symbol $\mathbf{F}_N^{\mathcal{H}}\mathbf{x}_n$, by applying an N-point inverse fast Fourier transform (IFFT) $\mathbf{F}_N^{\mathcal{H}}$. Before the signal is transmitted over the channel, the resultant time domain representation is lengthened by a guard interval, known as the CP. The CP adds the last J entries of the time domain representation to the front to increase the length of the signal to P, where $P = N + J$. The transmitted signal is represented as

$$\mathbf{T}_{cp}\mathbf{F}_N^{\mathcal{H}}\mathbf{x}_n = [\ x_n^c(0)\ x_n^c(1)\ \ldots\ x_n^c(P-1)\ ]^{\mathcal{T}} \tag{2.29}$$

where the CP can be represented as follows:

$$\mathbf{T}_{cp} = \begin{bmatrix} \mathbf{0}_{L\times(N-J)} | \mathbf{I}_J \\ \mathbf{I}_N \end{bmatrix}. \tag{2.30}$$

$\mathbf{0}_{(a\times b)}$ represents an all zero matrix of size $a \times b$ and $\mathbf{I}$ represents the identity matrix. If L is the channel order of the frequency-selective fading channel, there will be no ISI between consecutive OFDM symbols if the length of J is selected larger than or equal to the channel order. The ISI is confined in the CP portion, where removal of the CP at the receiver converts the linear convolution with the channel to a circular convolution [35]. When the signal is received and the CP is removed, the n^{th} received symbol can be represented as

$$\mathbf{y}_n = \tilde{\mathbf{H}}\mathbf{F}_N^{\mathcal{H}}\mathbf{x}_n + \mathbf{w} \tag{2.31}$$

where $\mathbf{w}$ denotes the complex AWGN vector, which is circularly symmetric with a variance scaled according to a specific E_b/N_0 value as described in section 2.4.1. $\tilde{\mathbf{H}}$ is a $N \times N$ circulant channel matrix represented as

$$\tilde{\mathbf{H}} = \begin{bmatrix} h(0) & 0 & \dots & h(L) & \dots & h(1) \\ \vdots & h(0) & \dots & \dots & \ddots & \vdots \\ \vdots & \dots & \ddots & \dots & \ddots & h(L) \\ h(L) & \dots & \dots & \ddots & \dots & 0 \\ \vdots & \ddots & \dots & \dots & \ddots & \vdots \\ 0 & \dots & h(L) & \dots & \dots & h(0) \end{bmatrix}. \tag{2.32}$$

From the properties of circulant matrices [36], the matrix $\tilde{\mathbf{H}}$ can be diagonalized with the use of FFT and IFFT matrices as

$$\mathbf{H}_D = \mathbf{F}_N \mathbf{x}_n \mathbf{F}_N^{\mathcal{H}} = \text{diag}(\ H(0), H(1), H(2)\ \ \dots\ \ H(N-1)\ ) \tag{2.33}$$

where $H(p) = \sum_{l=0}^{L} h(l) e^{-j2\pi lp/N}$ with $h(l)$ representing the l^{th} tap of the tap delay line model. Using this property on the received signal $\mathbf{y}_n$ yields:

$$\mathbf{y}_n^D = \tilde{\mathbf{H}} \mathbf{F}_N^{\mathcal{H}} \mathbf{y}_n = H_D \mathbf{x}_n + \mathbf{w}^D. \tag{2.34}$$

In the above equation $\mathbf{w}^D$ represents the FFT processed noise $\mathbf{w}$. Equation 2.34 can be presented for the n^{th} OFDM symbol as follows:

$$y_n(p) = H(p) x_n(p) + w_n(p) \qquad p = 0, ..., N-1. \tag{2.35}$$

The above equation illustrates how the the frequency-selective fading channel is converted into a set of frequency flat channels for $p = 0, ..., N-1$. The equation also illustrates that a simple division of $H(p)$ for each $y_n(p)$, $p = 0, ..., N-1$ can be done for equalization. The disadvantage of using OFDM is its sensitivity to carrier drifts and high peak-to-average-power ratio (PAPR) that IFFT processing introduces.

Equation 2.35 holds for any pair of transmit and receive antenna and can be extended for a MIMO platform, using M_t transmit antennas and M_r receive antennas as follows:

$$y_n^i(p) = \frac{1}{\sqrt{M_t}} \sum_{j=1}^{M_t} H_{i,j}^n(p) x_{n,j}(p) + w_n^i(p), \qquad i = 1, ..., M_r. \tag{2.36}$$

Equation 2.36 illustrates the received MIMO signal after CP removal and FFT processing for the i^{th} receive antenna and p^{th} subcarrier. The received symbol $y_n(p)$ comprises the superposition of OFDM symbols transmitted from all M_t antennas and is illustrated for the n^{th} received OFDM symbol. $H_{i,j}(p)$ is extended from equation 2.35 to represent the channel frequency response from the j^{th} transmit antenna to the i^{th} receive antenna evaluated on the p^{th} subcarrier as follows:

$$H_{i,j}^n(p) = \sum_{l=0}^{L} h_{i,j}^n(l) e^{\frac{-j2\pi lp}{N}}. \tag{2.37}$$

$x_{n,j}(p)$ from equation 2.36 represents the transmitted signal from the j^{th} transmit antenna, n^{th} OFDM symbol and p^{th} subcarrier.

OFDM, in combination with MIMO, gives rise to degrees of freedom that can be exploited in multi-antenna coding techniques. Chapter 3 illustrates how OFDM was used for the use of the multi-antenna coding techniques on the MIMO-WiMAX platform.

2.6 THE MIMO-WiMAX INTERFACE SIMULATOR

The functional layout of the MIMO-WiMAX Wireless MAN-OFDMA physical layer simulator is illustrated in Figure 2.7. The simulator was developed in C++, where each one of the blocks in Figure 2.7 illustrates the basic operation of the simulator.

Before the simulator starts, the appropriate channel information is created from a PDP using equation 2.15 in MATLAB. The values are stored appropriately and indexed in the simulator to calculate equation 2.10 to produce the channel taps at the correct time interval according to the simulation parameters.

The source bits are randomly generated by block 1 and contain no redundancy, which is typical of data produced by source encoding and compression methods. After the information bits are

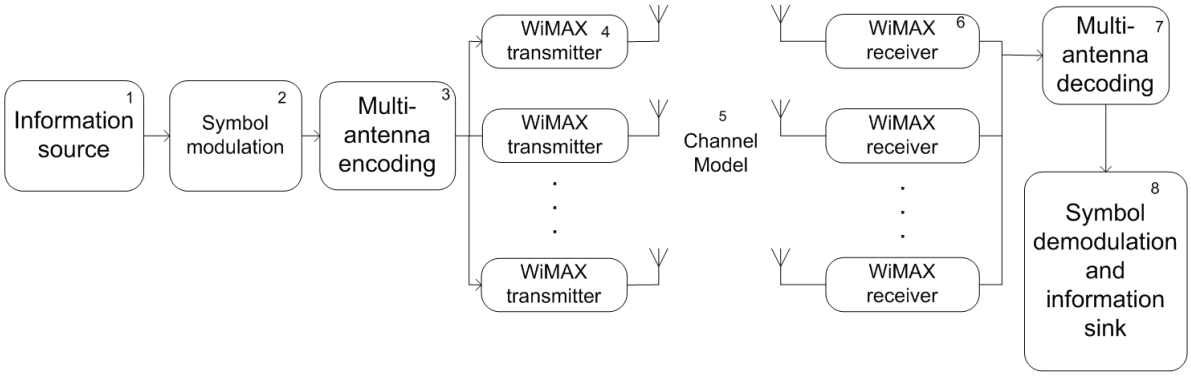

FIGURE 2.7: Simulator platform for the MIMO-WiMAX interface

generated, they are modulated (block 2) in the frequency domain with the specific modulation scheme, which can consist of BPSK, QPSK, 16-QAM and 64-QAM.

After modulation, the symbols are grouped appropriately and encoded using a multi-antenna coding technique (chapter 3) defined in the simulation parameters. These coding techniques consist of space-time codes, space-frequency codes, space-time-frequency codes or a concatenation scheme of space-time coded LDPC or space-time-frequency coded LDPC. The encoded symbols are spread to each of the M_t transmit antennas according to the type of coding technique used.

The downlink bursts used within this simulator were simulated using the Wireless MAN-OFDMA-PHY layer specifications. In block 4 the OFDMA symbol is created by placing the frequency domain encoded symbols, guard bands, pilot tones and DC frequency bands to conform to the WiMAX specifications using the FUSC mode. These pilot tones and data carriers are linearly displaced for each OFDMA symbol in a downlink burst. The downlink burst consists of a preamble OFDMA symbol, followed by 24 OFDMA symbols. The pre-amble OFDMA symbol is collected according to the three segment numbers and identification cell number from the predefined pre-amble database. Each OFDMA symbol constructed is converted into a time domain sequence by computing the corresponding IFFT and is followed by appending a sufficient length CP of the OFDMA symbol to the transmission sequence.

The downlink bursts were simulated over a channel represented by block 5. All the OFDMA symbols in the downlink burst were simulated over the channel model created (section 2.4). The channel parameters include the selectivities described in section 2.4 for a system using any M_t transmit antennas and any M_r receive antennas.

Block 6 is the WiMAX receiver, whose main function is to demultiplex the received frame for each M_r-receive antenna and to allocate the appropriate symbols to the corresponding user. The data symbols are retrieved by using the same permutation vectors as specified in the WiMAX transmitter (block 4). The symbols associated with each user are sent to the multi-antenna decoder. For the space-time codes, a single-symbol ML detector is used, but for the space-frequency (SF) and space-time-frequency (STF) codes, sphere decoding methods had to be used (chapter 3 and 4). The LDPC concatenated decoding schemes had to produce soft outputs (chapter 3), where the LDPC codes were decoded using Pearl-Belief propagation as described in [37].

After decoding, the information symbols for each user are demodulated using the appropriate scheme defined at the modulation block. The payload for each user is fed to the receiver sink (block 8) to obtain the number of errors that have occured for a given RF signal quality.

2.7 CONCLUSION

This chapter discussed the various wireless propagation effects of realistic mobile environments and how these channel conditions were incorporated into a statistically accurate and computationally efficient channel model. The mobile WiMAX platform was discussed with a representation of the way in which the OFDM symbols are formed for the FUSC mode. OFDM was discussed in detail and the chapter concluded with a functional diagram on how the channel model and mobile WiMAX platform were incorporated to form the MIMO-WiMAX channel model, which was used for all simulations and analyses in this dissertation.

CHAPTER THREE

MODERN CODING TECHNIQUES FOR MULTI-ANTENNA SYSTEMS

3.1 INTRODUCTION

Using multiple transmit and receive antennas has shown considerable improvement over single antenna systems. The performance increase can be characterized by more reliable throughput obtained through diversity and a higher achievable data rate through spatial multiplexing. To achieve the larger capacity offered by MIMO systems, various multi-antenna coding schemes can be used to exploit the many degrees of freedom available in wireless channels. Critical to this enhanced rate and performance is the proper design of multi-antenna coding schemes to account for challenging propagation channels and receiver complexity. The multi-antenna coding schemes in this section are assessed primarily on diversity gain, where each coding scheme will be evaluated on throughput rate in symbols per channel use and maximum achievable diversity gain.

The chapter begins with an overview of multi-antenna coding schemes for flat fading channels. These space-time (ST) codes can exploit a diversity order of $M_r M_t$, where M_r is the number of receive antennas and M_t the number of transmit antennas. For frequency-selective fading channels the design complexity increases owing to ISI. Code designs are discussed for the MIMO-WiMAX platform, which uses OFDM as an underlying technology to combat ISI, as OFDM transforms a broadband frequency-selective fading channel into a set of parallel flat fading channels [38]. These code designs for OFDM are known as SF codes and STF codes. SF codes can obtain a diversity order of $M_r M_t L$, where L is the number of independent fading

paths. Using block-fading conditions, another dimension of diversity is exploited in the design of STF codes. These codes obtain a diversity order of $M_r M_t L M_b$, where M_b is the number of consecutive independent fading blocks used in the STF code design. The high rate SFC and STFC [7] as well as the full rate SFC [39] and space-time block codes (STBCs) [40] for $M_t > 2$, make use of algebraic rotations to obtain full diversity. A brief overview and introduction on the design of these matrices are discussed. The last section of the chapter will be an overview of LDPC codes, which were used in conjunction with the multi-antenna codes to increase the coding gain on the BER performance.

The codes in this chapter form the basis for the performance analysis of the MIMO-WiMAX platform in realistic wireless propagation channels. For all the multi-antenna codes, the maximum rate and diversity gain will be discussed, as well as encoding and decoding methods. The aim of this chapter is to introduce these coding technologies and the methods to incorporate them in a MIMO-WiMAX platform. These coding technologies form the basis for the performance evaluation of the concatenation of LDPC codes and multi-antenna codes in block-fading conditions.

3.2 MULTI-ANTENNA CODING FOR FLAT FADING CONDITIONS

In this section, STBCs for flat fading channels are briefly discussed. These codes form the basis from which codes for frequency-selective fading conditions are designed using MIMO-OFDM principles. The ST codes for frequency selective channels are designed from the concepts of the orthogonal STBC for flat fading conditions. The principles of combining algebraic rotations and layering with orthogonal codes were first introduced by the diagonal algebraic space-time (DAST) (section 3.2.2) and threaded algebraic space-time (TAST) (section 3.2.3) codes and form the basis for the construction of the high-rate full diversity SF/STF codes. The channel for all the codes in this section was assumed to be i.i.d. Gaussian with quasi-static flat fading, where the system model can be represented as

$$\mathbf{Y} = \frac{1}{\sqrt{M_t}} \mathbf{H}.\mathbf{C}^{\mathcal{T}} + \mathbf{W} \tag{3.1}$$

where the superscript $\mathcal{T}$ represents the matrix transpose operation, $\mathbf{Y}$ represents an $M_r \times U$ received vector, where U represents the number of consecutive blocks used with the code in which the channel remains quasi-static. $\mathbf{C}$ represents the $U \times M_t$ STBC, which is encoded from a block of p information symbols $\mathbf{S}$ and can be illustrated as follows:

$$\mathbf{C} = \begin{bmatrix} g_{1,1} & g_{2,1} & \cdots & g_{M_t,1} \\ g_{1,2} & g_{2,2} & \cdots & g_{M_t,2} \\ \vdots & \vdots & \vdots & \vdots \\ g_{1,U} & g_{2,U} & \cdots & g_{M_t,U} \end{bmatrix}. \tag{3.2}$$

The entries $g_{i,j}$, where $i = 1...M_t$, are transmitted simultaneously from transmit antennas $1, ..., M_t$ in each time slot $j = 1, ..., U$. It can be seen that the encoding is carried out in both space and time; hence the term space-time coding. In equation 3.1, $\mathbf{H}$ represents the $M_r \times M_t$ MIMO channel and can be expressed as follows:

$$\mathbf{H} = \begin{bmatrix} h_{1,1} & h_{1,2} & \dots & h_{1,M_t} \\ h_{2,1} & h_{2,2} & \dots & h_{2,M_t} \\ \vdots & \vdots & \ddots & \vdots \\ h_{M_r,1} & h_{M_r,2} & \dots & h_{M_r,M_t} \end{bmatrix}. \tag{3.3}$$

The entries $h_{i,j}$ denote the channel gain between the j^{th} transmit antenna and the i^{th} receive antenna. $\mathbf{W}$ in equation 3.1 represents an $M_r \times U$ additive white complex Gaussian noise vector with zero mean and variance $\frac{N_0}{2}$, which is scaled according to a specific $\frac{E_b}{N_0}$ value. The normalization factor $\frac{1}{\sqrt{M_t}}$ ensures that the specific $\frac{E_b}{N_0}$ value used for simulation purposes at each receive antenna is independent of M_t.

For two distinct ST codewords, $\mathbf{C}$ and $\tilde{\mathbf{C}}$, the following notation for Δ is defined, which will be used in subsequent equations:

$$\Delta = (\mathbf{C} - \tilde{\mathbf{C}})(\mathbf{C} - \tilde{\mathbf{C}})^{\mathcal{H}}. \tag{3.4}$$

The superscript $\mathcal{H}$ in the above equation represents the Hermitian operation. The pairwise error-probability between $\mathbf{C}$ and $\tilde{\mathbf{C}}$ can then be upper-bounded by [18]

$$P(\mathbf{C} \rightarrow \tilde{\mathbf{C}}) \leq \left(\prod_{i=1}^{r} \lambda_i \right)^{-M_r} \left(\frac{E_s}{4N_0 M_t} \right)^{rM_r} \tag{3.5}$$

where r denotes the rank of matrix $(\mathbf{C} - \tilde{\mathbf{C}})$, and λ_i for $i = 1...r$ are the nonzero eigenvalues of Δ. Based on this upper-bound, two design criteria for STBC for quasi-static flat fading conditions were proposed as follows [18]:

- *Diversity (rank) criterion:* The minimum rank of the difference matrix $(\mathbf{C} - \tilde{\mathbf{C}})$ over all pairs of distinct codeword $\mathbf{C}$ and $\tilde{\mathbf{C}}$ should be as large as possible.
- *Product criterion:* The minimum value of the product $\prod_{i=1}^{r} \lambda_i$ over all pairs of distinct codewords $\mathbf{C}$ and $\tilde{\mathbf{C}}$ should be maximized.

To achieve maximum diversity of $M_t M_r$ for STBC, the difference matrix $(\mathbf{C} - \tilde{\mathbf{C}})$ should be full rank for any pair of distinct codewords $\mathbf{C}$ and $\tilde{\mathbf{C}}$. The following sub-sections will discuss several STBC that form the basis for the design of STC, SFC and STFC for frequency-selective fading channels. These codes have major considerations in implementation, where a tradeoff has to be made between diversity gain, transmission rate and receiver complexity.

3.2.1 Orthogonal space-time block codes

ST codes can in general be classified into two categories: ST trellis codes and STBCs. ST trellis codes perform extremely well at the cost of relatively high decoding complexity [18], [41]. Orthogonal STBC design, which was first proposed by Alamouti [42], has a simple ML-detection property, alleviating problems introduced by ST trellis codes. The code was originally defined for two transmit antennas and one receive antenna where the transmission matrix for $M_t = 2$ and $U = 2$ is as follows:

$$\mathbf{C} = \begin{bmatrix} S_1 & S_2 \\ -S_2^* & S_1^* \end{bmatrix}. \tag{3.6}$$

The superscript $*$ denotes the complex conjugate operation. The Alamouti STBC provides full diversity $M_t M_r$ at a rate of one symbol per channel use and simple-single ML detection. Using orthogonal designs, similar schemes were derived in [43] for cases of more than two transmit antennas. An example of a full diversity, $1/2$-rate code with $M_t = 3$ and $U = 8$ is as follows:

$$\mathbf{C} = \begin{bmatrix} S_1 & S_2 & S_3 \\ -S_2 & S_1 & -S_4 \\ -S_3 & S_4 & S_1 \\ -S_4 & -S_3 & S_2 \\ S_1^* & S_2^* & S_3^* \\ -S_2^* & S_1^* & -S_4^* \\ -S_3^* & S_4^* & S_1^* \\ -S_4^* & -S_3^* & S_2^* \end{bmatrix}. \tag{3.7}$$

For special cases of three and four transmit antennas, a rate of $3/4$ code can be constructed. An example of a full diversity $3/4$-rate code with $M_t = 3$ and $U = 4$ is as follows:

$$\mathbf{C} = \begin{bmatrix} S_1 & S_2 & \frac{S_3}{\sqrt{2}} \\ -S_2^* & S_1^* & \frac{S_3}{\sqrt{2}} \\ \frac{S_3^*}{\sqrt{2}} & \frac{S_3^*}{\sqrt{2}} & \frac{(-S_1 - S_1^* + S_2 - S_2^*)}{2} \\ \frac{S_3^*}{\sqrt{2}} & -\frac{S_3^*}{\sqrt{2}} & \frac{(S_2 + S_2^* + S_1 - S_1^*)}{2} \end{bmatrix}. \tag{3.8}$$

It was proved in [44] that the maximum achievable data rate for more than two antennas cannot be greater than $3/4$.

3.2.2 Diagonal algebraic space-time codes

In order to reach the maximum achievable rate of $3/4$ for more than two transmit antennas, methods where proposed in [40], [45] to combine STBC with algebraic rotations (see section 3.4) and the Hadamard transform to yield full-diversity STBC for flat fading conditions at a rate of one symbol per channel use. These codes are called DAST codes and were shown to outperform original STBC for more than two antennas while still maintaining a rate of one symbol per channel use. The code structure for the DAST codes can be represented as

$$\mathbf{C}^{\mathcal{T}} = \mathcal{H}_{ad} diag(x_1 \;\; x_2 \;\; \ldots \;\; x_{M_t}) \tag{3.9}$$

where $\mathcal{H}_{ad}$ represents an $M_t \times M_t$ Hadamard matrix and $[x_1 \; x_2 \; \ldots \; x_{M_t}]^{\mathcal{T}} = \Theta_{M_t}[s_1 \; s_2 \; \ldots \; s_{M_t}]^{\mathcal{T}}$, where Θ_{M_t} represents the linear complex precoder matrix based on algebraic rotation (section

3.4) and $[s_1\ s_2\ ...\ s_{M_t}]$ the information symbol vector consisting of phase shift keying (PSK) or quadrature amplitude modulation (QAM) constellations.

The use of the Hadamard matrix is to reduce the peak-to-mean envelope power ratio, but limits the number of transmit antennas to $M_t = 1, 2$ or any multiple of four [40]. Methods were later proposed in [46] to construct a full diversity DAST code for any number of transmit antennas. These codes don't use the Hadamard matrix as defined in equation 3.9, but design the linear complex precoder matrix Θ_{M_t} to be unitary for any number of transmit antennas (section 3.4). The DAST codes form a lattice structure where ML decoding can be implemented using sphere decoding methods (chapter 4).

3.2.3 Threaded algebraic space-time codes

The STBCs described in previous sections were designed with the main objective to achieve the highest possible diversity provided by MIMO channels while attaining rates no higher than one symbol per channel use. For most values of M_t, this rate is significantly lower than the actual capacity of MIMO systems. Code designs were proposed in [47] to exploit the fundamental capacity limits of MIMO channels while still maintaining full diversity. These codes are known as TAST codes, which are capable of achieving rate M_t as well as full diversity.

TAST codes are constructed by combining ST layering concepts with algebraic rotations as used with DAST codes. Each code is assigned to a "thread" in the space-time matrix, where the Diophantine approximation theory [47] is used to make threads "transparent" to one another. For $M_t = 2$, the code design using two symbols per channel, is illustrated as

$$\mathbf{C}^{\mathcal{T}} = \begin{bmatrix} x_{1,1} & \phi x_{2,1} \\ \phi x_{2,2} & x_{1,2} \end{bmatrix} \tag{3.10}$$

where the codes are created as $[x_{1,1}\ x_{1,2}]^{\mathcal{T}} = \Theta_{M_t}[s_1\ s_2]^{\mathcal{T}}$ and $[x_{2,1}\ x_{2,2}]^{\mathcal{T}} = \Theta_{M_t}[s_3\ s_4]^{\mathcal{T}}$. Θ_{M_t} represents the linear complex precoder matrix based on algebraic rotation (section 3.4) and s_1, s_2, s_3, s_4 the information symbols consisting of PSK or QAM constellations.

A general structure for $M_t \geq 3$ can be represented as [6]:

$$\mathbf{C}^{\mathcal{T}} = \begin{bmatrix} x_{1,1} & \phi x_{2,1} & \dots & \phi^{M_t-1} x_{M_t,1} \\ \phi^{M_t-1} x_{M_t,2} & \phi x_{1,2} & \dots & \phi^{M_t-2} x_{M_t-1,2} \\ \vdots & \vdots & \ddots & \vdots \\ \phi x_{2,M_t} & \phi^2 x_{3,M_t} & \dots & x_{1,M_t} \end{bmatrix} \tag{3.11}$$

where $[x_{n,1}\ x_{n,2}\ ...\ x_{n,M_t}]^{\mathcal{T}} = \Theta_{M_t}[s_{M_t(n-1)+1}\ ...\ s_{M_t(n-1)+M_t}]^{\mathcal{T}}$ for $n = 1, ..., M_t$, where Θ_{M_t} represent the linear complex precoder matrix based on algebraic rotation (section 3.4) and $s_1, ..., s_{M_t^2}$ the information symbols consisting of PSK or QAM constellations.

As with the DAST codes, TAST has a lattice structure, where ML detection is performed using sphere decoding (section 4).

3.3 MULTI-ANTENNA CODING FOR FREQUENCY-SELECTIVE CONDITIONS

Using WiMAX in a broadband wireless environment results in a frequency-selective fading channel. The design of the codes defined in the previous section is suitable for flat fading conditions, since design is more complex in frequency-selective fading conditions due to ISI. The MIMO-WiMAX platform that was created uses OFDM as an underlying technology, translating the frequency-selective fading channel into a set of parallel flat fading channels. These parallel flat fading channels are used as virtual antennas, where another dimension of diversity is exploited.

The coding principles introduced in the previous section are used to define coding techniques suitable for the MIMO-WiMAX platform in frequency-selective fading channel conditions. The coding techniques in this section are derived in a form suitable for OFDM, presenting a design criterion as well as examples for code construction, hard-output decoding, and soft-output decoding used with the LDPC codes.

The codes for the MIMO-WiMAX platform are illustrated using a channel model consisting of M_t transmit antennas, M_r receive antennas and N tones of an OFDM for each user. The frequency-selective fading channels between different transmit and receive antenna pairs are

assumed to have L independent paths and the same power delay profile. Each code is described for M_b consecutive OFDM blocks, where the path gains remain constant for each OFDM block. For the codes defined in section 3.3.2, the channel gains remain quasi-static over the whole codeword, which consists of two OFDM blocks ($M_b = 2$). The STF codes in section 3.3.4 are defined for block-fading conditions, where the gains will be independent for each OFDM block n, where $n = 1...M_b$.

After CP removal and FFT processing for the i^{th} receive antenna and p^{th} subcarrier, the received symbol $y_n(p)$ comprises the superposition of OFDM blocks transmitted from all M_t antennas and is illustrated for the n^{th} received OFDM block as

$$y_n^i(p) = \frac{1}{\sqrt{M_t}} \sum_{j=1}^{M_t} H_{i,j}^n(p) c_{n,j}(p) + w_n^i(p), \qquad i = 1, ..., M_r \tag{3.12}$$

where $H_{i,j}(p)$ is the channel frequency response from the j^{th} transmit antenna to the i^{th} receive antenna evaluated on the p^{th} subcarrier as

$$H_{i,j}^n(p) = \sum_{l=0}^{L} h_{i,j}^n(l) e^{\frac{-j2\pi lp}{N}}. \tag{3.13}$$

The channel impulse response $h_{i,j}^n(l)$ can be extracted directly from the model defined in chapter 2. In equation 3.12, $w_n^i(p)$ represents the additive white complex Gaussian noise with zero mean and variance $\frac{N_0}{2}$, which is scaled according to a specific $\frac{E_b}{N_0}$ value. The normalization factor $\frac{1}{\sqrt{M_t}}$ ensures that the specific $\frac{E_b}{N_0}$ value used for simulation purposes at each receive antenna is independent of M_t. The codeword symbols $c_{n,j}(p)$ for each transmit antenna, OFDM tone and OFDM block are encoded from information symbols consisting of PSK or QAM symbols, which are normalized to unity power.

All the codewords presented for the WiMAX platform will be illustrated in the format of equation 3.14, where the values for $c_{n,j}(p)$ are indexed from equation 3.15, ie

$$\mathbf{G} = \left[\begin{array}{cccc} \mathbf{C}_1 & \mathbf{C}_2 & ... & \mathbf{C}_{M_b} \end{array} \right]. \tag{3.14}$$

$\mathbf{C}_n$ is a $N \times M_t$ matrix denoting the sub-codeword sent at OFDM block n and represented as

follows:

$$\mathbf{C}_n = \begin{bmatrix} \mathbf{c}_{n,1} & \mathbf{c}_{n,2} & \dots & \mathbf{c}_{n,M_t} \end{bmatrix} = \begin{bmatrix} c_{n,1}(0) & c_{n,2}(0) & \dots & c_{n,M_t}(0) \\ c_{n,1}(1) & c_{n,2}(1) & \dots & c_{n,M_t}(1) \\ \vdots & \vdots & \ddots & \vdots \\ c_{n,1}(N-1) & c_{n,2}(N-1) & \dots & c_{n,M_t}(N-1) \end{bmatrix}. \tag{3.15}$$

The channel frequency response matrix for OFDM block n over all subcarriers N, receiver antennas i and transmitter antennas j can be illustrated by the following $M_r N \times M_t N$ matrix as

$$\mathbf{H}_n = \begin{bmatrix} \mathbf{\Lambda}^n_{1,1} & \mathbf{\Lambda}^n_{1,2} & \dots & \mathbf{\Lambda}^n_{1,M_t} \\ \mathbf{\Lambda}^n_{2,1} & \mathbf{\Lambda}^n_{2,2} & \dots & \mathbf{\Lambda}^n_{2,M_t} \\ \vdots & \vdots & \ddots & \vdots \\ \mathbf{\Lambda}^n_{M_r,1} & \mathbf{\Lambda}^n_{M_r,2} & \dots & \mathbf{\Lambda}^n_{M_r,M_t} \end{bmatrix} \tag{3.16}$$

where

$$\mathbf{\Lambda}^n_{i,j} = \begin{bmatrix} H^n_{i,j}(0) & 0 & 0 & 0 \\ 0 & H^n_{i,j}(2) & 0 & 0 \\ \vdots & \vdots & \ddots & \vdots \\ 0 & 0 & 0 & H^n_{i,j}(N-1) \end{bmatrix} \tag{3.17}$$

represents the $N \times N$ diagonal matrix form of equation 3.13. Using the direct sum of matrices, equation 3.16 can be extended in terms of the direct sum operation "$\oplus$" over all OFDM blocks for the codeword as follows:

$$\mathbf{H} = \mathbf{H_1} \oplus \mathbf{H_2} \oplus \dots \oplus \mathbf{H_{M_b}}. \tag{3.18}$$

The mathematical operation for the direct sum of matrices can be defined for any arbitrary matrices $\mathbf{A}$ (of size $m \times n$) with entries $a_{m,n}$ and $\mathbf{B}$ (of size $p \times q$) with entries $b_{p,q}$ as follows:

$$\mathbf{A} \oplus \mathbf{B} = \begin{bmatrix} a_{1,1} & \dots & a_{1,n} & 0 & \dots & 0 \\ \vdots & \dots & \vdots & \vdots & \dots & \vdots \\ a_{m,1} & \dots & a_{m,n} & 0 & \dots & 0 \\ 0 & \dots & 0 & b_{1,1} & \dots & b_{1,q} \\ \vdots & \dots & \vdots & \vdots & \dots & \vdots \\ 0 & \dots & 0 & b_{p,1} & \dots & b_{p,q} \end{bmatrix}. \tag{3.19}$$

For the codes used in section 3.3.2, quasi-static fading conditions were assumed, where entries for $\mathbf{H_1}...\mathbf{H_{M_b}}$ would experience the same gain. For the STFC in section 3.3.4, each $\mathbf{H_n}$ in equation 3.18 would experience gains independent from all the others.

Using equation 3.18 the output of equation 3.12 can be presented in matrix form as

$$\mathbf{Y} = \mathbf{HC} + \mathbf{W} \tag{3.20}$$

where $\mathbf{H}$ is of size $M_r N M_b \times M_t N M_b$, $\mathbf{Y}$ is of size $M_r N M_b \times 1$ and $\mathbf{C}$ is of size $M_t N M_b \times 1$ defined as

$$\mathbf{C} = \begin{bmatrix} \mathbf{X}_1 & \mathbf{X}_2 & \dots & \mathbf{X}_{M_b} \end{bmatrix}^{\mathcal{T}} \tag{3.21}$$

where $\mathbf{X}_n$ can be defined using equation 3.15 as follows:

$$\mathbf{X}_n = \begin{bmatrix} \mathbf{c}_{n,1}^{\mathcal{T}} & \mathbf{c}_{n,2}^{\mathcal{T}} & \dots & \mathbf{c}_{n,M_t}^{\mathcal{T}} \end{bmatrix}. \tag{3.22}$$

The power normalization term is neglected in the above equations for notational brevity. Sphere decoding in chapter 4 is used to decode the codes presented in section 3.3.3 and section 3.3.4, by deriving the outputs in the form of equation 3.20.

Let $\mathbf{C}$ and $\tilde{\mathbf{C}}$ be two matrices related to two codewords $\mathbf{G}$ and $\tilde{\mathbf{G}}$ respectively. Using notation

$$\Delta = (\mathbf{C} - \tilde{\mathbf{C}})(\mathbf{C} - \tilde{\mathbf{C}})^{\mathcal{H}} \tag{3.23}$$

and

$$\mathbf{R} = E[\mathbf{H}\Delta\mathbf{H}^{\mathcal{H}}] \tag{3.24}$$

the pairwise error probability between $\mathbf{C}$ and $\tilde{\mathbf{C}}$ can then be upper-bounded by [48], [49], [50]

$$P(\mathbf{C} \rightarrow \tilde{\mathbf{C}}) \leq \left(\begin{array}{c} 2r-1 \\ r \end{array} \right) \left(\prod_{i=1}^{r} \lambda_i \right)^{-1} \left(\frac{E_s}{N_0 M_t} \right)^{-r} \tag{3.25}$$

where r is the rank of $\mathbf{R}$ and λ_i for $i = 1...r$ are the nonzero eigenvalues of $\mathbf{R}$. Based on this upper-bound, two general design criteria for multi-antenna codes for frequency-selective fading conditions can be proposed as follows:

- *Diversity (rank) criterion:* The minimum rank of $\mathbf{R}$ over all pairs of distinct codeword $\mathbf{C}$ and $\tilde{\mathbf{C}}$ should be as large as possible.
- *Product criterion:* The minimum value of the product $\prod_{i=1}^{r} \lambda_i$ over all pairs of distinct codewords $\mathbf{C}$ and $\tilde{\mathbf{C}}$ should be maximized.

With the primary interest of full diversity codes, it was shown in [50], [39] that the rank r for SF codes ($M_b = 1$) is given by

$$r \quad \leq \quad min\{M_r N, M_r M_t L\} \tag{3.26}$$

and for STF codes [7] as

$$r \quad \leq \quad min\{M_r M_b N, M_r M_t M_b L\} \tag{3.27}$$

with additional criteria for the block-fading sum criterion and block-fading product criterion defined in [6], [7].

3.3.1 Diversity product of space-frequency codes

If an SF code achieves full diversity, the normalized coding advantage can be represented by the diversity product [50], [39], which can be decomposed as the product of the intrinsic diversity product and extrinsic diversity product. It was shown in [39] that if $\prod_{k=1}^{LM_t} |x_k - \tilde{x_k}| \neq 0$ for any distinct pair of codewords $\mathbf{X} = [x_1\ x_2\ ...\ x_{LM_t}]$ and $\tilde{\mathbf{X}} = [\tilde{x_1}\ \tilde{x_2}\ ...\ \tilde{x_{LM_t}}]$ the SF code achieves a diversity order of $M_t M_b L$ and the diversity product is as follows:

$$\zeta = \zeta_{in}\zeta_{ex}. \tag{3.28}$$

The intrinsic diversity product ζ_{in} depends solely on the signal constellation used, as well as the code construction of the SF code. The extrinsic diversity product ζ_{ex} depends solely on the power delay profile of the channel. The mathematical derivation of the intrinsic diversity is illustrated in [39] and is as follows:

$$\zeta_{in} = \frac{1}{2} \min_{\mathbf{X} \neq \tilde{\mathbf{X}}} \left(\prod_{k=1}^{LM_t} |x_k - \tilde{x_k}| \right)^{\frac{1}{LM_t}}. \tag{3.29}$$

To maximize the intrinsic diversity product, it is desirable to design the set of symbols $\mathbf{X}$ such that the minimum product distance is as large as possible. Maximizing the minimum product distance is associated with the problem of constructing signal constellations for fading channels. One approach is to use a precoder matrix based on algebraic rotations. The precoder design to maximize the minimum product distance is discussed in section 3.4 and is used with the SF codes, STF code and the LDPC-STFC used in the MIMO-WiMAX platform.

The extrinsic diversity product is given by [39]

$$\zeta_{ex} = |det(Q_0)|^{\frac{1}{2L}} \tag{3.30}$$

where Q_0 is defined as

$$Q_0 = W_0 \text{diag}(\delta_0^2, \delta_1^2, ..., \delta_{L-1}^2) W_0^{\mathcal{H}} \tag{3.31}$$

where $\sigma_l^2 = E[|h_{i,j}(l)|^2]$ with $h_{i,j}$ as defined in equation 3.13 and W_0 a $N \times L$ matrix as illustrated in [39] with $w = e^{j2\pi\Delta f}$ and τ_l the associated time delay for each path delay:

$$W_0 = \begin{bmatrix} 1 & 1 & \dots & 1 \\ w^{\tau_0} & w^{\tau_1} & \dots & w^{\tau_{L-1}} \\ \vdots & \vdots & \ddots & \vdots \\ w^{(N-1)\tau_0} & w^{(N-1)\tau_1} & \dots & w^{(N-1)\tau_{L-1}} \end{bmatrix}. \tag{3.32}$$

From equation 3.30 we can see that the extrinsic diversity product depends solely on the channel used. The SF codes for the WiMAX platform were simulated over various channel conditions, which include correlated channel conditions, where the impact of the diversity product on these codes is illustrated for the different types of channels.

3.3.2 Space-time codes for the MIMO-WiMAX platform

Combining space-time coding with MIMO-OFDM for broadband wireless communication systems over frequency-selective fading channels was first proposed using ST trellis codes [51] for each subcarrier. With the large decoding complexity of ST trellis codes, methods were proposed in [52] which applied orthogonal ST block coding techniques described in section 3.2.1 directly to each subcarrier, regarding it as a virtual antenna. As with the flat fading channel, the diversity gain implementing these codes as illustrated in section 3.2.1 can only achieve a maximum diversity of $M_t M_r$. To exploit the diversity provided by the frequency-selective fading channel using OFDM, methods were proposed in [53] which repeat the scheme in [52] over L consecutive carriers, reducing the rate of the code to $1/L$, but achieving a diversity order of $M_t M_r L$.

The codes used for the representation of space-time codes for the MIMO-WiMAX platform are based on the codes presented in [52]. The codes achieve a rate of one symbol per channel use, with a diversity order of $M_t M_r$. The code assumes quasi-static fading conditions, where the fading parameters remain constant over the whole codeword, which consists of two OFDM symbols, $M_b = 2$. The illustration of the space-time code for the MIMO-WiMAX platform implemented using a 2×2 antenna setup can be illustrated using equation 3.14 for a specific user as

$$\mathbf{G} = \left[\begin{array}{cc} \mathbf{C}_1 & \mathbf{C}_2 \end{array} \right] = \left[\begin{array}{cc} \mathbf{c}_{1,1}\, \mathbf{c}_{1,2} & \mathbf{c}_{2,1}\, \mathbf{c}_{2,2} \end{array} \right] = \begin{pmatrix} S_1 & S_2 & -S_2^* & S_1^* \\ S_3 & S_4 & -S_4^* & S_3^* \\ \vdots & \vdots & \vdots & \vdots \\ S_{2N-1} & S_{2N} & -S_{2N}^* & S_{2N-1}^* \end{pmatrix} \tag{3.33}$$

where S is an information symbol consisting of PSK or QAM constellation and N the number of subcarriers available for the specific user.

After the encoding of the information data in equation 3.33, the data are transmitted over the channel and the received signal for each OFDM tone p, can be illustrated by the following equations by using equation 3.12:

At the first receive antenna we have:

$$y_1^1(p) = \frac{1}{\sqrt{M_t}} \left[H_{1,1}^1(p) c_{1,1}(p) + H_{1,2}^1(p) c_{1,2}(p) \right] + w_1^1(p), \qquad p = 0, ..., N-1 \tag{3.34}$$

$$y_2^1(p) = \frac{1}{\sqrt{M_t}} \left[H_{1,1}^2(p) c_{2,1}(p) + H_{1,2}^2(p) c_{2,2}(p) \right] + w_2^1(p), \qquad p = 0, ..., N-1. \tag{3.35}$$

At the second receive antenna we have:

$$y_1^2(p) = \frac{1}{\sqrt{M_t}} \left[H_{2,1}^1(p) c_{1,1}(p) + H_{2,2}^1(p) c_{1,2}(p) \right] + w_1^2(p), \qquad p = 0, ..., N-1 \tag{3.36}$$

$$y_2^2(p) = \frac{1}{\sqrt{M_t}} \left[H_{2,1}^2(p) c_{2,1}(p) + H_{2,2}^2(p) c_{2,2}(p) \right] + w_2^2(p), \qquad p = 0, ..., N-1. \tag{3.37}$$

In the above equations, $n = 1..M_b$ and $M_b = 2$. Using equation 3.33 and knowing that $H_{i,j}^1 = H_{i,j}^2$ in quasi-static fading conditions for every transmit antenna j and receive antenna i, we can rewrite the above equations for $p = 0$ as follows:

For the first receive antenna:

$$y_1^1(0) = H_{1,1}(0)S_1 + H_{1,2}(0)S_2 + w_1^1(0) \tag{3.38}$$

$$y_2^1(0) = -H_{1,1}(0)S_2^* + H_{1,2}(0)S_1^* + w_2^1(0). \tag{3.39}$$

For the second receive antenna:

$$y_1^2(0) = H_{2,1}(0)S_1 + H_{2,2}(0)S_2 + w_1^2(0) \tag{3.40}$$

$$y_2^2(0) = -H_{2,1}(0)S_2^* + H_{2,2}(0)S_1^* + w_2^2(0). \tag{3.41}$$

The term $\frac{1}{\sqrt{M_t}}$ in the above equations was neglected for notational brevity. The hard-output decoding is illustrated as follows for $p = 0$ where the same procedure was used for all received symbols for $p = 0...N-1$.

To extract the symbols S_1 and S_2 from the above received signals, signal-processing techniques for orthogonal signals were used to separate the symbols as follows:

$$\tilde{S}_1 = \sum_{i=1}^{M_r} \left[H_{i,1}^*(0)y_1^i(0) + H_{i,2}(0)(y_2^i(0))^* \right] \tag{3.42}$$

$$\tilde{S}_2 = \sum_{i=1}^{M_r} \left[H_{i,2}^*(0)y_1^i(0) - H_{i,1}(0)(y_2^i(0))^* \right]. \tag{3.43}$$

The above equations can be simplified to:

$$\tilde{S}_1 = \sum_{i=1}^{M_r} \left[\left(|H_{i,1}(0)|^2 + |H_{i,1}(0)|^2 \right) S_1 + H_{i,1}^*(0)w_1^i + H_{i,2}(0)(w_2^i(0))^* \right] \tag{3.44}$$

$$\tilde{S}_2 = \sum_{i=1}^{M_r} \left[\left(|H_{i,1}(0)|^2 + |H_{i,1}(0)|^2 \right) S_2 + H_{i,2}^*(0)w_1^i - H_{i,1}(0)(w_2^i(0))^* \right]. \tag{3.45}$$

Equation 3.44 and equation 3.45 illustrate that the symbols S_1 and S_2 are separated from the received signals. The combined signals $\tilde{S}_1$ and $\tilde{S}_2$ are passed to a maximum likelihood detector, which based decisions on the Euclidean distances between the combined signals $\tilde{S}_1$ and $\tilde{S}_2$ and all possible transmitted symbols. The signals with the smallest Euclidean distances are chosen as the maximum likelihood transmitted symbols for $\tilde{S}_1$ and $\tilde{S}_2$ respectively.

To separate the signals with no ISI, it is imperative that the channel remains quasi-static for the whole codeword. If the codes were to be used in block-fading conditions ($H^1_{i,j} \neq H^2_{i,j}$), equation 3.42 for S_1 can be rewritten as

$$\tilde{S}_1 = \sum_{i=1}^{M_r} \left[(H^1_{i,1})^*(0) y^i_1(0) + H^2_{i,2}(0)(y^i_2(0))^* \right] \tag{3.46}$$

and simplified to

$$\begin{aligned} \tilde{S}_1 = &\left(|H^1_{1,1}(0)|^2 + |H^2_{1,2}(0)|^2 + |H^1_{2,1}(0)|^2 + |H^2_{2,2}(0)|^2 \right) S_1 + \\ &\left((H^1_{1,1}(0))^* H^1_{1,2}(0) - (H^2_{1,1}(0))^* H^2_{1,2}(0) + (H^1_{2,1}(0))^* H^1_{2,2}(0) - (H^2_{2,1}(0))^* H^2_{2,2}(0) \right) S_2 + \\ &(H^1_{1,1}(0))^* w^1_1(0) + H^2_{1,2}(0)(w^1_2(0))^* + (H^1_{2,1}(0))^* w^2_1(0) + H^2_{2,2}(0)(w^2_2(0))^*. \end{aligned} \tag{3.47}$$

We can clearly see from equation 3.47 that S_2 does not cancel in non-quasi-static fading conditions. The ISI introduced by the block-fading conditions will dramatically decrease system performance as single symbol ML detection will not be viable, as $\tilde{S}_1$ is now a function of S_1 and S_2.

Further improvements on the performance of the ST code on the MIMO-WiMAX platform were made by concatenating the code with an LDPC code. The LDPC code was used as the outer code, where soft outputs were formed directly from the space-time decoder. In order to produce soft outputs with the space-time code, methods proposed in [54] and [55] were used to develop a soft-output space-time decoder for the MIMO-WiMAX platform.

The soft-output decoder is a symbol-by-symbol maximum a posteriori probability (MAP) decoder, derived from methods proposed in [55] for flat fading conditions. Applying Bayes' rule, the a posteriori probability of the ST code consisting of k symbols per OFDM tone ($p = 0, ..., N-1$) over M_b consecutive quasi-static OFDM blocks with M_r receive antennas and M_t transmit antennas can be expressed as

$$P(S_{1+pk}, .., S_{k+pk}|y_1^1(p), ..., y_{M_b}^{M_r}(p)) = P(y_1^1(p), ..., y_{M_b}^{M_r}(p)|S_{1+pk}, .., S_{k+pk}).P(S_{1+pk}, .., S_{k+pk}) \tag{3.48}$$

where $P(S_{1+pk}, .., S_{k+pk})$ denotes the a priori probability of the transmitted symbol used with tone p. Furthermore, from equation 3.48

$$P(y_1^1(p), ..., y_{M_b}^{M_r}(p)|S_{1+pk}, .., S_{k+pk}) = \frac{1}{(\sigma\sqrt{2\pi})^{M_r M_b}} \exp\left[-\frac{1}{2\sigma^2}\sum_{l=1}^{M_r}\sum_{i=1}^{M_b}\left|y_i^l(p) - \sum_{j=1}^{M_t} H_{l,j}^i(p)c_{i,j}(p)\right|^2\right] \tag{3.49}$$

where $p = 0, ..., N-1$ and $\sigma^2 = \frac{N_0}{2}$ are the noise variance at each receiving antenna, which is scaled appropriately according to a specific E_b/N_0 value used in the simulation. The term $\frac{1}{\sqrt{M_t}}$ is neglected for notational brevity.

For the space-time code presented in equation 3.33 for the MIMO-WiMAX platform, equation 3.48 can be presented as

$$\begin{aligned} &P(S_{1+pk}, .., S_{k+pk}|y_1^1(p), ..., y_{M_b}^{M_r}(p)) \\ &= C \,.\, \exp\left\{-\frac{1}{2\sigma^2}\sum_{l=1}^{M_r}\left[\left|y_1^l(p) - \sum_{j=1}^{M_t} H_{l,j}^1(p)c_{1,j}(p)\right|^2 + \left|y_2^l(p) - \sum_{j=1}^{M_t} H_{l,j}^2(p)c_{2,j}(p)\right|^2\right]\right\} \end{aligned} \tag{3.50}$$

for $p = 0, ..., N-1$, where C consists of all constants not dependent on $S_{1+pk}, .., S_{k+pk}$. The equation can be simplified further, knowing that the ST code in equation 3.33 is defined for $M_t = 2$ and quasi-static conditions, $H_{l,j}^1 = H_{l,j}^2$. Due to the fact that the decoding procedure will remain the same for all tones, an example of decoding for $p = 0$ using equation 3.50 can be illustrated as follows:

$$P(S_1, S_2|y_1^1(0), ..., y_2^{M_r}(0))$$
$$= C \cdot \exp\left\{ -\frac{1}{2\sigma^2} \sum_{l=1}^{M_r} \left[\left| y_1^l(0) - H_{l,1}(0)S_1 - H_{l,2}(0)S_2 \right|^2 + \left| y_2^l(0) + H_{l,1}(0)S_2^* - H_{l,2}(0)S_1^* \right|^2 \right] \right\}. \quad (3.51)$$

From the orthogonality of the code, we can expand equation 3.51 into two parts,

$$P(S_1|y_1^1(0), ..., y_2^{M_r}(0))$$
$$= C \cdot \exp\left\{ -\frac{1}{2\sigma^2} \sum_{l=1}^{M_r} \left[-H_{l,1}(0)S_1(y_1^l(0))^* - H_{l,1}^*(0)S_1^* y_1^l(0) - \right.\right.$$
$$\left.\left. H_{l,2}(0)S_1^*(y_2^l(0))^* - H_{l,2}^*(0)S_1 y_2^l(0) + |S_1|^2 \sum_{i=1}^{2} |H_{l,i}(0)|^2 \right] \right\} \quad (3.52)$$

where equation 3.52 is only dependent on S_1 and equation 3.53 only on S_2.

$$P(S_2|y_1^1(0), ..., y_2^{M_r}(0))$$
$$= C \cdot \exp\left\{ -\frac{1}{2\sigma^2} \sum_{l=1}^{M_r} \left[-H_{l,2}(0)S_2(y_1^l(0))^* - H_{l,2}^*(0)S_2^* y_1^l(0) + \right.\right.$$
$$\left.\left. H_{l,1}(0)S_2^*(y_2^l(0))^* - H_{l,1}^*(0)S_2 y_2^l(0) + |S_2|^2 \sum_{i=1}^{2} |H_{l,i}(0)|^2 \right] \right\} \quad (3.53)$$

These equations can be further simplified to a similar form presented in [54] as follows:

$$P(S_1|y_1^1(0), ..., y_2^{M_r}(0))$$
$$= C \cdot \exp\left\{ -\frac{1}{2\sigma^2} \left[\left| \left[\sum_{l=1}^{M_r} (H_{l,1}^*(0)y_1^l(0) + H_{l,2}(0)(y_2^l(0))^*) \right] - S_1 \right|^2 + \left(-1 + \sum_{l=1}^{M_r} \sum_{i=1}^{2} |H_{l,i}(0)|^2 \right) |S_1|^2 \right] \right\} \quad (3.54)$$

$$P(S_2|y_1^1(0), ..., y_2^{M_r}(0))$$
$$= C \cdot \exp\left\{ -\frac{1}{2\sigma^2} \left[\left| \left[\sum_{l=1}^{M_r} (H_{l,2}^*(0)y_1^l(0) - H_{l,1}(0)(y_2^l(0))^*) \right] - S_2 \right|^2 + \left(-1 + \sum_{l=1}^{M_r} \sum_{i=1}^{2} |H_{l,i}(0)|^2 \right) |S_2|^2 \right] \right\}. \quad (3.55)$$

In the above equations, C is updated on each simplification by incorporating all constants which do not depend on S_1 and S_2. C also serves as a normalization factor to ensure that $\sum P(S_1|y_1^1(0),...,y_2^{M_r}(0)) = 1$ and $\sum P(S_2|y_1^1(0),...,y_2^{M_r}(0)) = 1$, where the summation is over all possible symbols for the given constellation used. For the concatenation with the LDPC code, the above probabilities are expressed in a log-likelihood ratio, by first deriving the bit probability of each bit, being a 1 and 0, and computing it as $\lambda_L = \ln\frac{P(x_k=1|\mathbf{Y})}{P(x_k=-1|\mathbf{Y})}$, where (x_k, x_{k+1}) is mapped to a symbol S_l in equation 3.48-3.55 and $\mathbf{Y}$ is the codeword received.

3.3.3 Space-frequency codes for the MIMO-WiMAX platform

Coding across OFDM tones and antennas in a MIMO-OFDM system is known as SF codes. The simplest method of constructing an SF code is to spread the Alamouti scheme presented in 3.2.1 over two OFDM tones [56]. This method can only achieve space diversity gain, where the maximum diversity available in frequency-selective fading channels is $M_t M_r L$. Methods were proposed in [50], for a systematic design of full diversity SF codes, by repeating the codes presented in [56] on L different OFDM tones. Although it achieves full diversity, the maximum achievable data rate is $\frac{1}{L}$ symbols per channel use. A few methods on the design of SF codes that can guarantee full diversity and a rate of one symbol per channel use were presented in [39], [57], [58]. The rate-1 SF code used for analysis on the MIMO-WiMAX platform is designed using the code presented in [39], which generalizes a code construction method for an arbitrary number of transmit antennas and power delay profiles. The construction of the code is presented in the following subsection.

3.3.3.1 Rate-1 space-frequency code

From [39], equation 3.14 is represented as

$$\mathbf{G} = \begin{bmatrix} \mathbf{B}_1^{\mathcal{T}} & \mathbf{B}_2^{\mathcal{T}} & \dots & \mathbf{B}_J^{\mathcal{T}} & \mathbf{0}_{N-JK}^{\mathcal{T}} \end{bmatrix}^{\mathcal{T}} \tag{3.56}$$

where $K = M_t L$, $J = \frac{N}{K}$ and each block $\mathbf{B_i}$ for $1 \leq i \leq J$ is of size $K \times M_t$. The $\mathbf{0}_{N-JK}^{\mathcal{T}}$ term in the above equation represents an all zero matrix, which is padded if the number of subcarriers is not a multiple of K. The structure B_i can be represented in the form illustrated in [6] as

$$\mathbf{B}_i = \sqrt{M_t} \begin{pmatrix} \tilde{\mathbf{X}}_{i,1} & & & \\ & \tilde{\mathbf{X}}_{i,2} & & \\ & & \ddots & \\ & & & \tilde{\mathbf{X}}_{i,M_t} \end{pmatrix} \tag{3.57}$$

where $\tilde{\mathbf{X}}_{i,j} = [\, X_{(i-1)K+(j-1)L+1} \;\; X_{(i-1)K+(j-1)L+2} \;\; \ldots \;\; X_{(i-1)K+(j)L}]$, $i = 1, 2, ..., J$ and $j = 1, 2, ..., M_t$. The entries for $\tilde{\mathbf{X}}_{i,j}$ are given as

$$[\, \tilde{\mathbf{X}}_{i,1}^{\mathcal{T}} \;\; \tilde{\mathbf{X}}_{i,2}^{\mathcal{T}} \;\; ... \;\; \tilde{\mathbf{X}}_{i,M_t}^{\mathcal{T}}] = [\, X_{(i-1)K+1} \;\; X_{(i-1)K+2} \;\; ... \;\; X_{(i)K} \,] = \mathbf{\Theta_K S}_i \tag{3.58}$$

for $i = 1, 2, ..., J$. The information vector $\mathbf{S}_i$ is of PSK or QAM constellation and is given as $\mathbf{S}_i = [\, S_{(i-1)K+1} \;\; S_{(i-1)K+2} \;\; ... \;\; S_{(i)K}]$. $\mathbf{\Theta_K}$ is a precoder matrix based on algebraic rotation, which is discussed in section 3.4. An example of the code for $\mathbf{B}_i$ for $i = 1$, $M_t = 2$, $M_r = 2$ and designing the code to obtain a maximum frequency diversity of $L = 2$ is given as

$$\mathbf{B}_1 = \sqrt{2} \begin{pmatrix} X_1 & 0 \\ X_2 & 0 \\ 0 & X_3 \\ 0 & X_4 \end{pmatrix} \tag{3.59}$$

where $[X_1 \; X_2 \; X_3 \; X_4]^{\mathcal{T}} = \mathbf{\Theta_4}[S_1 \; S_2 \; S_3 \; S_4]^{\mathcal{T}}$. The code used in the example is used for the analysis of rate-1 SF codes on the MIMO-WiMAX platform for the 2×2 antenna setup.

3.3.3.2 High-rate space-frequency code

The SF codes in the previous section can only achieve a maximum rate of one symbol per channel use. In [7], a rate-M_t SF code was proposed which achieves full diversity for any number of transmit antennas and arbitrary channel power delay profiles. The codes are constructed by using a layering concept, which was introduced by the TAST codes (section 3.2.3). As with the TAST codes, the Diophantine approximation theory [47] is used to make threads "transparent" to one another. Using the same structure as with equation 3.56, an example for the code used on the MIMO-WiMAX platform for $M_t = 2$, $M_r = 2$ and $L = 2$ is given as [6]

$$\mathbf{B}_i = \begin{pmatrix} X_{8i-7} & \phi X_{8i-3} \\ X_{8i-6} & \phi X_{8i-2} \\ \phi X_{8i-1} & X_{8i-5} \\ \phi X_{8i} & X_{8i-4} \end{pmatrix} \tag{3.60}$$

where the entries are formed as $[\, X_{8i-7}\ X_{8i-6}\ X_{8i-5}\ X_{8i-4}\,]^{\mathcal{T}} = \mathbf{\Theta_4}[\, S_{8i-7}\ S_{8i-6}\ S_{8i-5}\ S_{8i-4}\,]^{\mathcal{T}}$ and $[\, X_{8i-3}\ X_{8i-2}\ X_{8i-1}\ X_{8i}\,]^{\mathcal{T}} = \mathbf{\Theta_4}[\, S_{8i-3}\ S_{8i-2}\ S_{8i-1}\ S_{8i}\,]^{\mathcal{T}}$.

With the codes illustrated in this section, a joint decoding method is required to decode the above-mentioned SF codes, as the symbols are entangled with a precoder matrix based on algebraic rotation. An exhaustive search over all possible combinations of symbols for joint detection is unfeasible, whereas sphere decoding methods can be applied to alleviate decoding complexity. Sphere decoding is an approximate ML decoding scheme and is discussed in detail in chapter 4. Systematic code design of high-rate SF codes for any M_t, M_b and L is given in [7].

For decoding, the codewords received have to be constructed in an appropriate form to be able to apply the sphere-decoding algorithm. The decoding procedure will consist of J sphere decoders for $\mathbf{B}_i$, $i = 1, 2, ..., J$, where the decoding procedure is the same for all $i = 1, 2, ..., J$. An example of the decoding of $\mathbf{B}_1$ for the code in equation 3.60 is as follows:

For $M_t = 2$, $M_r = 2$, $L = 2$, $K = M_t L = 4$ and $M_b = 1$, the high rate full diversity code for $\mathbf{B}_1$ is represented as

$$\mathbf{B}_1 = [\, \mathbf{c}_{1,1,1}\ \ \mathbf{c}_{1,2,1}\,] = \begin{pmatrix} X_1(1) & \phi X_2(1) \\ \phi X_2(2) & X_1(2) \\ X_1(3) & \phi X_2(3) \\ \phi X_2(4) & X_1(4) \end{pmatrix} \tag{3.61}$$

where $[X_n(1) \ldots X_n(4)]^{\mathcal{T}} = \mathbf{\Theta_4}[S_{4(n-1)+1} \ldots S_{4n}]^{\mathcal{T}}$, $n = 1, 2$. Equation 3.20 can be divided into a series of decoding blocks for $M_b = 1$ as

$$\begin{pmatrix} \mathbf{Y}_{1,i} \\ \mathbf{Y}_{2,i} \end{pmatrix} = \underbrace{\begin{pmatrix} \mathbf{\Lambda}^1_{1,1,i} & \mathbf{\Lambda}^1_{1,2,i} \\ \mathbf{\Lambda}^1_{2,1,i} & \mathbf{\Lambda}^1_{2,2,i} \end{pmatrix}}_{\mathbf{H}_{1,i}} \begin{pmatrix} \mathbf{c}_{1,1,i} \\ \mathbf{c}_{1,2,i} \end{pmatrix}, \quad i = 1, 2, ..., J \tag{3.62}$$

where the noise term and scaling factor are neglected for notational brevity. $\mathbf{\Lambda}^{u}_{l,j,i} = \mathrm{diag}(H^{u}_{l,j,i}((i-1)K), ..., H^{u}_{l,j,i}(iK-1))$ denotes the diagonal form of the channel vector for the u^{th} received OFDM symbol and i^{th} decoding block between the j^{th} transmit antenna and the l^{th} receive antenna in frequency domain. For $i = 1$, the above simplifies to

$$\begin{pmatrix} \mathbf{Y}_{1,1} \\ \mathbf{Y}_{2,1} \end{pmatrix} = \tilde{\mathbf{G}}_{\mathbf{1}} \begin{pmatrix} X_1(1) \\ X_1(2) \\ X_1(3) \\ X_1(4) \\ \phi X_2(1) \\ \phi X_2(2) \\ \phi X_2(3) \\ \phi X_2(4) \end{pmatrix} = \underbrace{\tilde{\mathbf{G}}_{\mathbf{1}} \begin{pmatrix} \mathbf{\Theta_4} & \\ & \phi\mathbf{\Theta_4} \end{pmatrix}}_{\tilde{\mathbf{H}}} \underbrace{\begin{pmatrix} S_1 \\ S_2 \\ S_3 \\ \vdots \\ S_8 \end{pmatrix}}_{\mathbf{S}} \tag{3.63}$$

where $\tilde{\mathbf{G}}_1$ represents the reordering of the columns of $\mathbf{H}_{1,1}$ with column index $\{1,\ 6,\ 3,\ 8,\ 5,\ 2,\ 7,\ 4\}$. $\mathbf{\Theta_4}$ represents the precoder matrix based on algebraic rotation, and ϕ the phase rotation based on Diophantine approximation to make the layers transparent from each other. With the code in the form $\mathbf{Y} = \tilde{\mathbf{H}}.\mathbf{S}$, sphere decoding techniques (chapter 4) were employed to decode the symbols $\mathbf{S} = [S_1, S_2, ..., S_8]^{\mathcal{T}}$ which are of PSK or QAM constellation.

3.3.4 Space-time-frequency codes for the MIMO-WiMAX platform

In practice wireless channels are subject to block-fading conditions. Coding strategies defined in the previous sections were either derived for quasi-static fading conditions or usable in block-fading channels without taking advantage of the extra dimension of diversity. Appropriate coding schemes across multiple independent fading OFDM blocks can increase diversity in the channel for block-fading channels [59], [60]. STF coding techniques offer maximum achievable diversity and were shown in [61] to be the product of space, frequency and time diversity due to block fades $(M_t M_r M_b L)$.

STFC designs proposed in [7] guarantee rate-M_t and full diversity over MIMO frequency-selective block-fading channels. The codes proposed in [7] form the basis of the analysis of STFC on the MIMO-WiMAX platform and were used for the proposed

concatenation scheme of STFC-LDPC in section 3.5. As with the high-rate SF codes in section 3.3.3.2, the codes are constructed by using a layering concept and Diophantine approximation to make threads transparent to one other.

The STFC codes for the MIMO-WiMAX platform are described for N OFDM tones, M_t transmit antennas, M_r receive antennas, M_b OFDM blocks and a frequency diversity order of L. Let $N_L = 2^{\log_2 L}$, $N_q = 2^{\log_2 M_t}$, $K = N_L N_q$ and $J = \frac{N}{K}$; the codes can then be presented in the form

$$\mathbf{G} = \left[\begin{array}{cccc} \mathbf{B}_1^{\mathcal{T}} & \mathbf{B}_2^{\mathcal{T}} & \dots & \mathbf{B}_J^{\mathcal{T}} \end{array} \right]^{\mathcal{T}} \tag{3.64}$$

where $\mathbf{B}_i,\ \ i = 1, 2, ..., J$ is a $K \times M_t M_b$ matrix using the same coding strategy for every subblock. An encoding example for $\mathbf{B}_1$ using $M_t = 2$, $M_b = 2$ and $L = 2$ is as follows:

$$\mathbf{B}_1 = \left[\begin{array}{cccc} \mathbf{c}_{1,1,1} & \mathbf{c}_{1,2,1} & \mathbf{c}_{2,1,1} & \mathbf{c}_{2,2,1} \end{array} \right] = \begin{pmatrix} X_1(1) & \phi X_2(1) & X_1(1) & \phi X_2(1) \\ \phi X_2(2) & X_1(2) & \phi X_2(2) & X_1(2) \\ X_1(3) & \phi X_2(3) & X_1(3) & \phi X_2(3) \\ \phi X_2(4) & X_1(4) & \phi X_2(4) & X_1(4) \end{pmatrix} \tag{3.65}$$

$[X_n(1) \dots X_n(4)]^{\mathcal{T}} = \mathbf{\Theta_4} [S_{4(n-1)+1} \dots S_{4n}]^{\mathcal{T}}, n = 1, 2.$ $\mathbf{\Theta_4}$ represents the unitary precoder matrix based on algebraic rotation, and ϕ the phase rotation based on Diophantine approximation to make the layers transparent from each other. The code presented is a rate-1 STFC; designs for rate-M_t STFC are presented in [7].

For decoding, the codewords received have to be constructed in an appropriate form to be able to apply sphere decoding techniques. The decoding procedure will consist of J sphere decoders for $\mathbf{B}_i,\ \ i = 1, 2, ..., J$, where the decoding procedure is the same for all $i = 1, 2, ..., J$. Using the STFC from equation 3.65, a decoding example for $\mathbf{B}_1$ is illustrated as follows:

Equation 3.20 can be divided into a series of decoding blocks for $M_b = 2$ as

$$\begin{pmatrix} \mathbf{Y}_{1,i} \\ \mathbf{Y}_{2,i} \end{pmatrix} = \underbrace{\begin{pmatrix} \mathbf{\Lambda}^1_{1,1,i} & \mathbf{\Lambda}^1_{1,2,i} & & \\ \mathbf{\Lambda}^1_{2,1,i} & \mathbf{\Lambda}^1_{2,2,i} & & \\ & & \mathbf{\Lambda}^2_{1,1,i} & \mathbf{\Lambda}^2_{1,2,i} \\ & & \mathbf{\Lambda}^2_{2,1,i} & \mathbf{\Lambda}^2_{2,2,i} \end{pmatrix}}_{\mathbf{H}_i} \begin{pmatrix} \mathbf{c}_{1,1,i} \\ \mathbf{c}_{1,2,i} \\ \mathbf{c}_{2,1,i} \\ \mathbf{c}_{2,2,i} \end{pmatrix}, \quad i = 1, 2, ..., J \tag{3.66}$$

where the noise term and scaling factor are neglected for notational brevity. $\mathbf{\Lambda}^u_{l,j,i} = \text{diag}(H^u_{l,j,i}((i-1)K), ..., H^u_{l,j,i}(iK-1))$ denotes the diagonal form of the channel vector for the u^{th} received OFDM symbol ($u = 1, .., M_b$) and i^{th} decoding block between the j^{th} transmit antenna and the l^{th} receive antenna in frequency domain. For $i = 1$, the above simplifies to

$$\begin{pmatrix} \mathbf{Y}_{1,1} \\ \mathbf{Y}_{2,1} \end{pmatrix} = \underbrace{\tilde{\mathbf{G}}_1 \begin{pmatrix} \mathbf{\Theta_4} & & \\ & \phi\mathbf{\Theta_4} & \\ \mathbf{\Theta_4} & & \\ & & \phi\mathbf{\Theta_4} \end{pmatrix}}_{\tilde{\mathbf{H}}} \underbrace{\begin{pmatrix} S_1 \\ S_2 \\ S_3 \\ \vdots \\ S_8 \end{pmatrix}}_{\mathbf{S}} \tag{3.67}$$

where $\tilde{\mathbf{G}}_1$ represents the reordering of the columns of $\mathbf{H}_1$ with column index $\{1,\ 6,\ 3,\ 8,\ 5,\ 2,\ 7,\ 4,\ 9,\ 14,\ 11,\ 16,\ 13,\ 10,\ 15,\ 12\}$. $\mathbf{\Theta_4}$ represents the precoder matrix based on algebraic rotation, and ϕ the phase rotation based on Diophantine approximation to make the layers transparent to each other. With the code in the form $\mathbf{Y} = \tilde{\mathbf{H}}.\mathbf{S}$, sphere decoding techniques (chapter 4) were employed to decode the symbols $\mathbf{S} = [S_1, S_2, ..., S_8]^{\mathcal{T}}$, which are of PSK or QAM constellation. Equivalent representations can be presented in a form similar to the above for any rate STFC and can also be used directly for soft-output decoding with the sphere decoder (chapter 4).

3.4 ALGEBRAIC ROTATION MATRICES

Lattice codes based on rotated constellations of QAM symbols were first investigated by Belfiore and showed a performance gain in terms of signal diversity for flat fading channels [62], [63]. It was found in [64] that Vandermonde matrices can be used to implement

these lattice codes to enable coding gain and diversity through multi-path propagation SISO channels. The Vandermonde matrices were used as the linear precoder matrices, where the entries are drawn from the complex field and the size used depends on various factors, which include the multi-path diversity order, number of transmit antennas and independent fading blocks in the system.

For MIMO flat fading channels, the precoder matrices were used in [40], [46] to obtain full diversity at a rate of 1. High-rate full diversity schemes for MIMO flat fading channels were presented in [65] and for frequency-selective fading MIMO channels in [66]. The SF and STF codes used in this dissertation use these precoder matrices to obtain full diversity, whereas the codes presented in [7] can obtain high-rate, full diversity for any number of transmit antennas and OFDM tones in block fading conditions.

3.4.1 Designing precoder matrices

The linear precoder matrix $\mathbf{\Theta}_K$ is a $K \times K$ matrix designed according to a total dimension of K. For the codes used in this dissertation $K = 2^{\log_2 \tilde{\mathrm{N}}}$, where $\tilde{N} = N_L M_t M_b$ and $N_L = 2^{\log_2 \mathrm{L}}$. Although the rate-1 STFC is defined for $M_b = 2$, the code implemented is an extension of the rate-2 SFC, repeated over two independent fading blocks, where the rotations are done as with the rate-2 SFC, which is defined for $M_b = 1$. The rate-M_t STFC is designed directly for a dimension K, with $M_b = 2$.

For the design of the precoder matrix $\mathbf{\Theta}_K$, the following two criteria have to be satisfied:

- For maximum diversity, the $K \times K$ matrix $\mathbf{\Theta}_K$ should be designed so that:

$$|\theta_i^{\mathcal{T}}(\mathbf{s} - \tilde{\mathbf{s}})| \neq 0, \quad i \in [1, K], \quad \mathbf{s} \neq \tilde{\mathbf{s}}. \tag{3.68}$$

- For maximum coding gain, the $K \times K$ matrix $\mathbf{\Theta}_K$ should be designed to maximize the minimum product distance:

$$d_{min}^2 = \min_{\mathbf{s} \neq \tilde{\mathbf{s}}} \prod_{i=1}^{K} |\theta_i^{\mathcal{T}}(\mathbf{s} - \tilde{\mathbf{s}})|. \tag{3.69}$$

In the above two equations, $\mathbf{s}$ and $\tilde{\mathbf{s}}$ represent $K \times 1$ information symbol vectors and $\theta_i^{\mathcal{T}}$

denotes the i^{th} row of precoder matrix $\mathbf{\Theta}_K$.

The two methods that can be used to construct the linear precoding matrices are known as construction based on parameterization and construction based on algebraic tools. For parameterization, the code construction procedure is based on an exhaustive search to maximize equation 3.69. This search is not feasible when parameter K is large.

Algebraic construction methods were proposed in [67] ,which yield precoders with large coding gain for any K. The first design approach proposed in [67] yield unitary precoding matrices when K is a power of 2. Unitary matrices have the advantage over non-unitary matrices that they correspond to a rotation and preserve the Euclidian distance among the K-dimensional signal points, $\mathbf{s}$. Non-unitary matrices have some constellation points closer and some further, which degrades performance in near AWGN channels.

The design of the precoder matrix as presented in [67] is given as

$$\mathbf{\Theta}_K = \frac{1}{\lambda}\begin{bmatrix} 1 & \alpha_1 & \dots & \alpha_1^{K-1} \\ 1 & \alpha_2 & \dots & \alpha_2^{K-1} \\ \vdots & \vdots & & \vdots \\ 1 & \alpha_K & \dots & \alpha_K^{K-1} \end{bmatrix} \tag{3.70}$$

where λ is the power normalization factor and $\{\alpha_k\}_1^K$ are the roots of the minimum polynomial α, where design examples for various values of K are given in table 3.1.

TABLE 3.1: Design examples of Θ_K for various dimension values of K

K	α_1	α_2	α_3	α_4	α_5	α_6
2	$e^{-j\frac{\pi}{4}}$	$e^{-j\frac{5\pi}{4}}$				
4	$e^{-j\frac{\pi}{8}}$	$e^{-j\frac{5\pi}{8}}$	$e^{-j\frac{9\pi}{8}}$	$e^{-j\frac{13\pi}{8}}$		
6	$e^{-j\frac{2\pi}{7}}$	$e^{-j\frac{4\pi}{7}}$	$e^{-j\frac{6\pi}{7}}$	$e^{-j\frac{8\pi}{7}}$	$e^{-j\frac{10\pi}{7}}$	$e^{-j\frac{12\pi}{7}}$

The second design method proposed yields unitary precoder matrices for any dimension K and is presented as

$$\mathbf{\Theta}_K = \mathbf{F}_{\tilde{M}}^{\mathcal{H}} \mathrm{diag}(1 \;\; \varphi \;\; \dots \;\; \varphi^{\tilde{M}-1}) \tag{3.71}$$

where $\tilde{M} = 2^{\log_2 \tilde{N}}$ with $\tilde{N} = N_L M_t M_b$, $\varphi = \exp(\mathrm{j}2\pi/4\tilde{M})$, $\phi = \varphi^{1/N_q}$ and $\mathbf{F}_{\tilde{M}}^{\mathcal{H}}$ is a $\tilde{M} \times \tilde{M}$ discrete Fourier transform matrix. Design choices for α are discussed in [7] and [67]. This method was used to construct the algebraic rotation matrices used with the rate-1 SF, rate-2 SF and STFC in all simulations.

3.5 STFC-LDPC CONCATENATED SCHEME

The multi-antenna codes can achieve high diversity gain, but only limited coding gain. The codes are designed according to the rank criteria to obtain a maximum diversity code $\mathbf{C}$. However, the product criterion is neglected and the minimum determinant of $\mathbf{C}$ is found to vanish with an increase in constellation size [68], limiting the coding gain to the maximum value of this determinant. For coding gain improvements, STC-LDPC and STFC-LDPC concatenated coding schemes are proposed in this dissertation. LDPC codes were first proposed by Gallager in 1962 [69] and recently rediscovered by MacKay and Neal [70] and are recognized as good error-correcting codes achieving near channel capacity.

The LDPC code has a very sparse parity-check matrix $\mathcal{H}$, which has the effect of reducing the dependencies for each element in the syndrome calculations and leads to extremely good BER performance. The LDPC code is expressed in terms of a factor graph known as a Tanner graph [71], using variable nodes which correspond to each element of the codeword and check nodes which correspond to the parity checks of the parity-check matrix $\mathcal{H}$. Each variable node and check node has a degree associated with it which corresponds to the number of edges that emanate from the variable or check nodes. If a graph has Λ_i variable nodes of degree i and P_j check nodes of degree j, the following notation is used to describe the variable node degree distribution as [72]

$$\Lambda(x) = \sum_{i=1}^{l_{max}} \Lambda_i x^i \tag{3.72}$$

and for the check node degree distribution as [72]

$$P(x) = \sum_{j=1}^{r_{max}} P_j x^j. \tag{3.73}$$

For asymptotic analysis, the Tanner graph can also be presented from an edge perspective, rather than a node perspective as [72]

$$\lambda(x) = \sum_{i=1}^{l_{max}} \lambda_i x^i = \frac{\Lambda'(x)}{\Lambda'(1)} \tag{3.74}$$

and [72]

$$\rho(x) = \sum_{j=1}^{r_{max}} \rho_j x^j = \frac{P'(x)}{P'(1)} \tag{3.75}$$

where $\lambda(x)$ denotes the variable edge degree distribution and $\rho(x)$ the check edge degree distribution of the Tanner graph. The decoding algorithm for the LDPC code using the structure defined by the Tanner graph is known as the Pearl Belief propagation algorithm [73]. The algorithm is a message-passing algorithm, passing probabilities between variable and check nodes and is discussed in section 3.5.2.

Various methods are used in the design of irregular LDPC codes, which include the optimization technique, called density evolution. LDPC codes are usually optimized assuming a very long length code, which introduces large delays at the encoder/decoder of the codewords. Long length codes are unsuitable for time-sensitive applications. For this reason only short-length LDPC codes were evaluated in this dissertation. The following sub-section describes the design of the LDPC used based on density evolution.

3.5.1 Density evolution design

The optimizing of the LDPC code for the high-performance MIMO system using the STFC or the STC scheme required the PDF of the received log-likelihood values [74]. The PDF of the received log-likelihood values for the STFC using $E_b/N_0 = 4dB$ is illustrated in figure 3.1.

From this figure, it can be seen that the PDF of the received log-likelihood values can be approximated as Gaussian, as it follows the ideal Gaussian PDF on the distribution graph in figure 3.1 with only a small deviation. The initial density of the STFC can then be defined as

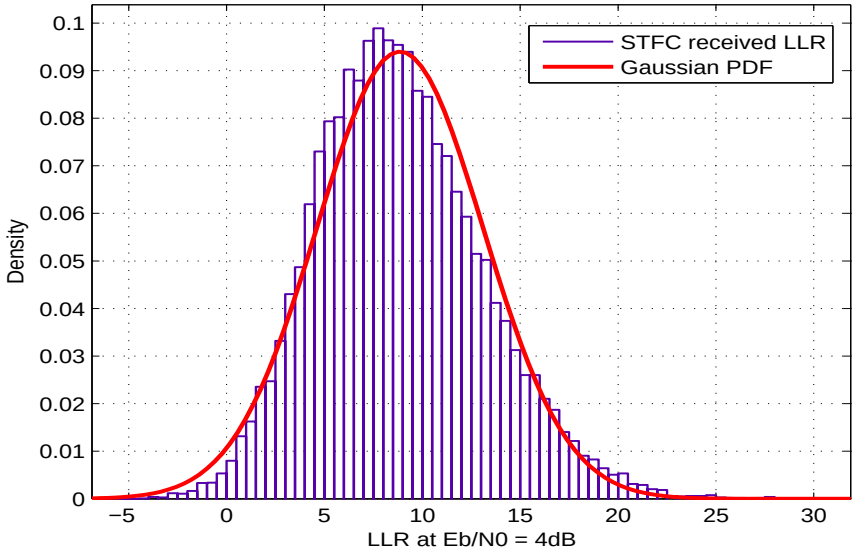

FIGURE 3.1: PDF of the received log-likelihood values for the STFC using $E_b/N_0 = 4dB$

$$a_0(\lambda_L(x_k)) = \frac{\sigma}{2\sqrt{2\pi}} e^{-(\lambda_L(x_k)-2/\sigma^2)^2/(8/\sigma^2)} \tag{3.76}$$

where $\lambda_L(x_k)$, $\lambda_L(x_k) \in (-\infty, \infty)$, denotes the log-likelihood value received at the input of the channel decoder [75]. The density evolution algorithm uses the initial density $a_0(\lambda_L(x_k))$ of the STFC scheme to calculate the noise threshold σ^* [76] that is defined as follows:

$$\sigma^*(\lambda(x), \rho(x)) = \sup\{\sigma \in [0, \infty] : \lim_{i\to\infty} P_e(\sigma) \to 0\}. \tag{3.77}$$

The noise threshold σ^* is the largest variance that the Belief propagation decoder can accommodate to yield an arbitrary small bit error probability using enough iterations i within the decoder. Rewriting the density as

$$a_i(\lambda_L(x_k)) = a_0(\lambda_L(x_k)) * \lambda(\rho(a_{i-1}(\lambda_L(x_k)))) \tag{3.78}$$

density evolution obtains the noise threshold σ^* by iteratively computing equation 3.78 till $i \to \infty$ (typically 1500) or when a preset bit error probability ε has been acquired. The bit error probability threshold is satisfied when

$$\int_{-\infty}^{0} a_i(z)dz \leq \varepsilon \tag{3.79}$$

where ε is typically set to values between 10^{-6} and 10^{-8}. When the noise level is lower than the noise threshold σ^* the recursive computation of equation 3.78 yields a desired density of

$$\lim_{i\to\infty} a_i(\lambda_L(x_k)) \approx \triangle_\infty. \tag{3.80}$$

Optimized degree distribution pairs $(\lambda(x), \rho(x))$ have been found in [76] for the initial density $a_0(\lambda_L(x_k)$ that is given in equation 3.76. The codeword length was limited by the MIMO-WiMAX platform and because of this finite analysis the degree distribution pair used was [76], $\lambda(x) = 0.38354x + 0.04237x^2 + 0.57409x^3$ and $\rho(x) = 0.24123x^4 + 0.75877x^5$.

Using the degree distribution, codes used for decoding were constructed using the Progressive Edge Growth algorithm [77]. The algorithm connects an edge between two nodes and then verifies if the minimum cycle length of the code is at least greater than the minimum set value.

3.5.2 Belief propagation

After obtaining the soft-output log-likelihood ratio (LLR) values from the soft-output sphere decoder (see section 4.4), the values are sent to the LDPC decoder, which uses Pearl Belief propagation for the decoding of the LDPC codewords. The algorithm uses the soft-output values to iteratively update two a posteriori probability ratios q^x_{ml} and r^x_{ml}. The probability ratio q^x_{ml} can be defined as the probability that codeword bit node l has the value x, given the information obtained from the checknodes, excluding the checknode m. The probability ratio r^x_{ml} is defined as the probability that the checknode m is satisfied, given that the codeword bit node l has a value of x and that the other bits are independent with probabilities q^x_{ml}. All codeword bit node probabilities are used, excluding the probability q^x_{ml} of codeword bit node l. The steps of the Pearl Belief propagation algorithm using the LLR values are explained in the following sub-sections.

3.5.2.1 Initialization step

In the initialization step, the Belief propagation algorithm assigns the LLR value λ_l for each codeword bit node l as

$$q_{ml} = \lambda_l, \quad \forall \ l, m \tag{3.81}$$

where q_{ml} is the LLR representation of q^1_{ml} and q^0_{ml}.

3.5.2.2 Horizontal step (checknode update)

In the horizontal step, the r_{ml} values, which are the LLR representation of r^1_{ml} and r^0_{ml}, are updated for all check nodes as

$$r_{ml} = \ln \left[\left(1 - \prod_{l' \in \mathcal{L}(m)/l} \frac{1 - \exp(q_{ml'})}{1 + \exp(q_{ml'})} \right) . \left(1 + \prod_{l' \in \mathcal{L}(m)/l} \frac{1 - \exp(q_{ml'})}{1 + \exp(q_{ml'})} \right)^{-1} \right] \tag{3.82}$$

where $\mathcal{L}(m)/l$ refers to all codeword bit nodes connected to checknode m, excluding the codeword bit node l.

3.5.2.3 Vertical step (codeword bit node update)

The vertical step updates the values of q_{ml} for all codeword bit nodes as

$$q_{ml} = \lambda_l + \sum_{m' \in \mathcal{M}(l)/m} r_{m'l} \tag{3.83}$$

where $\mathcal{M}(l)/m$ refers to all checknodes connected to codeword bit l, excluding the checknode bit m.

3.5.2.4 Verifying decoding

After each iteration, the posterior probabilities are calculated as follows:

$$q_l = \lambda_l + \sum_{m \in \mathcal{M}(l)} r_{ml} \tag{3.84}$$

The syndrome is calculated by converting the posterior probabilities to hard output values and multiplying the hard-output with the parity check matrix to determine if the output is a valid codeword. For a valid codeword, the syndrome vector will be an all-zero vector and the Pearl Belief propagation algorithm can terminate. If the syndrome vector has a non-zero entry, the algorithm iterates through the process again from the horizontal step, until a valid codeword is found or the preset number of iterations for decoding has been reached. A decoding failure occurs if no valid codeword is found after the preset number of iterations.

3.6 CONCLUSION

The chapter discussed the various multi-antenna coding techniques designed for flat fading channels, where it was illustrated how these codes were adapted for frequency-selective fading channels. It was illustrated how these codes were implemented in the MIMO-WiMAX platform; chapter 5 presents a performance evaluation of these codes in a realistic mobile environment using the MIMO-WiMAX platform created. The design of the algebraic rotation matrices was discussed, as well as the way in which soft-output values were created for the STC/STFC to be used in conjunction with the LDPC codes. The chapter concludes with a discussion of the STFC-LDPC concatenated scheme, in which the design of the LDPC codes and the Pearl Belief propagation algorithm which was used to decode the LDPC codes are discussed.

CHAPTER FOUR

SPHERE DECODING

4.1 INTRODUCTION

In MIMO decoding we are given the information blocks received from the M_r receive antennas, which can be entangled by a specific multi-antenna code, where we want to estimate the transmitted blocks, which are integers drawn from a specific constellation $\mathcal{A}$ of size $|\mathcal{A}|$. Using optimal ML decoding, an exhaustive search has a very high complexity of $\mathcal{O}(|\mathcal{A}|^{K_t})$, where K_t represents the total dimensions of the multi-antenna code which entangles symbols according to the number of transmit antennas M_t, the number of fading blocks M_b and the frequency order diversity N_L[1]. The decoding complexity grows exponentially with an increase in any of the parameters mentioned.

The encoding procedure based on algebraic rotation matrices is formed by entangling a block of $N_L M_t M_b$ symbols together, having an ML decoding complexity of $\mathcal{O}(|\mathcal{A}|^{N_L M_t M_b})$ (assuming no layering). For a system using $M_t = 4$, $L = 2$ and $M_b = 2$, the ML decoding would require an exhaustive search over 4^{16} possible candidates, which is unfeasible in high performance decoding of systems. With layering the the complexity will increase with a factor of M_t. Methods of alleviating decoding complexity are known as zero-forcing (ZF), minimum mean-square error detectors, nulling-cancelling (NC) and sphere-decoding algorithm (SDA). SDA is the only method of these mentioned that can obtain near-ML performance with reasonably low memory requirements and at a decoding complexity polynomial to the dimension size [78].

[1] Although the frequency order diversity is denoted as L, $N_L = 2^{\log_2 L}$ is used as described in previous chapters.

The chapter begins with a description of the original SDA, illustrating how the decoding complexity is alleviated compared to an exhaustive search ML-decoding scheme. The SDA for the MIMO-WiMAX platform is described, which is a modulation-independent, complex domain SDA using the methods presented in [79] and [80]. This chapter illustrates the decoding method of the multi-antenna codes based on algebraic rotation matrices, as well as how soft-output values are generated for the proposed STFC-LDPC concatenated scheme.

The chapter concludes with a description of how the soft-output values are generated for the soft-output SDA used with the concatenation of the STFC and LDPC codes.

4.2 SPHERE DECODING ALGORITHM

As described in section 3, the multi-antenna codes based on algebraic rotations are divided into J sub-blocks with $J = \frac{N}{K}$. N is the total number of OFDMA tones available and K is designed as described in section 3.3.4. For decoding, an SDA algorithm is implemented for every subblock, where the output for every subblock can be defined as:

$$\mathbf{Y} = \mathbf{HC} + \mathbf{W} = \tilde{\mathbf{H}}\mathbf{S} + \mathbf{W}. \tag{4.1}$$

In the above equation, the output vector $\mathbf{Y}$ is of size $M_r K M_b \times 1$, $\tilde{\mathbf{H}}$ represents the combination of the channel matrix with the precoder matrix based on algebraic rotations and is of size $M_r K M_b \times M_t K M_b$ and S is the information symbol vector consisting of QPSK/QAM symbols and is of size $M_t K M_b$. $\mathbf{W}$ represents the $M_r K M_b$ AWGN noise vector. As mentioned earlier, the rate-1 STFC is designed by repeating the rate-2 SFC over two independent fading blocks having dimensions of $M_r K M_b \times M_t K$ for $\tilde{\mathbf{H}}$ and $M_t K$ for $\mathbf{S}$. For the rate-M_t STFC, the dimensions are as specified initially. For the purpose of the discussion, let $K_d = M_t K M_b$, $M = M_r K M_b$, $N = M_t K M_b$ and for the rate-1 STFC, $K_d = M_t K$, $M = M_r K M_b$ and $N = M_t K$.

The SDA algorithm assumes that the channel matrix is full rank, where methods proposed in [81] can be used if $M_t > M_r$ or when the channel gains are strongly correlated. The optimal solution for the received vector $\mathbf{Y}$ given in equation 4.1 is given as

$$\mathbf{S}_{ML} = \arg \min_{\mathbf{S} \in \mathcal{A}^{K_d}} ||\mathbf{Y} - \tilde{\mathbf{H}}\mathbf{S}||^2. \tag{4.2}$$

The ML equation above is presented for the whole codeword received, forming lattice $\Lambda(\mathbf{H}) := \{\mathbf{x} = \tilde{\mathbf{H}}\mathbf{S} | \mathbf{S} \in \mathcal{A}^{K_d}\}$, where the SDA searches within a hyper sphere of radius r, centred at the receive vector $\mathbf{Y}$ examining all $\tilde{\mathbf{H}}\mathbf{S}$ candidates to find the transmitted lattice point.

The SDA can be divided into three steps :

- Selecting an initial search radius r
- Initializing search with ZF solution
- Searching exhaustively and efficiently within the hypersphere of radius r.

Methods for choosing an initial radius are presented in [78]. For the implementation of the SDA in the MIMO-WiMAX platform (section 4.3), radius reduction methods were implemented after each viable solution found, so the initialization of radius r was set fairly large to ensure that a solution would be found inside the sphere.

The first step in the initialization and searching phase is to transform the sphere centred at the vector received $\mathbf{Y}$ to a new equivalent sphere as follows:

$$\mathbf{S}_{ML} = \arg \min_{\mathbf{S} \in \mathcal{A}^{K_d}} ||\mathbf{Y} - \tilde{\mathbf{H}}\mathbf{S}||^2 = \arg \min_{\mathbf{S} \in \mathcal{A}^{K_d}} ||\mathbf{R}(\mathbf{S} - \hat{\mathbf{S}})||^2. \tag{4.3}$$

In the above equation, $\mathbf{R}$ is the $N \times N$ upper triangle factor in the QR-decomposition $\tilde{\mathbf{H}} = \mathbf{QR}$. $\hat{\mathbf{S}}$ is the ZF solution given as

$$\hat{\mathbf{S}} = \underbrace{(\tilde{\mathbf{H}}^{\mathcal{T}}\tilde{\mathbf{H}})^{-1}\tilde{\mathbf{H}}^{\mathcal{T}}}_{\text{Pseudoinverse}}\mathbf{Y}. \tag{4.4}$$

Equation 4.3 searches through a newly defined hypersphere for $\mathbf{S}$ candidates to find the lattice point $\mathbf{RS}$ closest to the centre of the sphere located at $\mathbf{R}\hat{\mathbf{S}}$. No information is lost by transforming to the new equivalent sphere as $\hat{\mathbf{S}}$ and $\mathbf{Y}$ are related through a one-to-one mapping. The reason the sphere is transformed into a new equivalent form is that the upper-triangle form

of $\mathbf{R}$ enables a recursive search in a tree format to find the optimal lattice point closest to the centre of the sphere. With a recursive search, any of the known tree searching strategies can be employed to search efficiently to find the optimal solution.

Starting from dimension K_d and proceeding backwards to the first entry, the newly defined sphere can be expressed in a recursive form as

$$\begin{aligned} ||\mathbf{R}(\mathbf{S}-\hat{\mathbf{S}})||^2 &= R^2_{K_d,K_d}[S_{K_d}-\hat{S}_{K_d}]^2 \\ &\quad + R^2_{K_d-1,K_d-1}\left[S_{K_d-1}-\hat{S}_{K_d-1}+\frac{R_{K_d-1,K_d}}{R_{K_d-1,K_d-1}}(S_{K_d}-\hat{S}_{K_d})\right]^2 \\ &\quad + \cdots + R^2_{1,1}\left[S_1-\hat{S}_1+\frac{R_{1,2}}{R_{1,1}}(S_2-\hat{S}_2)+\cdots+\frac{R_{1,M_t}}{R_{1,1}}(S_{K_d}-\hat{S}_{K_d})\right]^2 \\ &= R^2_{K_d,K_d}(S_{K_d}-\rho_{K_d})^2 + R^2_{K_d-1,K_d-1}(S_{K_d-1}-\rho_{K_d-1})^2+\cdots \\ &\quad + R^2_{1,1}(S_1-\rho_1)^2 \end{aligned} \tag{4.5}$$

where $\rho_{K_d}=\hat{S}_{K_d}$ and $\rho_k=\hat{S}_k-\sum_{j=k+1}^{K_d}\frac{R_{k,j}}{R_{k,k}}(S_j-\hat{S}_j)$, $1\leq k<K_d$. The eminent tree structure is illustrated by equation 4.5, where it can be seen that each value of ρ_k depends on $S_{k+1},\ldots,S_{K_d}$.

In order to confine the search within search radius r, candidates for each dimension from K_d to 1 have to satisfy the following inequality:

$$\rho_k-\frac{\tau_k}{R_{k,k}}\leq S_k\leq\rho_k+\frac{\tau_k}{R_{k,k}},\qquad k=K_d\ldots 1. \tag{4.6}$$

In the above equation, $\tau_{K_d}=r$ and $\tau_k=\left[r^2-\sum_{i=k+1}^{K_d}R^2_{i,i}(S_i-\rho_i)^2\right]^{1/2}$ represents the radius reduction that is effected after fixing the candidates of $\{S_i\}_{i=k+1}^{K_d}$. Every possible value for S_k satisfying the inequality presents a viable solution for the transmitted symbol at the specific dimension. If no candidate is found for a specific dimension, the initial radius chosen is too small and has to be increased to find a viable solution within the sphere.

The search algorithm starts at dimension K_d and will always choose the best possible solution per dimension, which is closest to the lower bound of the inequality in 4.6. At dimension

K_d, the best candidate solution closest to lower bound $S_{K_d} - r/R_{K_d,K_d}$ is chosen, where the algorithm will move down to dimension $K_d - 1$. The inequality for candidates at this interval will be dictated by:

- The value chosen for $S_{K_d}^{(1)}$ at the previous step
- The selected radius r, as the radius is updated for each value chosen per dimension
- The entries $\mathbf{R}$ and $\hat{\mathbf{S}}$ obtained from the initialization phase.

This procedure will continue until a dimension is reached for which there is no viable candidate. If this does not happen, choosing a candidate per dimension will yield a possible solution vector $\mathbf{S}^{(1)} = [S_{K_d}^{(1)}, S_{K_d-1}^{(1)}, \ldots, S_2^{(1)}, S_1^{(1)}]^{\mathcal{T}}$. Each solution vector has a corresponding distance associated with it and is given as follows:

$$d_k^2 = \sum_{i=k}^{K_d} R_{i,i}^2 (S_i - \rho_i)^2 = d_{k+1}^2 + R_{k,k}^2 (S_k - \rho_k)^2. \tag{4.7}$$

Searching for the ML solution, the algorithm searches from dimension 2 up to K_d using already computed distances from equation 4.7. After searching through the tree for all possible viable solutions, the vector which is associated with the smallest distance represents the ML solution for the codeword received.

The following section describes how the SDA was implemented in the MIMO-WiMAX platform as a greedy depth-first tree search, doing all computations in the complex domain. The methods implemented also make use of radius reduction methods after a viable solution has been found. Using the SDA, if a viable solution vector is found, it is known that if the solution is not the ML solution; the SDA only has to search within a sphere with radius equal to the distance of the solution found. Using $r^{(1)} = ||\mathbf{R}(\mathbf{S}^{(1)} - \hat{\mathbf{S}})|| < r$, the complexity of the searching algorithm is reduced, as it will reduce the search radius for each viable solution found and if the first solution found is the ML solution, the algorithm can terminate immediately.

4.3 SPHERE DECODING IMPLEMENTATION

The SDA algorithm implemented in the MIMO-WiMAX platform is based on the method introduced in [79] and [80], which is a complex-domain, modulation independent framework

for the SDA.

The upper triangle form R is calculated by a Cholesky factorization [82] of $\tilde{\mathbf{H}}^{\mathcal{H}}\tilde{\mathbf{H}}$. The channel matrix has to be full rank in order to calculate the Cholesky factorization. The matrix $\mathbf{Q}$ is then calculated as $Q_{k,k} = R_{k,k}^2$ and $Q_{k,l} = R_{k,l}/R_{k,k}$ for $k < l$. Using the zero forcing solution as defined in equation 4.4 with the matrix $\mathbf{Q}$, the searching stage starts by finding the ML transmitted sequence.

From [79] and [80], the recursive form of the sphere constraint is expressed with quantities α_k and T_k as

$$\alpha_k = \hat{S}_k + \sum_{l=k+1}^{K_d-1} Q_{k,l}(\hat{S}_l - S_l) = \hat{S}_k + \sum_{l=k+1}^{K_d-1} Q_{k,l}\Delta_l \tag{4.8}$$

where $k = K_d - 1, K_d - 2, \ldots, 0$ and $\Delta_k = \hat{S}_k - S_k$. $T_{K_d-1} = r^2$ with

$$T_k = T_{k+1} - Q_{k+1,k+1}|\alpha_{k+1} - x_{k+1}|^2 \tag{4.9}$$

for $k = K_d - 2, K_d - 3, \ldots, 0$, where T_k represents the remaining square distance between the solution at dimension k and the surface of the sphere. Using these equations that have been defined, the inequality to determine valid constellation points inside the sphere can be expressed as:

$$|\alpha_k - S_k|^2 \leq \frac{T_k}{Q_{k,k}}. \tag{4.10}$$

The algorithm starts at dimension $k = K_d$ and moves down to 0, where a valid solution is found and radius reduction methods are implemented. Note that the S_k values used in the computations above represent the signal constellation as used in the transmission, that is, if the symbols are scaled to unity power, the symbols corresponding to $(1, 1)$ are not necessarily used as $(1, 1)$, but as $1/\sqrt{2}, 1/\sqrt{2}$ in the case of QPSK. The algorithm as implemented from [79] and [80] is illustrated by the block diagram in figure 4.1.

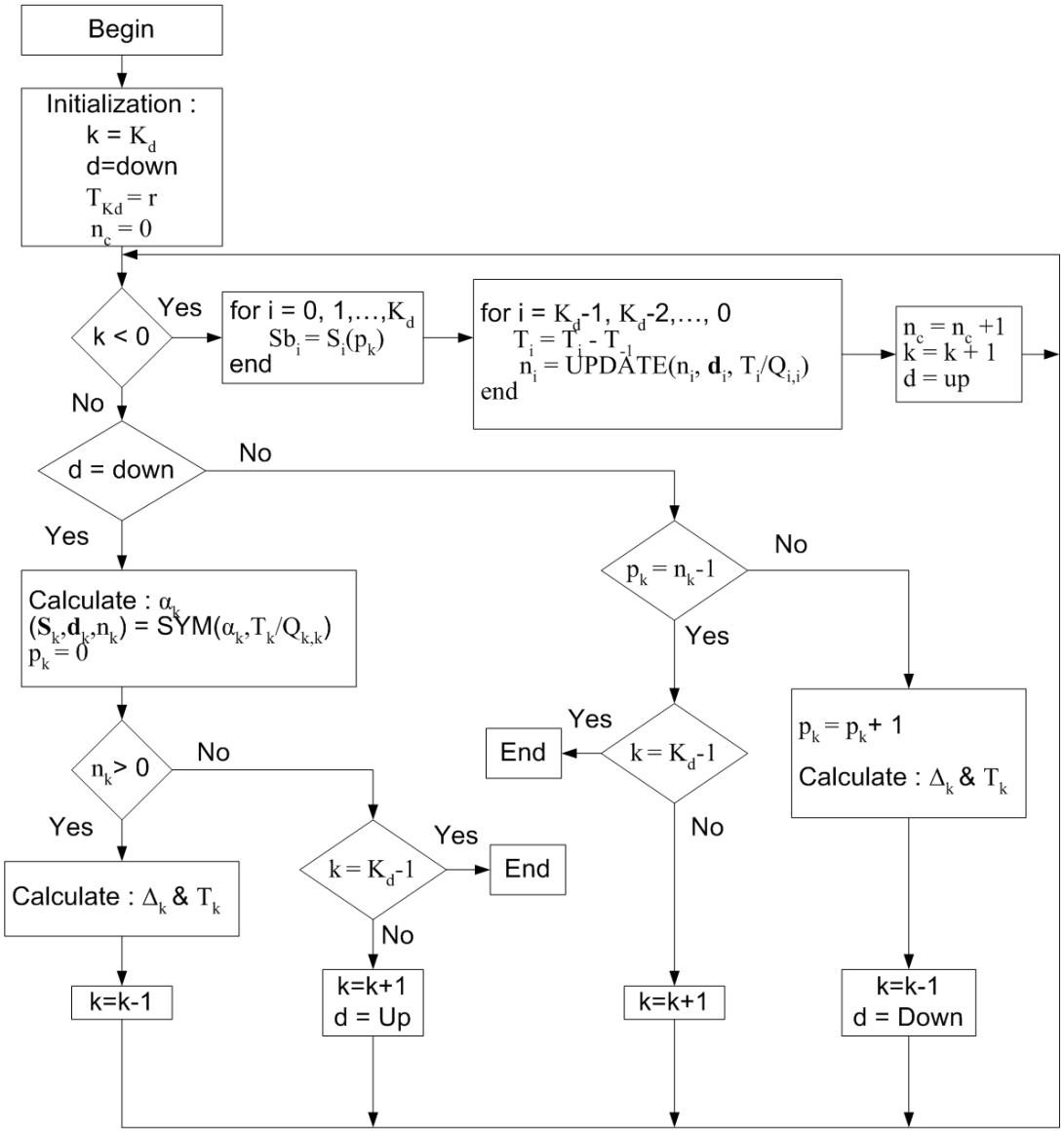

FIGURE 4.1: Flowchart of SDA algorithm implemented for the MIMO-WiMAX platform

All operations defined in block diagram occur in the complex domain and can be used with any constellation that is suitable for use with the MIMO-WiMAX platform, as various modulation schemes are defined in the WiMAX standard. The variable d indicates whether the node has been visited before or not, whereas $d = \text{Down}$ means that the node is visited for the first time. The variable n_c keeps track of the number of solutions found and is only used if list sphere decoding methods (see section 4.4) are implemented for soft-output SDA, as the radius

reduction method employed ensures that the last solution found will always be the best solution.

The function "SYM" generates a list of all viable symbols at the specific dimension, by comparing the symbols with the inequality defined in equation 4.10. It sorts the list $\mathbf{s}_k$ from the best solution to worst, where $\mathbf{d}_k$ represents the associated distances for each symbol and n_k is an integer representing the total number of viable symbols for a specific dimension k. The current symbol index value explored in the tree is denoted as p_k; the value would be increased to point to the next best solution if no viable solution vector was found by exploring the better solution closer to the lower bound.

When a solution vector is found, the vector is stored in the $\mathbf{Sb}$ vector, where the radius of the sphere will be updated to equal the distance of the viable vector found. This means that the solution is now on the surface of the sphere, where the "UPDATE" function will re-evaluate each distance associated with possible solutions per dimension. With the updated list, the searching algorithm will continue to look for solutions using the reduced radius. If another solution is found, the radius can then be further reduced. This continues until no viable solution vector can be found inside a sphere.

The SDA described is also used to produce soft outputs as described in the following section.

4.4 SOFT-OUTPUT SPHERE DECODING

For the proposed STFC-LDPC the SDA should be able to produce soft-output values for the LDPC decoder, as it was shown in [16] that soft-decision decoding shows an asymptotic gain of approximately 3 dB compared to hard-decision decoding. Let $\mathbf{x} = [x_0, x_1, ..., x_{K.M_t.M_c}]$ be the binary vector corresponding to the channel symbol vector $\mathbf{S}$ in equation 4.1, where each symbol in vector $\mathbf{S}$ consists of M_c bits. Using Bayes' rule for maximum a posteriori decoding, the log-likelihood ratio for x_k can be represented as

$$\lambda_L(x_k) = \ln\frac{P(x_k = +1|\mathbf{Y})}{P(x_k = -1|\mathbf{Y})} = \lambda_A(x_k) + \lambda_E(x_k) \tag{4.11}$$

where $\lambda_A(x_k) = \ln[P(x_k = +1)/P(x_k = -1)]$ is the a priori information and $\lambda_E(x_k)$ the

extrinsic information of x_k. Letting $\boldsymbol{\lambda}_A = [\lambda_A(x_1), ..., \lambda_A(x_{K.M_t.M_c})]$, the extrinsic information can be represented as

$$\lambda_E(x_k) = \ln \frac{\sum_{\mathbf{x}\in\mathbb{X}_{k,+1}} P(\mathbf{Y}|\mathbf{x}) \exp\{\frac{1}{2}\mathbf{x}_{[k]}^{\mathcal{T}}\boldsymbol{\lambda}_{A,[k]}\}}{\sum_{\mathbf{x}\in\mathbb{X}_{k,-1}} P(\mathbf{Y}|\mathbf{x}) \exp\{\frac{1}{2}\mathbf{x}_{[k]}^{\mathcal{T}}\boldsymbol{\lambda}_{A,[k]}\}} \tag{4.12}$$

where $\mathbb{X}_{k,+1} = \{\mathbf{x}|x_k = +1\}$, $\mathbb{X}_{k,-1} = \{\mathbf{x}|x_k = -1\}$, $\mathbf{x}_{[k]}$ is the subvector of $\mathbf{x}$ obtained after omitting its k^{th} entry x_k and similarly for $\boldsymbol{\lambda}_{A,[k]}$, which comes from $\boldsymbol{\lambda}_A$ after removing $\lambda_A(x_k)$. The likelihood function $P(\mathbf{Y}|\mathbf{x})$ is calculated as

$$P(\mathbf{Y}|\mathbf{S} = \text{map}(\mathbf{x})) = \frac{\exp\left[-\frac{1}{2\sigma^2}||\mathbf{Y} - \tilde{\mathbf{H}}\mathbf{S}||^2\right]}{(2\pi\sigma^2)^N}. \tag{4.13}$$

For the calculation of the log-likelihood ratios, only the term in the exponent is relevant, and the constant factor outside the exponent can be omitted. Further simplifications are possible using the Max-log approximation defined as follows:

$$\ln(e^{a_1} + e^{a_2}) = \max(a_1, a_2). \tag{4.14}$$

A refinement factor can be added to the Max-log approximation, which is known as the Jacobian logarithm and is defined as follows:

$$\ln(e^{a_1} + e^{a_2}) = \max(a_1, a_2) + \underbrace{\ln(1 + e^{-|a_1 - a_2|})}_{Refinement factor}. \tag{4.15}$$

The refinement factor was neglected in simulations, as it was found in [83] that the performance degradation, by excluding the factor, is often very small. Using the Max-log approximation, the extrinsic value can be expressed as

$$\lambda_E(x_k|\mathbf{Y}) \approx \frac{1}{2}\max_{\mathbf{x}\in\mathbb{X}_{k,+1}}\left\{-\frac{1}{\sigma^2}||\mathbf{Y}-\tilde{\mathbf{H}}.\mathbf{S}||^2+\mathbf{x}_{[k]}^{\mathcal{T}}\boldsymbol{\lambda}_{A,[k]}\right\}-\frac{1}{2}\max_{\mathbf{x}\in\mathbb{X}_{k,-1}}\left\{-\frac{1}{\sigma^2}||\mathbf{Y}-\tilde{\mathbf{H}}.\mathbf{S}||^2+\mathbf{x}_{[k]}^{\mathcal{T}}\boldsymbol{\lambda}_{A,[k]}\right\}. \tag{4.16}$$

Methods to solve equation 4.16 are known as list sphere decoding [84] and soft-to-hard

conversion for soft-decision sphere decoding [85].

List sphere decoding uses the SDA to generate the L_s best solutions, where L_s is usually in the range of $100 - 500$. $L_s = 1$ corresponds to the hard-output SDA and the higher the value of L_s, the more accurate the soft-output values will be. The algorithm starts by setting the initial radius r to a very large value until L_s viable solutions are found. Instead of reducing the radius to the best solution found as in the case of the hard-output SDA, the radius is reduced to the distance of the L_s solution. Only if a solution is found which is better than the L_s solution, the new vector will replace the last entry of the possible solutions. This procedure continues until the L_s best solutions have been found. Equation 4.16 is solved by using the vector list for each $x_k = 1$ and $x_k = -1$, searching for the vector with the lowest distance with the corresponding x_k value being a 1 and a -1. If no vector is found for $x_k = 1$ or $x_k = -1$, the value of LLR is set to a predefined threshold, with virtual certainty that the corresponding value is not the value for x_k, which was not found in the vector list.

The soft-to-hard conversion method [85] is the other method to produce the soft-output values and is the method that was implemented in the MIMO-WiMAX platform. The first step of the algorithm is to rewrite the complex signal representation into a real equivalent system. For QPSK signaling, the real equivalent representation for each row in the received vector from equation 4.1 can be written as

$$\begin{bmatrix} y_{0,r} \\ y_{0,i} \end{bmatrix} = \begin{bmatrix} \tilde{H}_{0,r} & -\tilde{H}_{0,i} \\ \tilde{H}_{0,i} & \tilde{H}_{0,r} \end{bmatrix} \begin{bmatrix} S_{0,r} \\ S_{0,i} \end{bmatrix} + \begin{bmatrix} W_{0,r} \\ W_{0,i} \end{bmatrix}. \tag{4.17}$$

The real equivalent representation for 16-QAM modulation is different from the QPSK representation in equation 4.17, where details of the transformation can be found in [85]. The soft-to-hard conversion then starts of by rewriting equation 4.16 as

$$\begin{aligned} \lambda_E(x_k|\mathbf{Y}) \approx & \frac{1}{2} \max_{\mathbf{x}_r \in \mathbb{X}_{k,+1}} \left\{ -\frac{1}{\sigma^2} ||\mathbf{Y}_r - \tilde{\mathbf{H}}_r.\mathbf{x}_r||^2 + \mathbf{x}_r^{\mathcal{T}} \boldsymbol{\lambda}_A \right\} \\ & -\frac{1}{2} \max_{\mathbf{x}_r \in \mathbb{X}_{k,-1}} \left\{ -\frac{1}{\sigma^2} ||\mathbf{Y}_r - \tilde{\mathbf{H}}_r.\mathbf{x}_r||^2 + \mathbf{x}_r^{\mathcal{T}} \boldsymbol{\lambda}_A \right\} - \lambda_A(x_k) \end{aligned} \tag{4.18}$$

where $\mathbf{Y}_r$, $\mathbf{x}_r$ and $\tilde{\mathbf{H}}_r$ represent the real equivalent system of the parameters from equation 4.16.

With $\tilde{\mathbf{H}}_r$ being full rank, there can always be a vector $\tilde{\mathbf{Y}}_r$ satisfying:

$$2\tilde{\mathbf{H}}_r^{\mathcal{T}}\tilde{\mathbf{Y}}_r = \sigma^2\boldsymbol{\lambda}_A. \tag{4.19}$$

A new equation for the soft outputs can be represented by combining equation 4.18 and 4.19 as follows:

$$\begin{aligned}\lambda_E(x_k|\mathbf{Y}) \approx & \frac{1}{2\sigma^2}\min_{\mathbf{x}_r\in\mathbb{X}_{k,+1}}\left\{||\mathbf{Y}_r+\tilde{\mathbf{Y}}_r-\tilde{\mathbf{H}}_r.\mathbf{x}_r||^2\right\} \\ & +\frac{1}{2\sigma^2}\min_{\mathbf{x}_r\in\mathbb{X}_{k,-1}}\left\{||\mathbf{Y}_r+\tilde{\mathbf{Y}}_r-\tilde{\mathbf{H}}_r.\mathbf{x}_r||^2\right\}-\lambda_A(x_k).\end{aligned} \tag{4.20}$$

Using the output of the hard-output sphere decoder as

$$\hat{\mathbf{x}}_{map} = \arg\min_{\mathbf{x}_r\in\mathbb{X}}||\mathbf{Y}_r+\tilde{\mathbf{Y}}_r-\tilde{\mathbf{H}}_r.\mathbf{x}_r||^2 \tag{4.21}$$

equation 4.20 can be rewritten in a simplified form as follows:

$$\begin{aligned}\lambda_E(x_k|\mathbf{Y}) \approx & \frac{\hat{x}_{k,map}}{2\sigma^2}||\mathbf{Y}_r+\tilde{\mathbf{Y}}_r-\tilde{\mathbf{H}}_r.\hat{\mathbf{x}}_{map}||^2\Big\} \\ & +\frac{\hat{x}_{k,map}}{2\sigma^2}\min_{\mathbf{x}_r\in\mathbb{X}_{k,-\hat{x}_{k,map}}}\left\{||\mathbf{Y}_r+\tilde{\mathbf{Y}}_r-\tilde{\mathbf{H}}_r.\mathbf{x}_r||^2\right\}-\lambda_A(x_k).\end{aligned} \tag{4.22}$$

Solving equation 4.22 requires one hard-output SDA to find $\hat{\mathbf{x}}_{map}$ and an additional SDA for each k to solve the second part of the equation by forcing the x_k value to be the opposite of $\hat{x}_{k,map}$. The extrinsic values calculated by equation 4.22 are exact under the max-log approximation, but require additional sphere decoding steps for each value of k. The algorithm does not require the same memory storage of the list sphere decoder, but requires additional overhead by additional sphere decoders and conversion of the system to a real equivalent system. The soft-to-hard conversion algorithm was used with the STC and STFC to produce accurate log-likelihood ratios to use with the LDPC codes to obtain high performance with the MIMO-WiMAX platform under various channel conditions.

4.5 CONCLUSION

The chapter gave an overview of the SDA, explaining mathematically how the problem of searching within a hypersphere is solved by transforming the sphere to obtain the solution in a recursive manner. Radius reduction methods were discussed, as well as how the problem can be solved by a depth-first tree search. The algorithm as implemented in the MIMO-WiMAX platform was discussed, which is a modulation-independent SDA algorithm. The chapter concluded with a discussion on how to obtain soft-output values using the SDA. The method implemented in the MIMO-WiMAX platform to produce soft outputs for the concatenation of the LDPC was discussed.

CHAPTER FIVE
RESULTS

5.1 INTRODUCTION

This chapter illustrates the performance evaluation of the multi-antenna coding techniques presented in chapter 3 in various realistic channel conditions using the MIMO-WiMAX platform developed in chapter 2. These coding techniques are usually only evaluated in perfect channel conditions, assuming unrealistic multipath conditions or flat fading channels. Previous analysis of these codes assumes that the transmit and receive antennas are spaced far apart from one another so that there is no correlation between antennas. The channel conditions introduced are realistic, correlated MIMO channels, following the MIMO-WiMAX standard using modern coding techniques, which include the proposed LDPC-STFC. The results in this section only considered the downlink, as additional complications arise when considering the uplink, which were not handled in this study.

Section 5.2 illustrates the effects of multiple antennas and correlated conditions on the capacity of MIMO systems. It shows the severe capacity loss in correlated conditions and shows the importance of using correlated conditions in the performance analysis of MIMO systems. The section also illustrates the performance increase when increasing the number of transmit and receive antennas in terms of BER performance.

Section 5.3 illustrates the performance evaluation of the modern multi-antenna coding techniques in various correlated conditions and using realistic mobile frequency-selective fading channels.

Section 5.4 illustrates the performance gain of using concatenated STC-LDPC and STFC-LDPC codes compared to uncoded conditions presented in section 5.3. The performance gain using STFC-LDPC in block-fading conditions, compared to STC-LDPC codes are illustrated in various channel conditions which include highly correlated conditions, as well as channels using the suburban alternative PDP, which consists of a 20-tap multipath channel.

5.2 MIMO CHANNEL EFFECTS AND CAPACITY RESULTS

In this section, results on the capacity of MIMO channels are presented for spatially correlated channels. Capacity results were evaluated in terms of outage capacity and represented by complementary cummulative distribution function graphs. Outage capacity is defined as the probability that a specific capacity C cannot be achieved. The capacities for the MIMO channels were evaluated using the following assumptions:

- The MIMO channel is known at the receiver, but unknown at the transmitter.
- The total system power is uniformly distributed over all transmit antennas.

Capacities were evaluated for a fixed total transmission power as [86]

$$C = \frac{1}{2B_w} \int_{-B_w}^{B_w} \log_2 \det \left[\mathbf{I}_{M_r} + \frac{\beta}{M_t} . \mathbf{H}(k,f) . \mathbf{H}^{\mathcal{H}}(k,f) \right] df \tag{5.1}$$

where B_w represents the single-sided bandwidth of the baseband signal, β is the SNR at each receiving antenna and $\mathbf{H}(k,f)$ represents the frequency response of the channel transfer function and is given as follows:

$$\mathbf{H}(k,f) = \sum_{l=L1}^{L2} \mathbf{H}_l(k) z^{-l} \Big|_{z=e^{j2\pi f T_s}} . \tag{5.2}$$

In equation 5.2, $\mathbf{H}_l(k)$ is the channel coefficients as represented by equation 2.7 and T_s is the sampling time.

The capacities were measured using the channel model with a Vehicular A PDP defined in the UMTS standards [25] (see Appendix A) with square root raised cosine filters with roll-off factor

$\alpha = 0.5$ as the transmit and receive filters. All the capacity results were obtained for an SNR of $\beta = 15$. CCDF plots were obtained for 2×2, 4×4 and 8×8 MIMO channels using various correlation parameters and are illustrated as follows:

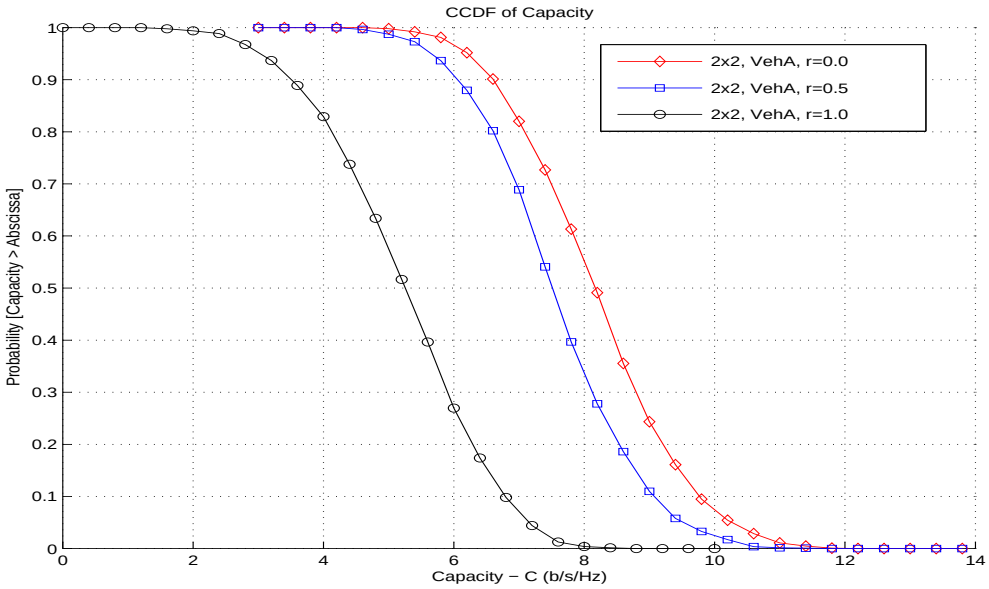

FIGURE 5.1: Capacities for a 2×2 antenna setup using the Vehicular A PDP

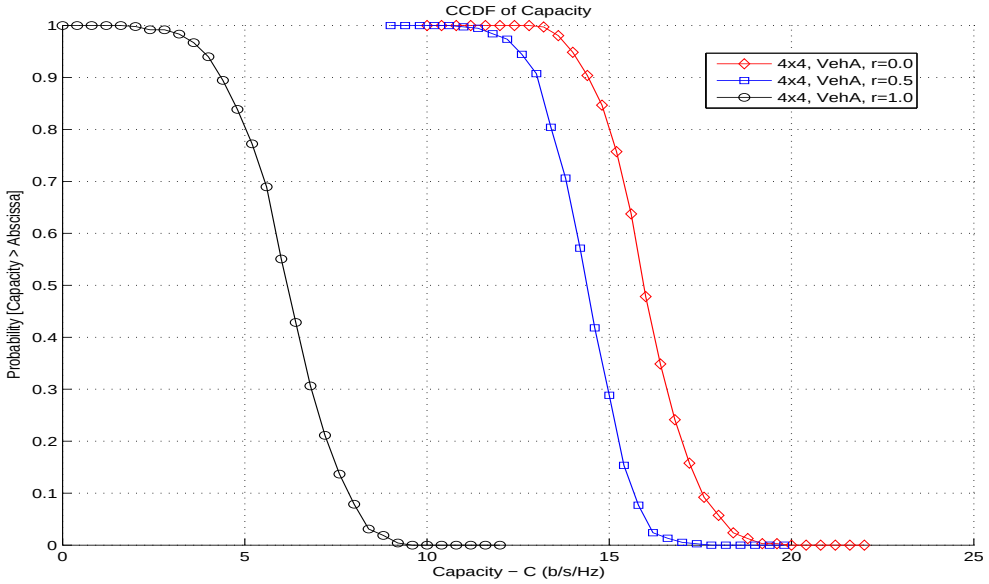

FIGURE 5.2: Capacities for a 4×4 antenna setup using the Vehicular A PDP

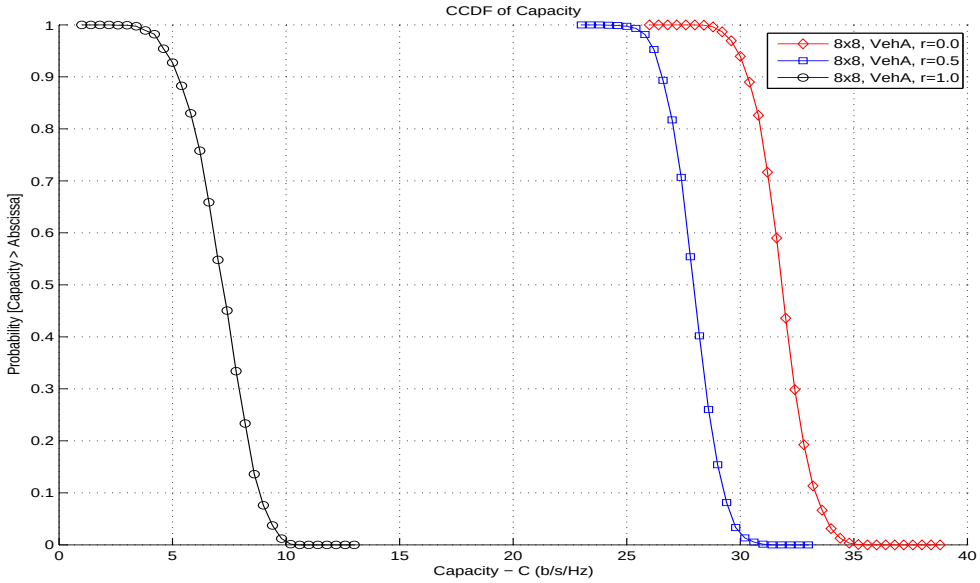

FIGURE 5.3: Capacities for an 8×8 antenna setup using the Vehicular A PDP

Figure 5.1-5.3 illustrates the effects on capacity with an increase in the number of transmit and receive antennas, as well as illustrating the effects of antenna correlation. Antenna correlation was introduced using equation 2.13 for the transmit and receive antennas, using $r = 0.0$, $r = 0.5$ and $r = 1.0$. For $r = 0.0$ and $r = 0.5$, the linear increase in capacities can be observed, when increasing the number of antennas used in the system. As r increases to 1, the capacity increase achieved by increasing the number of antennas is almost negligible. The capacity results shown in figure 5.1-5.3 illustrate the effects of correlation on MIMO capacity and show that the linear increase in capacity decreases for higher antenna correlation.

Figure 5.4 illustrates the effects on capacity when simulating in frequency-selective fading and flat fading conditions. Figure 5.4 illustrates the linear increase in capacity as the number of antennas increases, but for a capacity $\geq$ abscissa ≥ 0.9, which translates to an outage capacity of 10%. It can be seen that frequency-selective fading conditions represented by the Vehicular A PDP have a larger capacity compared to flat fading conditions. MIMO channels using frequency-selective fading channels with OFDM increases diversity, as not all subcarriers experience the same fading conditions. The rich scattering environments offered by frequency-selective fading conditions improve capacity as shown in [86] and this is illustrated in figure 5.4.

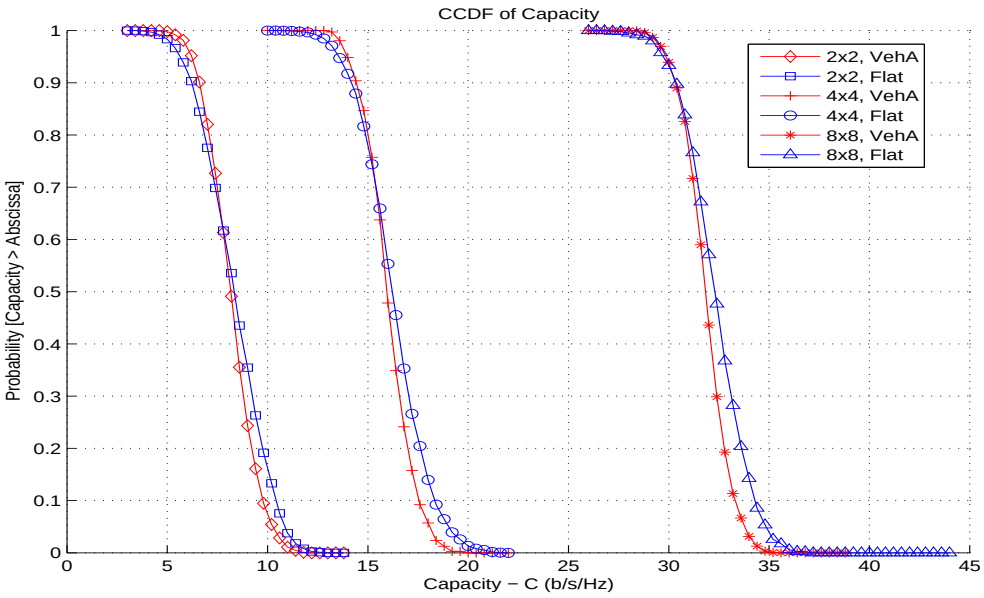

FIGURE 5.4: Capacities for a 2×2, 4×4 and 8×8 antenna setup using the Vehicular A PDP and flat fading conditions

The effects of different spatial parameters were simulated on a BER vs E_b/N_0 graph using the following simulation parameters:

TABLE 5.1: Simulation parameters for various antenna setups using MRC decoding

PDP	Vehicular A
Maximum Doppler spread	$f_d = 100Hz$
Sampling time	$T_s = 0.86\mu$s
Transmit filter	Square root raised cosine, $\alpha = 0.5$
Receive filter	Square root raised cosine, $\alpha = 0.5$
Modulation scheme	QPSK
Encoding technique	None
Decoding method	MRC

No multi-antenna code was implemented where the same data were transmitted from all transmit antennas. The results obtained are illustrated in figure 5.5.

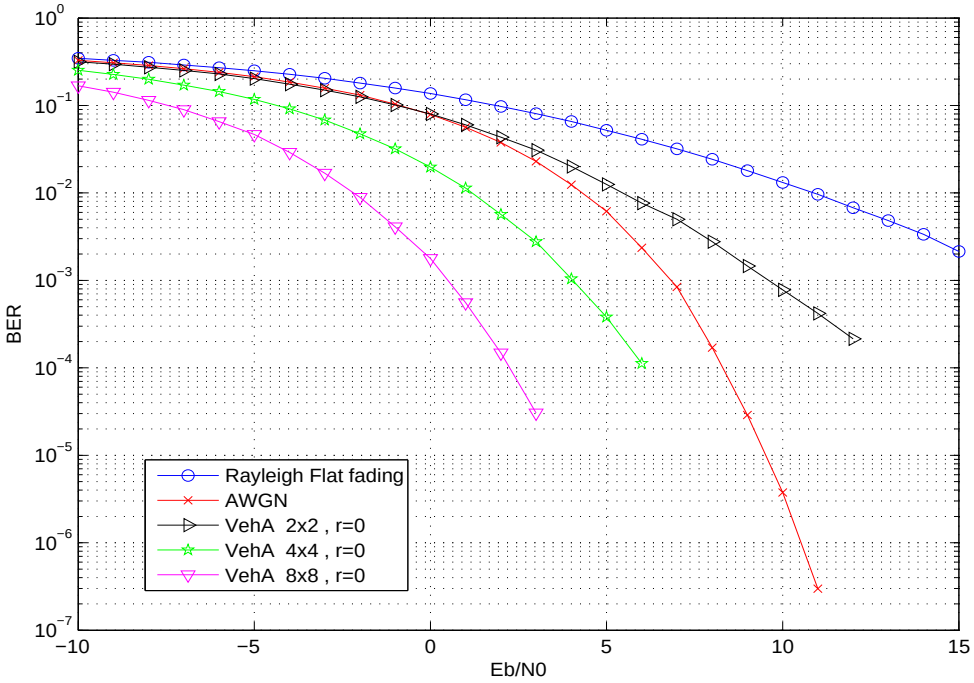

FIGURE 5.5: BER performance for various antenna setups

Figure 5.5 illustrates the performance increase for the same $b/s/h$ for an increased number of antennas used. The 1×1 QPSK flat fading and AWGN channels are inserted as reference graphs. For a BER of 10^{-3}, the 2×2 antenna setup shows an 8 dB increase in performance compared to the Rayleigh flat fading curve. The performance is further improved for the 4×4 and 8×8 antenna setups, showing a 5.5 dB and 9.5 dB performance increase respectively compared to the 2×2 antenna setup.

5.3 PERFORMANCE EVALUATION OF MULTI-ANTENNA CODING TECHNIQUES

Simulations were performed on the MIMO-WiMAX platform created to illustrate the performance of modern multi-antenna coding techniques in various channel conditions. The MIMO-WiMAX parameters chosen for simulations presented in this section are illustrated in Table 5.2.

TABLE 5.2: MIMO-WiMAX simulation parameters

MIMO-WiMAX parameters	
Transmit antennas	2
Receive antennas	2
FFT size	128
Number of sub-channels	2
Users per sub-channel	1
Mode	FUSC
Cyclic prefix length	0.25
Maximum Doppler spread	$f_d = 100Hz$
Sampling time	$T_s = 0.8\mu$s
Channel bandwidth	1.25MHz
Transmit filter	Square root raised cosine, $\alpha = 0.5$
Receive filter	Square root raised cosine, $\alpha = 0.5$

The coding schemes and corresponding conditions in which they were implemented in all the simulations are illustrated in Table 5.3. Modulation schemes were adjusted appropriately to maintain the same b/s/Hz. For comparison purposes, it was chosen at 2 b/s/Hz to be able to compare the coding techniques over various channel conditions.

TABLE 5.3: Coding parameters used in simulations

Code	Modulation	Fading condition	Decoder
STC	QPSK	Quasi-static fading	Single-symbol ML
Rate-1 SFC	QPSK	Block fading	Sphere-decoding
Rate-2 SFC	BPSK	Block fading	Sphere-decoding
Rate-1 STFC	QPSK	Block fading	Sphere-decoding

5.3.1 Performance analysis in an uncorrelated, 2-tap frequency-selective fading channel

The simulation parameters were set up to illustrate the maximum performance of these codes in ideal channel conditions and are summarized in Table 5.4.

TABLE 5.4: Simulation parameters for the performance evaluation in uncorrelated conditions

Channel parameters	
Frequency-selectivity	Two-ray equal power PDP at 0 μs and 8 μs
Time-selectivity	Slow-fading conditions with $f_d = 100Hz$
Space-selectivity	None

The simulations were performed on a two-ray equal power Rayleigh multipath channel (see appendix A) to illustrate the diversity gain capable for a frequency diversity order of 2. For all fading conditions simulated, no time-selectivity was introduced as the coding techniques assume that the channel remains constant for each OFDMA symbol.

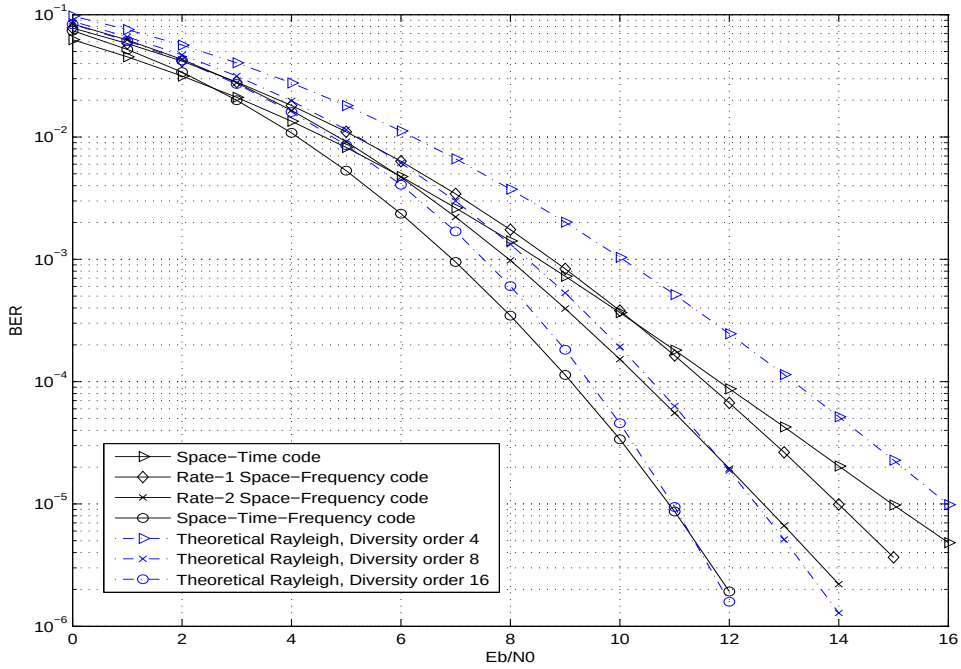

FIGURE 5.6: Results obtained for coding techniques in a two-ray equal power PDP at 0 μs and 8 μs with no space-selectivity

Figure 5.6 illustrates the performance results obtained through simulation, as well as theoretical results for Rayleigh fading channels for a certain degree of diversity. The theoretical results were implemented using MATLAB's built-in functions to obtain a theoretical Rayleigh curve with a specific diversity order. For high E_b/N_0 values, the theoretical results are very similar to those obtained through simulation.

From the simulated results in figure 5.6, it can be seen that the STFC code has a larger slope curve compared to the SFC and STC. This illustrates the larger diversity gain exploited by STFC in block fading conditions. The rate-2 SF code outperforms the rate-1 SF owing to a higher diversity product (see section 3.3.1). The diversity product is also the reason why the rate-1 SF code differs from theoretical diversity gain in Rayleigh channels. The diversity product consists of an intrinsic diversity product, as well as an extrinsic diversity product, which depends on the channel used. Larger delay spreads cause an increase in diversity product for the rate-2 SF code over the rate-1 SF code. The simulation used a very large delay spread (approximately 13 sample delay) which caused the 1.5 dB performance difference. The performance increase for the rate-2 SF code using the large delay spread conforms with the results obtained in [6].

5.3.2 Correlated results for the multi-antenna coding techniques

Simulation results in this section illustrate the performance evaluation of all the multi-antenna coding techniques described in various correlated conditions using a two-ray equal power PDP at 0 μs and 8 μs and the suburban alternative PDP, which is a 20-tap PDP (see appendix A). The space-selectivity was introduced using the exponential correlation matrices as presented by equation 2.13. The following sub-sections will illustrate the results obtained for the various multi-antenna coding techniques in these channel conditions.

5.3.2.1 Space-time code

The results obtained for the STC in the two-ray equal power PDP for various degrees of correlation are illustrated in figure 5.7 and for the suburban alternative PDP in figure 5.8.

For the suburban alternative PDP results from figure 5.8, there is a slight performance loss for correlated results compared to figure 5.7. For $r \leq 0.4$, the degradation is more noticeable, as the highly correlated results showed similar performance for both frequency-selective fading channels. The results are similar at high correlations, as no diversity is gained in terms of MIMO, where the two PDPs will perform similarly in a SISO-OFDM system, assuming there is no inter-carrier interference.

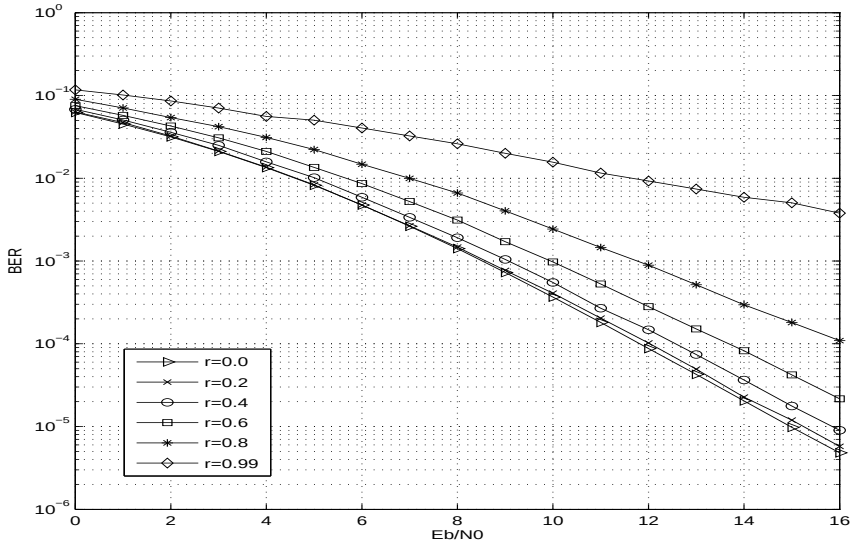

FIGURE 5.7: Results obtained for the STC in a two-ray equal power PDP at 0 μs and 8 μs for various degrees of correlation

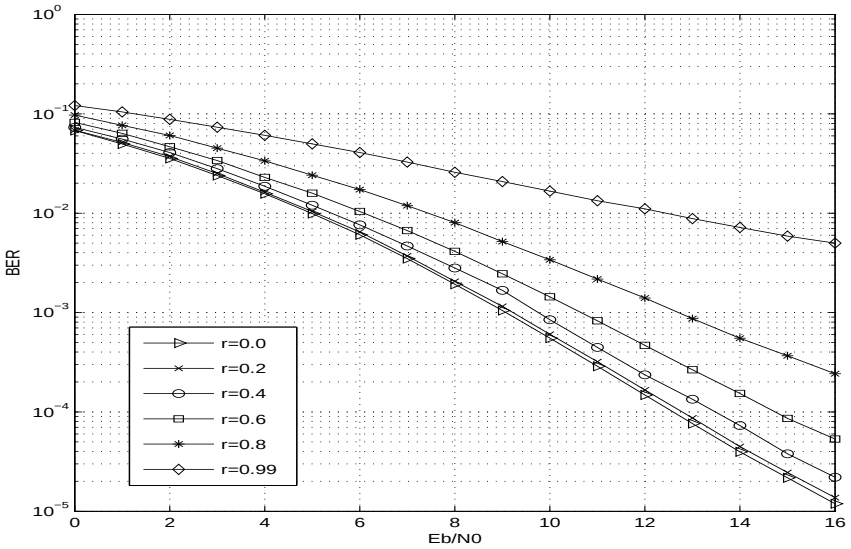

FIGURE 5.8: Results obtained for the STC in a suburban alternative PDP for various degrees of correlation

5.3.2.2 Rate-1 space-frequency code

The results obtained for the rate-1 SFC in the two-ray equal power PDP for various degrees of correlation are illustrated in figure 5.9.

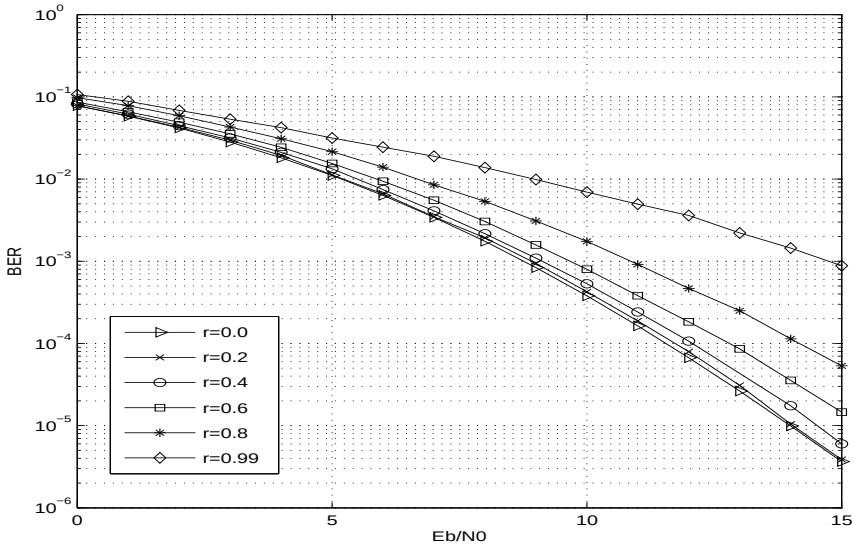

FIGURE 5.9: Results obtained for the rate-1 SFC in a two-ray equal power PDP at 0 μs and 8 μs for various degrees of correlation

The results obtained for the rate-1 SFC in the suburban alternative PDP for various degrees of correlation are illustrated in figure 5.10.

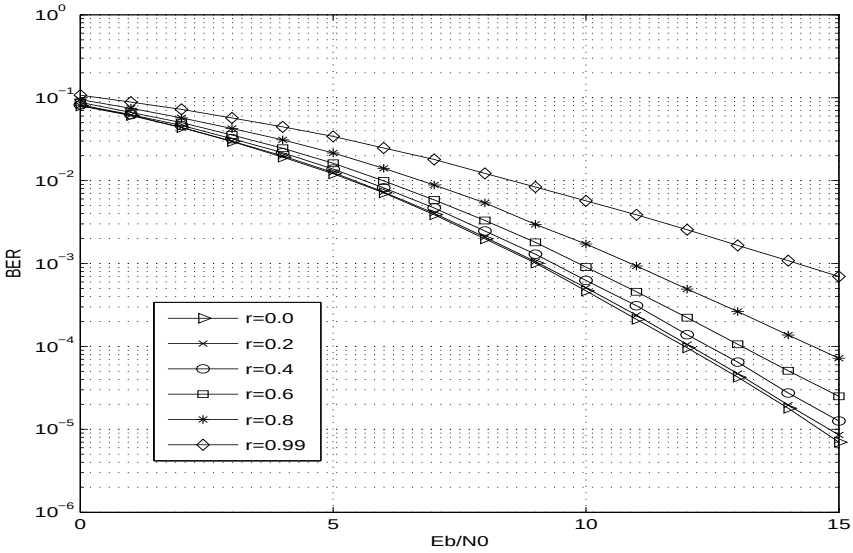

FIGURE 5.10: Results obtained for the rate-1 SFC in a suburban alternative PDP for various degrees of correlation

The degradation for increased correlation from figure 5.9 is less severe than in the results obtained for the STC. The rate-1 SF shows an increase in performance over all correlations for

the two-ray equal power PDP. The results obtained for the suburban alternative PDP from figure 5.10 only show a slight performance degradation compared to the results from figure 5.9. This indicates the good performance of the rate-1 SFC in a high number of taps, frequency-selective fading channel for all correlations.

5.3.2.3 Rate-2 space-frequency code

The results obtained for the rate-2 SFC in the two-ray equal power PDP for various degrees of correlation are illustrated in figure 5.11.

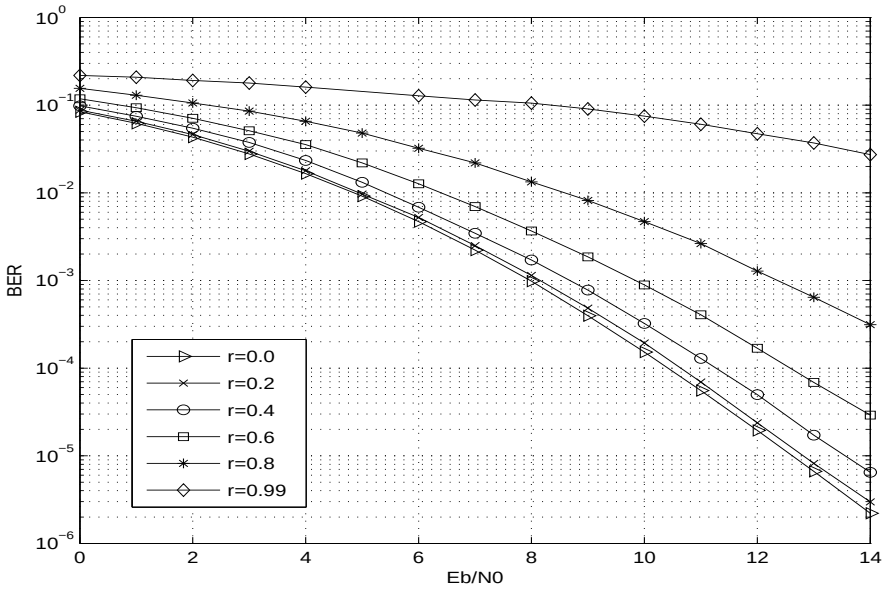

FIGURE 5.11: Results obtained for the rate-2 SFC in a two-ray equal power PDP at 0 μs and 8 μs for various degrees of correlation

The results obtained for the rate-2 SFC in the suburban alternative PDP for various degrees of correlation are illustrated in figure 5.12.

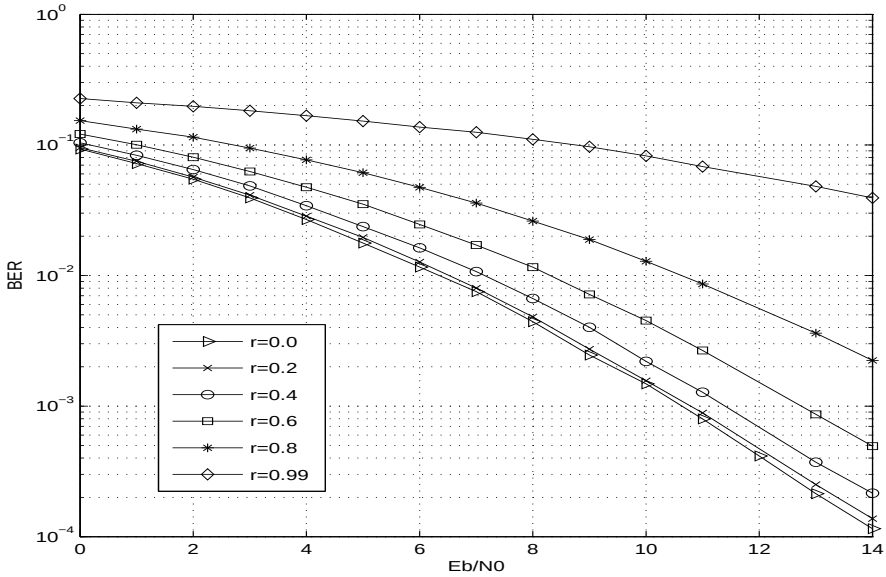

FIGURE 5.12: Results obtained for the rate-2 SFC in a suburban alternative PDP for various degrees of correlation

From figure 5.11 the rate-2 SFC shows much worse performance at high correlation compared to the other multi-antenna codes presented. At low correlation, the rate-2 SFC performs better than the rate-1 SFC for $r \leq 0.4$. According to figure 5.12 the performance of the rate-2 SFC is worse than that of other multi-antenna coding schemes for all correlation values of r. This indicates that the rate-2 SF does not perform as expected in a MIMO highly frequency-selective channel. Note that the code is only designed for a frequency order diversity of 2, where expected results will be obtained if the code is designed to include a higher number of taps. Designing the code for a higher order of diversity increases the decoding complexity (see chapter 4). A comparison of the results for the different SF codes is illustrated in section 5.3.2.5.

5.3.2.4 Space-time-frequency code

The results obtained for the STFC in the two-ray equal power PDP for various degrees of correlation is illustrated in figure 5.13 and for the suburban alternative PDP in figure 5.14

For the two-ray equal power PDP, the STFC performs better compared to the other multi-antenna codes for each respective value of r. For the suburban alternative PDP from figure 5.14, only the rate-1 SFC performs better at high correlations, but overall for correlation

$r \leq 0.6$, the STFC outperforms all the other multi-antenna codes for high number of taps PDPs.

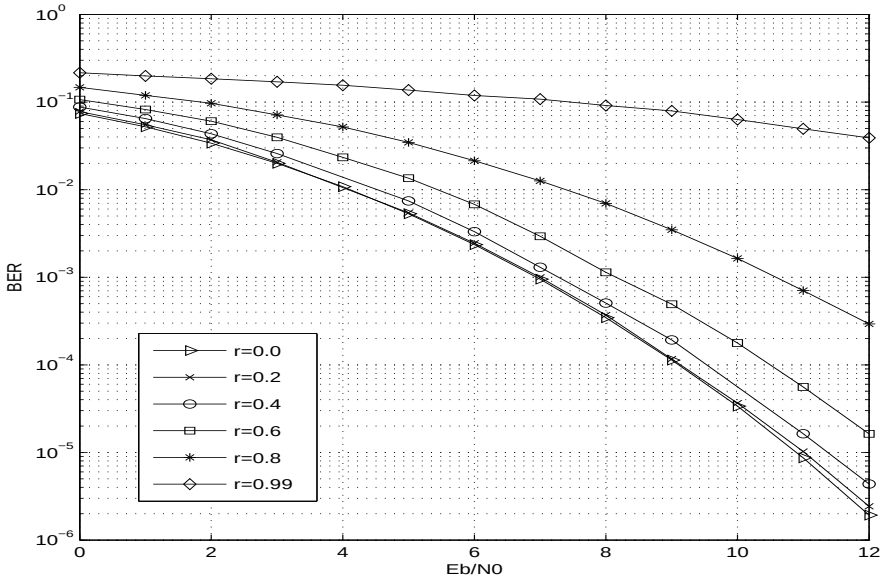

FIGURE 5.13: Results obtained for the STFC in a two-ray equal power PDP at 0 μs and 8 μs for various degrees of correlation

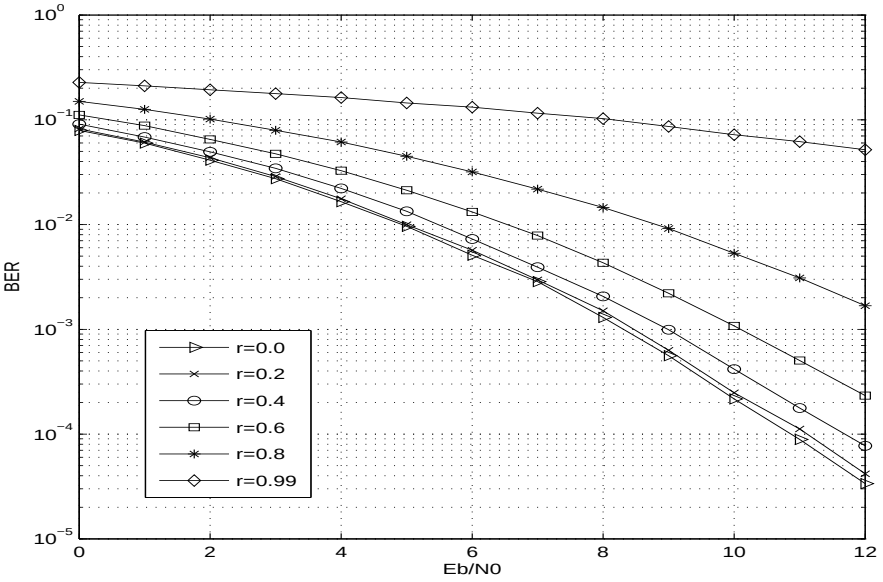

FIGURE 5.14: Results obtained for the STFC in a suburban alternative PDP for various degrees of correlation

5.3.2.5 Performance comparisons

The comparisons of the multi-antenna codes presented for different correlations are illustrated in figure 5.15.

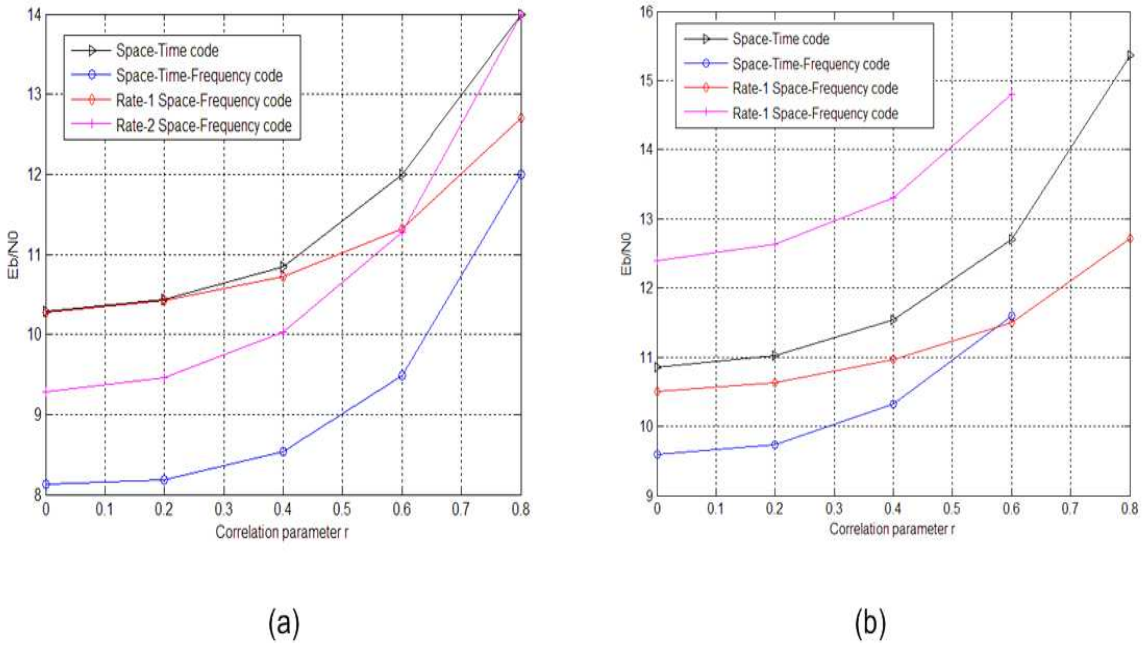

FIGURE 5.15: Performance comparison in (a) two-ray equal power and (b) suburban alternative PDP for various correlations

Figure 5.15 (a) and (b) illustrates a comparison in E_b/N_0 for different correlations to maintain a BER of $10^{-3.5}$. Figure 5.15 (a) illustrates the results obtained for the two-ray equal power PDP at 0 μs and 8 μs and (b) for the suburban alternative PDP. According to (a) the STFC requires the least amount of power to maintain the BER of $10^{-3.5}$. It also indicates that the rate-2 SFC will perform better than the rate-1 SFC for $r \leq 0.6$.

For the suburban alternative PDP, the STFC performs best for $r \leq 0.6$, where the rate-1 SFC shows the best performance for highly correlated conditions. The rate-2 SFC has the worst performance for all correlated conditions in the suburban alternative PDP.

The performance comparison for highly correlated conditions was simulated in terms of E_b/N_0 versus BER with the following parameters, described in table 5.5.

TABLE 5.5: Simulation parameters for highly correlated channel conditions

Channel parameters	
Frequency-selectivity	Two-ray equal power PDP at 0 μs and 8 μs
Time-selectivity	Slow-fading conditions with $f_d = 100Hz$
Space-selectivity	Exponential correlation matrix with r = 0.7

Figure 5.16 illustrates the results obtained for simulating the highly correlated conditions.

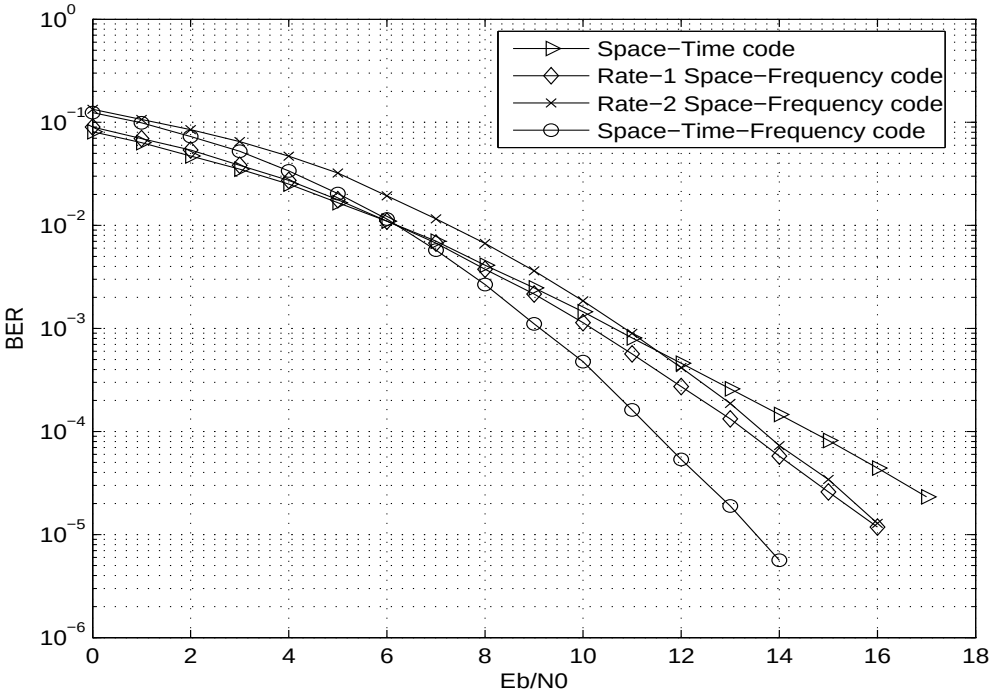

FIGURE 5.16: Results obtained for coding techniques in a two-ray equal power PDP at 0 μs and 8 μs using an exponential correlation matrix with r = 0.7

It clearly illustrates the performance degradation due to correlated MIMO channels. Compared to figure 5.6, each curve suffers a performance loss of approximately 3 dB. The results obtained follow the theoretical analysis from [24], which shows that a 70% correlation will result in a 3 dB loss compared to uncorrelated conditions.

The STFC crosses the STC graph at 6 dB, whereas in figure 5.6, the STFC already showed improvement at around 2.5 dB - 3 dB. These results illustrate the degradation in performance

of high diversity codes in highly correlated channels at lower Eb/N_0 values. At high Eb/N_0 values, the rate-1 SF and rate-2 SF differ less than a 0.5 dB, whereas in Figure 5.6, the rate-2 showed a significant improvement over all Eb/N_0 values. This is due to a lower diversity product, where the extrinsic diversity product is dependent on the channel, which is highly correlated, reducing overall diversity in the channel.

5.3.3 Performance results for realistic mobile channels

The simulation parameters were set up to illustrate the performance of these coding techniques in a realistic mobile environment. Codes are usually only illustrated and simulated in ideal conditions, neglecting correlations between antennas and excluding large number of paths for frequency selective conditions. Using techniques described in chapter 2, the correlation matrices in the model are capable of introducing the appropriate correlation in the system by only defining the antenna spacing, angle of arrival and the angular spread. The parameters for the simulation are summarized in Table 5.6.

TABLE 5.6: Simulation parameters for a realistic mobile environment

Channel parameters	
Frequency-selectivity	Suburban alternative
Time-selectivity	Slow-fading conditions with $f_d = 100Hz$
BS antenna spacing	12λ
MS antenna spacing	0.5λ
Angle of arrival	$90°$
Angular spread	$10°$

The results obtained for simulating these codes in these conditions are illustrated in Figure 5.17.

As with the highly correlated channel, the results reflected in figure 5.17 show a significant performance loss compared to the ideal situation in figure 5.6. The results also illustrate that the performance increase of the STFC compared to the other codes is significantly less. Only the STFC shows an improvement over the rate-1 SFC and STC, whereas the rate-2 SFC suffers a huge performance loss. Better performance can be obtained for the rate-2 SFC, if the code is designed for a larger frequency diversity order L, but will increase decoding complexity.

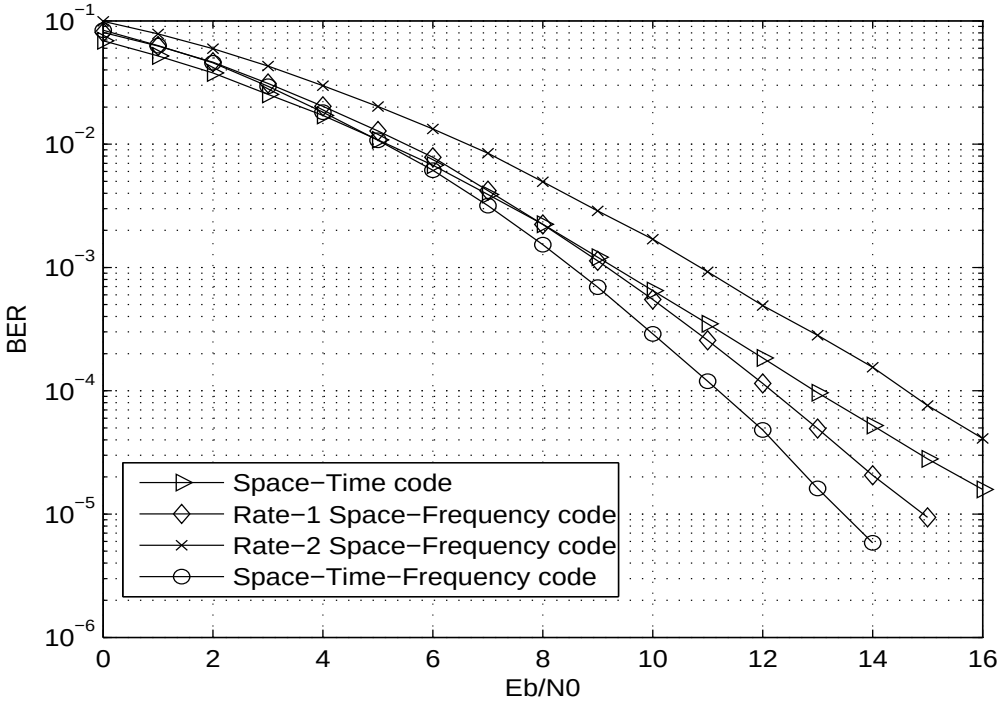

FIGURE 5.17: Results obtained for coding techniques in a suburban alternative power delay profile in a realistic mobile environment

5.4 PERFORMANCE EVALUATION OF STC-LDPC AND STFC-LDPC CONCATENATED CODES

In this section we will discuss the results obtained by simulating the STC-LDPC and STFC-LDPC concatenated coding schemes as presented in sections 3.3.4 and 3.5. Simulations were performed on the MIMO-WiMAX platform using parameters illustrated in table 5.7.

The STC-LDPC codes assume quasi-static fading conditions, where all the STFC-LDPC codes were simulated in block-fading conditions. LDPC codes considered were a cyclic LDPC code defined in the IEEE 802.16e-2005 standard (WiMAX) [1] and an LDPC code based on density evolution using a Gaussian approximation for the probability distribution function of the log-likelihood ratios [74]. The LDPC codes were decoded using the Pearl-Belief propagation algorithm as described in [37].

The results for the performace of the STC-LDPC and STFC-LDPC codes using a two-ray equal

TABLE 5.7: MIMO-WiMAX parameters for the STC-LDPC and STFC-LDPC codes

MIMO-WiMAX parameters	
Transmit antennas	2
Receive antennas	2
FFT size	128
Mode	FUSC
Cyclic prefix length	0.25
Maximum Doppler spread	$f_d = 100Hz$
Sampling time	$T_s = 0.8\mu$s
Channel bandwidth	1.25MHz
Transmit filter and receive filter	Square root raised cosine, $\alpha = 0.5$
LDPC rate	$\frac{1}{2}$-rate codes
Block length	2 304 bits
LDPC decoding	Pearl-Belief propagation with 1 000 iterations

power PDP at 0 μs and 8 μs are illustrated in figures 5.18 and 5.19.

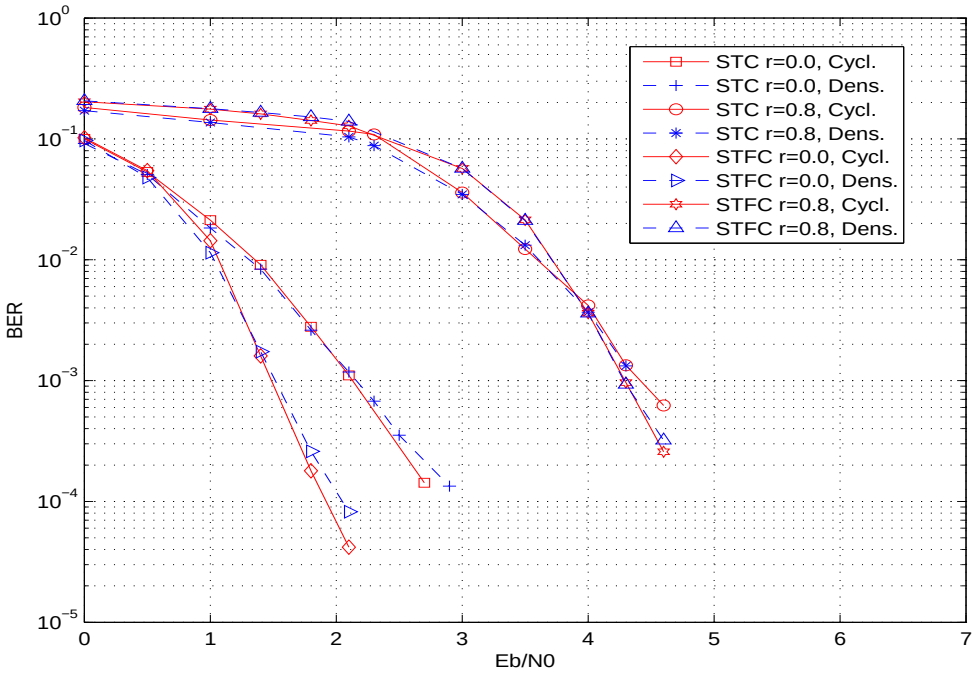

FIGURE 5.18: Results obtained for the STC-LDPC and STFC-LDPC codes in a two-ray equal power PDP at 0 μs and 8 μs using various correlations.

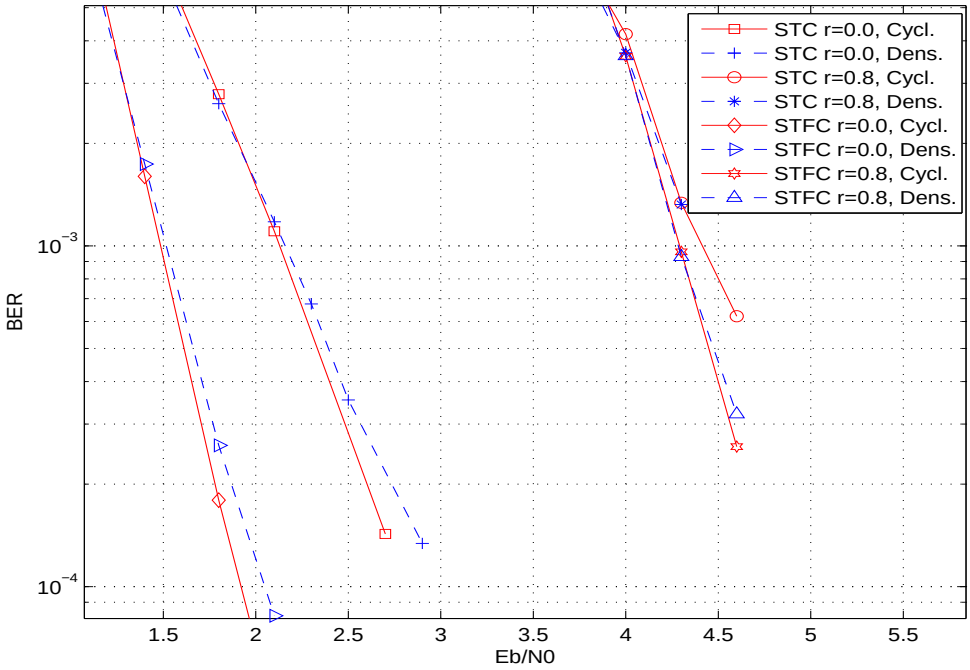

FIGURE 5.19: Closer view of the results obtained in figure 5.18

Figure 5.19 represents a closer view of the simulation results obtained. From figure 5.18 and 5.19, one can clearly see the coding gain advantage of the STC-LDPC and STFC-LDPC compared to previous results obtained for uncoded variations presented in section 5.3. The proposed STFC-LDPC concatenated scheme shows approximately a 0.8 dB increase compared to the STC-LDPC based code for $r = 0.0$. For $r = 0.8$, the codes have similar performance at lower E_b/N_0, whereas at high E_b/N_0, the STFC-LDPC shows increased performance.

The results for the STC-LDPC and STFC-LDPC codes using the suburban alternative, are illustrated in figure 5.20 and 5.21. For channels with high frequency-selectivity, the STFC-LDPC shows an increase in performance of approximately 1.5 dB for $r = 0.0$. For $r = 0.8$, the performance increase was more substantial compared to the case of figure 5.18 and 5.19. The performance increase was approximately 0.6 dB, where the results in figure figure 5.18 and 5.19 had negligible performance increase for $r = 0.8$.

The proposed STFC-LDPC scheme shows improved performance compared to the conventional STC concatenated with LDPC codes. For various channels and correlation, the STFC-LDPC

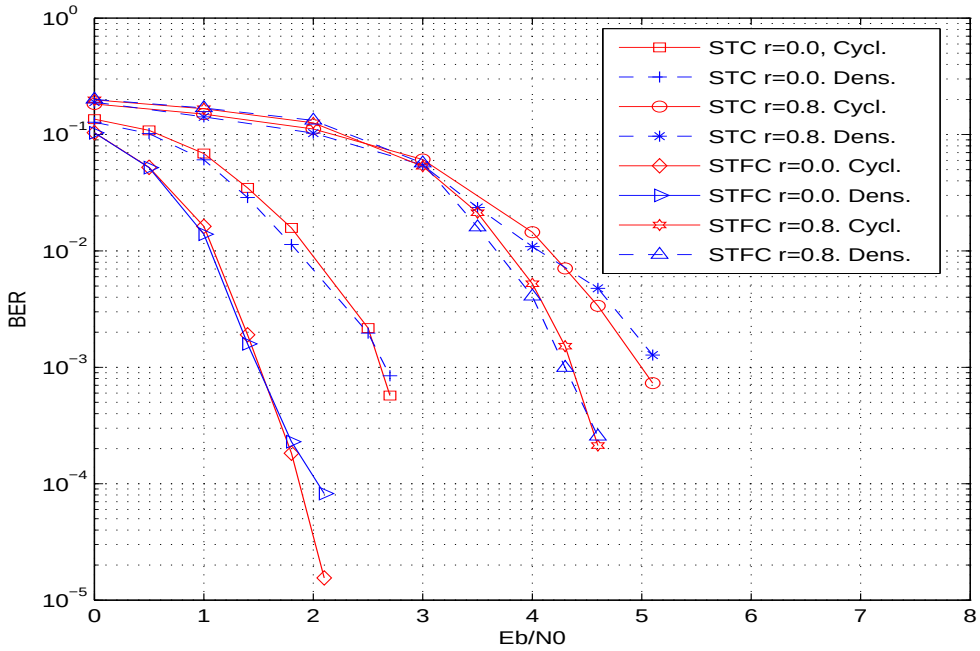

FIGURE 5.20: Results obtained for the STC-LDPC and STFC-LDPC codes in a suburban alternative PDP using various correlations.

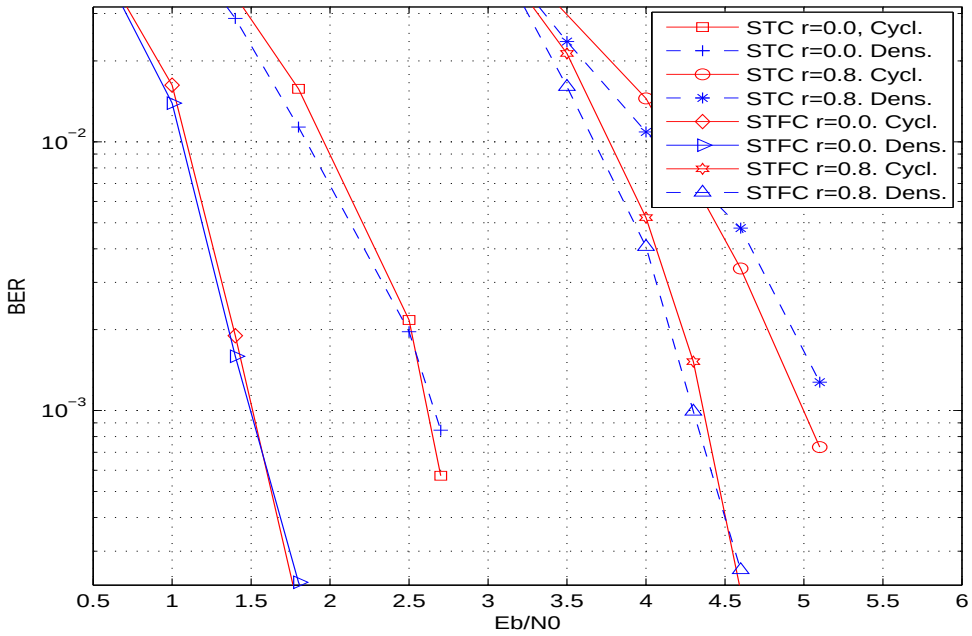

FIGURE 5.21: Closer view of the results obtained in figure 5.20

always outperforms the STC-LDPC, but has increased decoding complexity using soft-output sphere decoding techniques (see chapter 4), compared to single-symbol soft-output decoding. In all the simulations, the LDPC codes based on density evolution yielded approximately the same performance as the cyclic LDPC codes.

5.5 CONCLUSION

This chapter illustrated simulation results for the MIMO-WiMAX channel simulator created and described in chapter 2. The chapter presented capacity results for various antenna setups and correlations and illustrated the need to include correlated conditions for representation of realistic mobile environments.

The simulator was used to analyze the modern multi-antenna coding techniques in various mobile environments, where interesting results were presented for the codes in highly correlated conditions. Comparisons were made between the various coding strategies for a high number of taps, frequency-selective and space-selective fading conditions.

The design of the soft-output sphere decoding methods for the STFC presented in chapters 3 and 4 was used in conjunction with the MIMO-WiMAX platform to provide suitable soft-output values for the use of the proposed STFC-LDPC concatenated coding scheme. The STFC-LDPC scheme was compared to the uncoded STC, SFC and STFC codes and showed a dramatic increase in performance. Comparisons were made for various channel conditions between the LDPC-STFC and LDPC-STC coding schemes, where STFC-LDPC showed improvements under various channel conditions. The higher diversity inherent in the STFC produces a performance increase in the concatenated STFC-LDPC code and is a suitable coding technique for high-performance MIMO systems.

CHAPTER SIX

CONCLUSION AND FUTURE RESEARCH

6.1 CONCLUDING REMARKS

In this dissertation, a suitable MIMO-WiMAX platform was created according to the 802.16e2005 air interface using FUSC mode. Wireless propagation effects were identified in chapter 2 to resemble realistic wireless environments. It was illustrated how these propagation effects were implemented in a suitable MIMO channel model and combined with the WiMAX interface to form a simulation platform resembling realistic mobile environments.

Using the model created, chapter 5 began with results illustrating the effects of the MIMO channel on capacity. The results illustrated the increase in capacity, when the number of transmit and receive antennas was increased. It was shown that introducing correlation at the transmitter or receiver reduces the capacity in the MIMO channel drastically.

The multi-antenna codes discussed in chapter 3 were evaluated on the MIMO-WiMAX platform using various correlated conditions. The multi-antenna codes suffered a performance loss of approximately 3 dB at 70% antenna correlation, where the performance of the rate-2 SFC degraded most in highly correlated and realistic PDP environments. Performance comparisons between the multi-antenna codes illustrated that the STFC will have the best performance in a high number of taps PDP with correlation of less than 60% at the transmitter and the receiver. Further results in realistic mobile environments illustrated that correlated conditions and realistic PDPs with a high number of taps cannot be ignored in the performance analysis of these recent coding advances in mobile environments.

A proposed coding STFC-LDPC concatenated coding scheme was designed and the soft-output values for use with a soft-output SDA were presented in chapter 3. The LDPC codes were optimized using density evolution analysis; proper distributions for the pairs $(\lambda(x), \rho(x))$ were found in [76] for the initial density $a_0(\lambda_L(x_k)$ that is given in equation 3.76. The STFC-LDPC proved to outperform the more conventional approach of concatenating LDPC codes with STCs, where an analysis was presented for the proposed codes in various realistic mobile environments. This proved to be a good choice for implementation in future standards and system implementations.

6.2 FUTURE RESEARCH

Future research regarding the topics that have been handled in this research includes many interesting problems and can be listed as follows:

- The performance analysis in the dissertation assumed that the channel parameters are known at the receiver, since the analysis of the performance evaluation was done for perfect CSI at the receiver. Channel estimation techniques for MIMO-WiMAX in realistic mobile environments fall outside the scope of this dissertation. Interesting results could be obtained by doing an analysis of these codes in conditions where perfect CSI is not available.

- Regarding sphere-decoding analysis, quantization errors can affect the accuracy of soft-output values sent to an outer decoder, degrading overall performance. An analysis of such errors, as well as imperfect CSI on the sphere decoder, can contribute to interesting research into the evaluation of these modern multi-antenna coding techniques.

- An analysis can be performed on the performance of modern ST codes with LDPC codes using different equalizers and decoders. A performance and complexity comparison can be done for sphere decoding, MMSE, ZF-detectors under various different antenna setups and channel impairments.

- The results can be extended to an analysis for differential STF block codes for MIMO-WiMAX. The differential STF block codes can be concatenated with an LDPC code and compared directly to the results obtained in this dissertation. With differential codes being suitable for very fast fading channels, an analysis of the performance evaluation of LDPC codes in a MIMO time-selective channel can be performed.

- The MIMO-WiMAX simulator can be extended in the above topics to include the packet error rate, block error rate and frame error rate. These metrics can be used to further the capabilities of the simulator to translate the simulation results from the link level to the system level.

APPENDIX A
CHANNEL DELAY PROFILES

The power delay profiles used in the dissertation are presented in this chapter. The two-ray equal profile, as well as the suburban alternative profile from [87], is presented as follows:

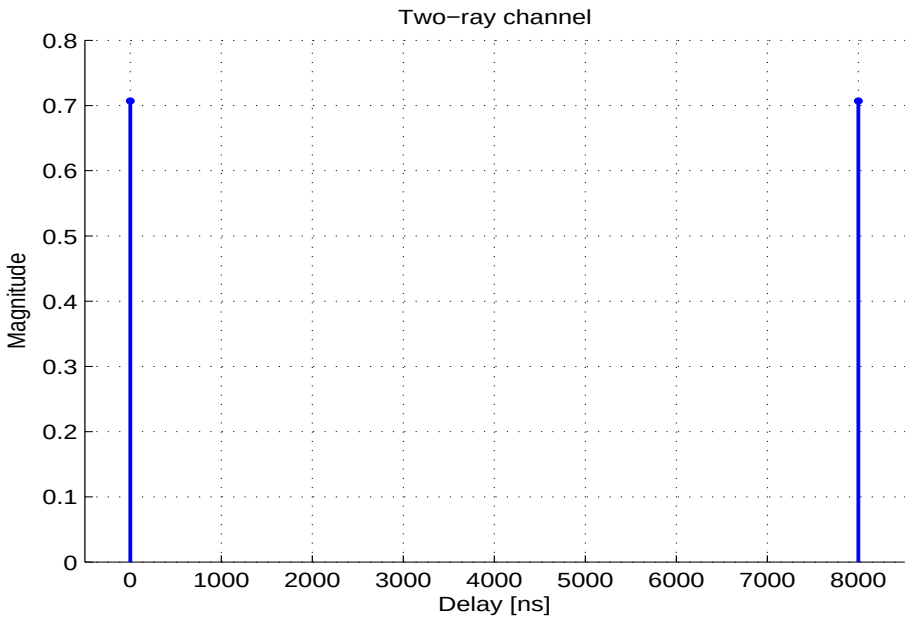

FIGURE A.1: Two-ray equal power PDP at $0\mu s$ and $8\mu s$

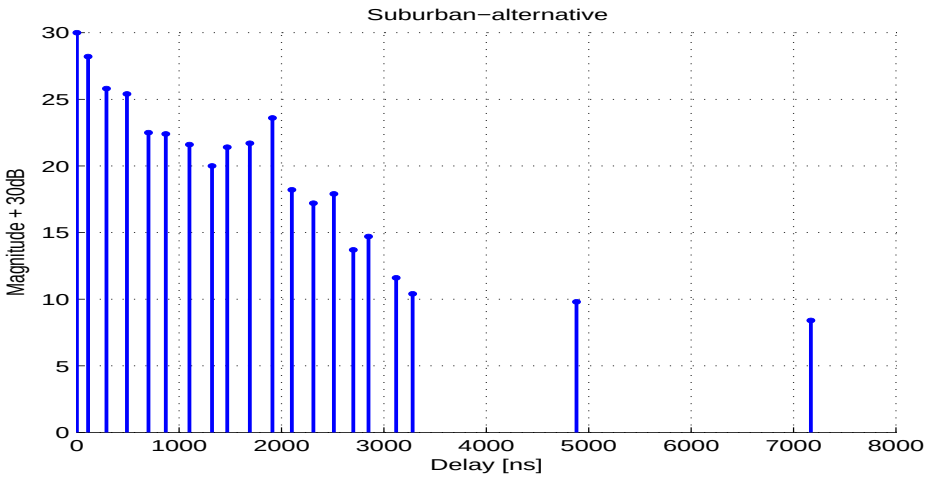

FIGURE A.2: Suburban alternative PDP

TABLE A.1: Suburban alternative PDP

Delay (ns)	Magnitude (dB)	Delay (ns)	Magnitude (dB)
0	0	1910	-6.4
110	-1.8	2100	-11.8
290	-4.2	2310	-12.8
490	-4.6	2510	-12.1
700	-7.5	2700	-16.3
870	-7.6	2850	-15.3
1100	-8.4	3120	-18.4
1320	-10	3280	-19.6
1470	-8.6	4880	-20.2
1690	-8.3	7170	-21.6

REFERENCES

[1] *Air Interface for Fixed and Mobile Broadband Wireless Systems*, IEEE Amendment and Corrigendum to IEEE Std. 802.16-2004 802.16e-2005, 2005.

[2] Wimax forum. [Online]. Available: http://www.wimaxforum.org

[3] C. Shannon, "A mathematical theory of communication," *Bell Labs Tech,*, vol. 27, pp. 623–656, Oct 1948.

[4] G.J. Foschini and M.J. Glans, "On limits of wireless communication in a fading environment when using multiple antennas," *Wireless Personal Communications*, vol. 6, no. 3, pp. 311–335, Mar 1998.

[5] E.G. Larsson and P. Stoica, *Space-Time Block Coding for Wireless Communications*. UK: Cambridge University Press, 2003.

[6] W. Zhang, "Issues on broadband wireless communication systems: Channel estimation, frequency synchronization and space-time-frequency coding," Ph.D. dissertation, Univ. of Hong Kong, China, 2005.

[7] W. Zhang, X.-G Xia, and P. C. Ching, "High-rate full-diversity space-time-frequency codes for broadband mimo block-fading channels," *IEEE Trans. Commun.*, vol. 55, pp. 25–34, Jan 2007.

[8] C. Xiao, J. Wu, S.-Y. Leong, Y. R. Zheng, and K. B. Letaief, "A discrete-time model for triply selective MIMO Rayleigh fading channels," *IEEE Trans. Commun.*, vol. 3, No 5, pp. 1678–1688, Sep 2004.

[9] B. Sklar, "Rayleigh fading channels in mobile digital communication systems Part I: Characterization," *IEEE Communications Magazine*, Jul 1997.

[10] G.D. Durgin and T.S. Rappaport, "A basic relationship between multipath angular spread and narrowband fading in a wireless channel," *IEEE Electronics Letters*, vol. 34, no. 25, pp. 2431–2432, Dec 1998.

[11] X. Ma and G.B. Giannakis, "Maximum-diversity transmission over time-selective wireless channels," in *Proc. IEEE WCNC'2002*, vol. 1, Orlando,FL, Mar 2002, pp. 497–501.

[12] X. Ma, G.B. Giannakis, and B. Lu, "Block differential encoding for rapidly fading channels," *IEEE Trans. Commun.*, vol. 52, no. 3, pp. 996–1011, Mar 2004.

[13] X. Ma and G.B. Giannakis, "Maximum-diversity transmission over doubly-selective wireless channels," *IEEE Trans. Inf. Theory*, vol. 49, no. 7, pp. 1832–1840, Jul 2003.

[14] X. Ma, G. Leus, and G.B. Giannakis, "Space-time Doppler coding for correlated time-selective fading channels," *IEEE Transactions on Signal Processing*, vol. 53, no. 6, pp. 2167–2181, Jun 2005.

[15] X. Ma and G.B. Giannakis, "Space-time coding for doubly-selective channels," in *Proc. International Conference on Circuits and Systems*, Scottsdale, AZ, Mar 2002, pp. 647–650.

[16] J.G. Proakis, *Digital Communications*. 4th ed., McGraw-Hill, New York, 2001.

[17] R. L. Peterson, R. E. Ziemer, and D. E. Borth, *Introduction to Spread Spectrum Communications*. Upper Saddle River, NJ, USA: Prentice Hall, 1995.

[18] V. Tarokh, N. Seshadri, and A. R. Calderbank, "Space-time codes for high data rate wireless communication: Performance criterion and code construction," *IEEE Trans. Inf. Theory*, vol. 44, pp. 744–765, Mar 1998.

[19] Z. Wang and G.B. Giannakis, "A simple and general parameterization quantifying performance in fading channels," *IEEE Trans. Commun.*, vol. 51, no. 8, pp. 1389–1398, Aug 2003.

[20] B.T.J. Maharaj, "MIMO Channel Modelling for Indoor Wireless Communications," Ph.D. dissertation, Univ. of Pretoria, South Africa, 2007.

[21] R. H. Clarke, "A Statistical Theory of Mobile-Radio Reception," *Bell Systems Technical Journal*, vol. 47, pp. 957–1000, 1968.

[22] A. Graham, *Kronecker Products and Matrix Calculus: With Applications*. Wiley, 1981.

[23] D. Shiu, G. Foschini, M. Gans, and J. Kahn, "Fading correlation and its effect on the capacity of multielement antenna systems," *IEEE Trans. Commun.*, vol. 48, pp. 502–513, Mar. 2000.

[24] S. L. Loyka, "Channel capacity of MIMO architecture using the exponential correlation matrix," *IEEE Commun. Lett.*, vol. 5, pp. 369–371, 2001.

[25] *Selection procedure for the choice of radio transmission technologies of UMTS*, UMTS Std. UMTS 30.03 version 3.2.0 ETSI, 1998.

[26] G. Marsagalia and T. Bray, "A convenient method for generating normal variables," *Society for Industrial Applied Mathematics Journal*, vol. 6, pp. 260–264, 1964.

[27] B. Wichmann and D. Hill, "Building a random-number generator," *Byte Magazine*, pp. 127–128, 1987.

[28] L. Staphorst, "Viterbi decoded linear block codes for narrowband and wideband wireless communication over mobile fading channels," Master's thesis, University of Pretoria, South Africa, 2005.

[29] B.P. Salmon, "Optimizing LDPC codes for a mobile WiMAX system with saturated transmission amplifier," Master's thesis, University of Pretoria, South Africa, 2008.

[30] W.C. Jakes, *Microwave Mobile Communications.* Piscataway, NJ: IEEE Press, 1994.

[31] M.F Pop and N.C Beaulieu, "Limitations of sum-of-sinoids fading channel," *IEEE Trans. Commun.*, vol. 49, pp. 699–708, Apr 2001.

[32] Y.R. Zheng and C. Xiao, "Simulation models with correct statistical properties for Rayleigh fading channels," *IEEE Trans. Commun.*, vol. 51, pp. 920–928, Jun 2003.

[33] Y.R Zheng and C. Xiao, "Improved models for the generation of multiple uncorrelated Rayleigh fading waveforms," *IEEE Commun. Lett*, vol. 6, pp. 256–258, Jun 2002.

[34] W Kleynhans, "On channel estimation for mobile WiMAX," Master's thesis, University of Pretoria, South Africa, 2008.

[35] Z. Wang and G.B. Giannakis, "Where Fourier meets Shannon," *IEEE Signal Processing Magazine*, vol. 17, no. 3, pp. 29–48, May 2000.

[36] Toeplitz and Circulant matrices: A review. [Online]. Available: http://www-ee.stanford.edu/˜gray/toeplitz.pdf

[37] Robert H. Morelos-Zaragoza, *The Art of Error Correcting Coding*. John Wiley & sons, Ltd, 2004.

[38] L. Hanzo and W. Webb and T. Keller, *Single- and Multicarrier Quadrature Amplitude Modulation: Principles and Applications for Personal Communications, WLANs and Broadcasting.* IEEE Press, 2002.

[39] W. Su, Z. Safar, and K. J. R Liu, "Full-rate full-diversity space-frequency codes with optimum coding advantage," *IEEE Trans. Inf. Theory*, vol. 51, pp. 229–249, Jan 2005.

[40] M.O. Damen, K. Abed-Meraim, and J.-C. Belfiore, "Diagonal algebraic space-time block codes," *IEEE Trans. Inf. Theory*, vol. 48, no. 3, pp. 628–636, Mar 2002.

[41] A.F. Naguib, V. Tarokh, N. Seshadri, and A.R. Calderbank, "A space-time coding modem for high-data-rate wireless communication," *IEEE J. Select. Areas Commun.*, vol. 16, pp. 1459–1478, Oct 1998.

[42] S. Alamouti, "A simple transmit diversity technique for wireless communications," *IEEE J. Select. Areas Commun.*, vol. 16, pp. 1451–1458, Oct 1998.

[43] V. Tarokh, H. Jafarkhani, and A.R. Calderbank, "Space-time block codes from orthogonal designs," *IEEE Trans. Inf. Theory*, vol. 45, pp. 1456–1467, May 1999.

[44] H. Jafarkhani, "A quasi-orthogonal space-time block code," *IEEE Trans. Commun.*, vol. 49, pp. 1–4, Jan 2001.

[45] Y. Xin, Z. Wang, and G.B. Giannakis, "Linear unitary precoders for maximum diversity gains with multiple transmit- and receive-antennas," in *Proc. of 34th Asilomar Conference on Signals, Systems, and Computers*, Pacific Grove, CA, Oct 29-Nov 1, 2000, vol. 2, pp. 1553–1557.

[46] M.O Damen, K. Abed-Meraim, and J.-C. Belfiore, "Systematic construction of full diversity algebraic constellations," *IEEE Trans. Inf. Theory*, vol. 49, pp. 3344–3349, Dec 2003.

[47] H.E. Gamal and M.O. Damen, "Universal space-time coding," *IEEE Trans. Inf. Theory*, vol. 49, pp. 1097–1119, May 2003.

[48] M.P Fitz, J. Grimm, and S. Siwamogsatham, "A new view of performance analysis techniques in correlated Rayleigh fading," in *Proc. IEEE Wireless Communication and Networking Conf.*, Sep 1999, pp. 139–134.

[49] S. Siwamogsatham, M.P Fitz, and J. Grimm, "A new view of performance analysis of transmit diversity schemes in Rayleigh fading," *IEEE Trans. Inf. Theory*, vol. 48, no. 4, pp. 950–956, Apr 2002.

[50] W. Su, Z. Safar, M. Olfat, and K. Liu, "Obtaining full-diversity space-frequency codes from space-time codes via mapping," *IEEE Trans. Signal Process.*, vol. 51, no. 11, pp. 2905–2916, Nov 2003.

[51] D. Agrawal, V. Tarokh, A. Naguib, and N. Seshadri, "Space-time coded OFDM for high data-rate wireless communications over wideband channels," in *Proc. IEEE Veh. Technol. Conf.*, May 1998, pp. 2232–2236.

[52] K.F. Lee and D.B. Williams, "A space-time coded transmitter diversity technique for frequency selective fading channels," in *Proc. IEEE Sensor Array and Multichannel Signal Processing Workshop*, Cambridge, MA, Mar 2000, pp. 149–152.

[53] W. Zhang, X.-G Xia, and P. C. Ching, "Full-diversity and fast ML decoding properties of general orthogonal space-time block codes for MIMO-OFDM systems," *IEEE Trans. Wireless Commun.*, vol. 6, no 5, May 2007.

[54] V. Tarokh, H. Jafarkhani, and A. R. Calderbank, "Space-time block coding for wireless communication: Performance results," *IEEE J. Select. Areas Commun.*, vol. 17, pp. 451–460, Mar 1999.

[55] G. Bauch, "Concatenation of space-time block codes and turbo-tcm," in *Proceedings of IEEE International Conference on Communications*, Vancouver, Canada, Jun 1999, pp. 1202–1206.

[56] K.F. Lee and D.B. Williams, "A space-frequency coded transmitter diversity technique for OFDM systems," in *Proc. IEEE Global Commun. Conf.*, vol. 3, Nov 27-Dec 1, 2000, pp. 1473–1477.

[57] L. Shao, S. Roy, and S. Sandhu, "Rate-one space-frequency block codes with maximum diversity gain for MIMO-OFDM," in *Proc. IEEE Global Telecommun. Conf.*, Dec 1-5, 2003, pp. 809–813.

[58] W. Su, Z. Safar, and K.J.R. Liu, "Systematic design of space-frequency codes with full rate and full diversity," in *Proc. IEEE Wireless Communication and Networking Conf.*, Mar 21-25, 2004, vol.3, pp. 1436–1441.

[59] H.E. Gamal and A.R. Hammons Jr., "On the design of algebraic space-time codes for MIMO block fading channels," *IEEE Trans. Inf. Theory*, vol. 49, pp. 151–163, Jan 2003.

[60] M. Fozunbal, S.W. McLaughlin, and R.W Schafer, "On space-time-frequency coding over MIMO-OFDM systems," *IEEE Trans. Wireless Commun.*, vol. 4, pp. 320–331, Jan 2005.

[61] W. Su, Z. Safar, and K.J.R Liu, "Towards maximum achievable diversity in space, time, and frequency: performance analysis and code design," *IEEE Trans. Wireless Commun.*, vol. 4, pp. 1847–1857, Jul 2005.

[62] J. Boutros, E. Viterbo, C. Rastello, and J.-C Belfiore, "Good lattice constellations for both Rayleigh and Gaussian channel," *IEEE Trans. Inf. Theory*, vol. 42, no 2, pp. 502–518, Mar. 1996.

[63] X. Giraud, E. Boutillian, and J.-C Belfiore, "Algebraic tools to build modulation schemes for fading channels," *IEEE Trans. Inf. Theory*, vol. 43, no 3, pp. 938–952, May 1997.

[64] Z. Wang and G.B. Giannakis, "Complex-field coding for OFDM over fading wireless channels," *IEEE Trans. Inf. Theory*, vol. 49, no 3, pp. 707–720, Mar 2003.

[65] Y. Xin, Z. Liu, and G.B Giannakis, "High-rate layered space-time coding based on constellation rotation," in *Proc. of Wireless Communications and Networking Conference*, Orlando, FL, Mar 17-21, 2002, pp. 471–476.

[66] Y. Xin and G.B. Giannakis, "High-rate space-time layered OFDM," *IEEE Commun. Lett.*, vol. 6, no. 5, pp. 187–189, May 2002.

[67] Y. Xin, Z. Wang, and G.B Giannakis, "Space-time diversity systems based on linear constellation precoding," *IEEE Trans. Wireless Commun.*, vol. 2, no. 2, pp. 294–309, Mar 2003.

[68] M.O Damen, A. Tewfik, and J. C. Belfiore, "A construction of a space-time code based on number theory," *IEEE Trans. Inf. Theory*, vol. 48, pp. 753–760, Mar 2002.

[69] R.G Gallagher, *Low-density Parity-Check Codes*, MIT Press, Cambridge, MA, 1963.

[70] D.J.C. MacKay and R.M. Neal, "Near Shannon limit performance of low density parity check codes," *IEEE Commun. Lett*, vol. 32, no. 18, pp. 1645–1646, Aug 1996.

[71] R. Tanner, "A recursive approach to low complexity codes," *IEEE Trans. Inf. Theory*, vol. 27, no 5, pp. 533–547, Sep. 1981.

[72] T. Richardson and R. Urbanke, *Modern coding theory*. New York: Cambridge University Press, 2008.

[73] J. Pearl, *Probalistic Reasoning in Intelligent Systems*. San Francisco, CA: Kauffmann, 1988.

[74] R. Urbanke and T. Richardson, "Design of Capacity-Approaching Irregular Low-density Parity-Check Codes," *IEEE Trans. Inf. Theory*, vol. 47, no 2, pp. 619–637, Feb 2001.

[75] J. Hou, P. Siegel, and L. Milstein, "Performance analysis and code optimization of low-density parity-check codes on Rayleigh fading channels," *IEEE Journal on Selected Areas of Communication*, vol. 19, no 5, pp. 924–934, May 2001.

[76] T. Richardson and R. Urbanke, "The capacity of Low-Density Parity Check codes under message passing decoding," *IEEE Trans. Inf. Theory*, vol. 47, no 2, pp. 599–618, Feb 2001.

[77] X. Hu, D. Arnold, and E. Eleftheriou, "Progressive edge-growth Tanner Graphs," in *Proceedings of IEEE GLOBECOM'2001*, vol 2, San Antonio, Texas, USA, Nov 2001, pp. 995–1001.

[78] B. Hassibi and H. Vikalo, "On the expected complexity of sphere decoding," in *Proc. of 35th Asilomar Conference on Signals, Systems, and Computers*, Pacific Grove, CA, Nov 4-7, 2001, vol.2, pp. 1051–1055.

[79] W. Su, Z. Safar, and K.J.R. Liu, "A Fast Sphere Decoding Algorithm for Space-Frequency Block Codes," *EURASIP Journal on Applied Signal Processing*, pp. 1–14, 2006.

[80] W. Su, Z. Safar, and K.J.R Liu, "A Fast Sphere Decoding Framework for Space-Frequency Block Codes," in *Proc. IEEE International Conference on Communications*, Jun 20-24, 2004, vol.5, pp. 2591–2595.

[81] T. Cui and C. Tellambura, "An Efficient Generalized Sphere Decoder for Rank-Deficient MIMO Systems," *IEEE Communications Letters*, vol. 9, no. 5, pp. 423–425, May 2005.

[82] Gene H. Golub and Charles F. Van Loan, *Matrix computations*. Johns Hopkins University Press.

[83] P. Robbertson, E. Villebrun, and P. Hoeher, "A comparison of optimal and suboptimal MAP decoding algorithms operating in the log domain," in *Proc. Int. Conf. Communications*, Jun 1995, pp. 1009–1013.

[84] B.M. Hochwald and S. ten Brink, "Achieving near-capacity on a multiple-antenna channel," *IEEE Trans. Commun.*, vol. 51, no 3, pp. 389–399, Mar 2003.

[85] R. Wang and G.B. Giannakis, "Approaching MIMO channel capacity with reduced-complexity sphere decoding," *IEEE Trans. Commun.*, vol. 54, no 4, pp. 587–590, Apr 2006.

[86] A.F. Molisch, M. Toeltsch, E. Bonek, and R.S. Thoma, "Capacity of MIMO systems based on measured wireless channels," *IEEE J. Select. Areas Commun.*, vol. 20, pp. 561–569, Apr 2002.

[87] K. Jeong et al., "Multipath channel models for wireless local and metropolitan area networks," *in Information Technology and Applications (ICITA)*, pp. 295–298, Jul 2005.